

TEMPERATURE DEPENDENT DIELECTRIC AND MAGNETIC PROPERTIES OF Gd AND Ti CO-DOPED BiFeO₃ MULTIFERROICS

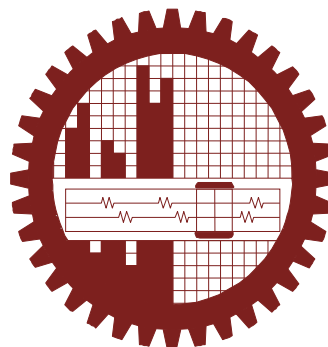
*A Dissertation Submitted to the Department of Physics, Bangladesh University of
Engineering & Technology, Dhaka in Partial Fulfillment of Requirement for the
Degree of Master of Philosophy in Physics*

SUBMITTED

By

Md. Zahirul Islam

EXAMINATION ROLL NO. : 0412143005P
SESSION : April 2012



DEPARTMENT OF PHYSICS

BANGLADESH UNIVERSITY OF ENGINEERING & TECHNOLOGY

DHAKA 1000, BANGLADESH

CANDIDATE’S DECLARATION

It is hereby declared that this thesis or any part of it has not been submitted elsewhere
for the award of any degree or diploma.



.....

Md. Zahirul Islam


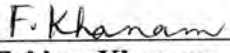
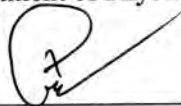
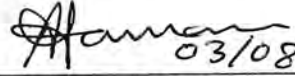
**BANGLADESH UNIVERSITY OF ENGINEERING & TECHNOLOGY (BUET), DHAKA
DEPARTMENT OF PHYSICS**



CERTIFICATION OF THESIS

The thesis titled “**TEMPERATURE DEPENDENT DIELECTRIC AND MAGNETIC PROPERTIES OF Gd AND Ti CO-DOPED BiFeO₃ MULTIFERROICS**” submitted by **Md. Zahirul Islam**, Roll No-0412143005 P, Registration No-0412143005 P, Session: April-2012, has been accepted as satisfactory in partial fulfillment of the requirement for the degree of **Master of Philosophy (M. Phil.)** in Physics on 03 August, 2016.

BOARD OF EXAMINERS

1. 
Dr. Mohammed Abdul Basith
Associate Professor,
Department of Physics, BUET, Dhaka. Chairman
(Supervisor)
2. 
Fahima Khanam
Professor & Head
Department of Physics, BUET, Dhaka. Member
(Ex-Officio)
3. 
Dr. Md. Feroz Alam Khan
Professor
Department of Physics, BUET, Dhaka. Member
4. 
Dr. Abdul Hannan
Professor
Department of Physics
Shahjalal University of Science and Technology, Sylhet. Member (External)

*Dedicated
To
My parents*

ACKNOWLEDGEMENTS

I firstly express all of my admiration and devotion to the almighty Allah, the most beneficial who has enabled me to perform this research work and to submit this thesis. I express my profound gratitude to my honorable supervisor Dr. Mohammed Abdul Basith, Associate Professor, Department of Physics, BUET, for his constant direction, constructive criticism and inspiration in pursuing the whole investigation of the present research. Words are always insufficient to express his working capacities and unending enthusiasm for scientific rigorousness for innovative investigations. This always becomes the everlasting source of inspiration for his students. I am deeply grateful to Professor Fahima Khanam, Head, Department of Physics, BUET, for her kind permission to do this work. I am also grateful to BUET authority for providing the financial grant for this research. I like to express my gratitude to Professor Dr. Md. Abu Hashan Bhuiyan, Professor Dr. Md. Feroz Alam Khan and all other teachers of Physics Department for their cooperation.

I wish to thank specially Dr. Bashir Ahmed Arima, Assistant Professor, Department of Electrical & Electronics Engineering, Yamagata University, Japan for providing X-ray Photoelectron Spectroscopy (XPS) and Superconducting Quantum Inteference Devices (SQUID) magnetometer facilities.

This work was partially supported by Ministry of Science and Technology, Government of Bangladesh, Grant No.:39.009.002.01.00.053.2014-2015/PHY'S-273/(26.01.2015) and The world Academy of Sciences (TWAS), Ref.:14-066 RG/PHYS/AS_I; UNESCO FR: 324028567.

I also gratefully acknowledge the wishes of my younger researchers Areef, Jalil, Saiful, Popy, Rafiq and Hena for their constant support.

Ultimately, I would mention a very special gratefulness for the moral support and sustaining inspiration provided by the members of my family. This dissertation would never have been possible without their love and affection.

ABSTRACT

Undoped BiFeO_3 , Gd doped $\text{Bi}_{0.9}\text{Gd}_{0.1}\text{FeO}_3$, and Gd-Ti co-doped $\text{Bi}_{0.9}\text{Gd}_{0.1}\text{Fe}_{1-x}\text{Ti}_x\text{O}_3$ ($x = 0.10, 0.20$) materials were synthesized to report their temperature dependent electric and magnetic properties. The structural analysis and phase identification of these multiferroic ceramics were performed using Rietveld refinement. The Rietveld analysis has confirmed the high phase purity of the 10% Gd-Ti co-doped $\text{Bi}_{0.9}\text{Gd}_{0.1}\text{Fe}_{0.9}\text{Ti}_{0.1}\text{O}_3$ sample compared to that of other compositions under investigation. The major phase of this particular composition is of rhombohedral R3c type structure (wt% > 97%) with negligible amount of impurity phases. In terms of characterization, the magnetic properties of this co-doped ceramic system were addressed by applying substantially higher magnetic fields than that applied in previously reported investigations of this material system. Both the coercive fields and remanent magnetizations were higher for 10% Gd-Ti co-doped $\text{Bi}_{0.9}\text{Gd}_{0.1}\text{Fe}_{0.9}\text{Ti}_{0.1}\text{O}_3$ sample than those for other materials. The dependence of temperature on their magnetization behaviour have been investigated elaborately. Unexpectedly, the coercive fields of this multiferroic system increased with increasing temperature. The coercive fields and remanent magnetization were higher over a wide range of temperatures in 10% Gd-Ti co-doped $\text{Bi}_{0.9}\text{Gd}_{0.1}\text{Fe}_{0.9}\text{Ti}_{0.1}\text{O}_3$ sample compared to those of other compositions. The magnetization versus applied magnetic field (M-H) hysteresis loops at different temperatures exhibited an asymmetric shift towards the magnetic field axes which indicated the presence of exchange bias effect in this material system. The hysteresis loops were also carried out at temperatures 150 K and 250 K by cooling down the sample from 300 K in various cooling magnetic fields. The exchange bias fields increased with cooling magnetic fields and decreased with temperature. The biasing fields were tunable by field cooling at temperatures up to 250 K. Additionally, the leakage current density has been measured to explore its effect on the ferroelectric properties of this multiferroic system. The outcome of this investigation suggested that the substitution of 10% Gd and Ti in place of Bi and Fe, respectively, in BiFeO_3 significantly enhances its multiferroic properties. The improved properties of this specific composition was associated with homogeneous reduced grain size, significant suppression of impurity phases and reduction in leakage current density which was further asserted by polarization versus electric field (P-E) hysteresis loop measurements.

Contents

Title.....	i
Declaration.....	ii
Dedication.....	iii
Acknowledgements.....	i v
Abstract.....	v
Contents.....	vi
List of Figures.....	i x
List of Tables.....	xiii

Chapter 1

Introduction [1-6]

1.1 Introduction.....	1
1.2 Aim and Objectives.....	2
1.3 Outline of the Thesis.....	3
References:.....	4

Chapter 2

Theoretical Background [7-37]

2.1 Electrical Properties Of Materials.....	8
2.1.1 Dielectrics.....	8
2.1.2 Ferroelectricity.....	10
2.2 Magnetic Properties Of Materials.....	13
2.2.1 Magnetic Ordering.....	13
2.2.2 Magnetic Interactions.....	15
2.3 Multiferroics.....	16
2.3.1 Ferromagnetic Materials.....	17
2.3.2 Ferroelectric Materials.....	20
2.3.3 Ferroelastic materials.....	21

2.4 Applications Of Multiferroics	24
24.1 Magnetic Field Sensors	24
2.4.2 Electric Field Control Of Exchange Bias	24
2.4.3 Multiferroic-Semiconductor Hetrostructures As Spin Filters	25
2.4.4 Multistate Memory Devices	25
2.5 Single Phase Multiferroic Compounds	26
2.5.1 Bismuth Ferrite (Bifeo3).....	26
2.5.2 Crystal Structure Of Bifeo3	27
2.5.3 Ferroelectricity In Bifeo3	28
2.5.4 Ferromagnetism In Bifeo3	29
2.5.5 Magnetoelectric Coupling In Bifeo3	31
2.5.6 Challenges With Bifeo3	32
References:	34

Chapter 3

Experimental Details [39-58]

3.1 Sample Preparation	39
3.1.1 Introduction	39
3.1.2 Standard Solid-State Reaction Technique	40
3.1.3 Calcination	42
3.1.4 Shaping	43
3.1.5 Sintering	44
3.1.6 Synthesis of composition	45
3.2 Characterization Techniques	46
3.2.1 Field Emission Scanning Electron Microscopy	46
3.2.2 X-Ray Diffraction Study:	48
3.2.3 X-Ray Photoelectron Spectroscopy (Xps)	50
3.2.4 The Squid Magnetometer	52
3.2.5 Ferroelectric Measurements	54
3.2.5.1 Basic Theory Of Operation	55
3.2.6 Dielectric Properties Measurement	56

References:.....	58
------------------	----

Chapter 4

Results and Discussion [59-96]

4.1 Morphological Studies	59
4.2 Structural Characterization	61
4.3 Magnetic Characterization	65
4.4 Electric Measurements.....	86
4.5 Dielectric Measurements.....	89
References :.....	91

Chapter 5

Summary and Conclusions [97-99]

5.1 Summary.....	97
5.2 Conclusions.....	98
5.3 Future work.....	98
References:.....	99

LIST OF FIGURES

Figure 2.1	Systematic representation of possible four types of polarization process.	08
Figure 2.2	systematic representation of various mechanisms in dielectric constant versus frequency plot.	10
Figure 2.3	Systematic representation of ferroelectric (P-E) hysteresis loop [8].	11
Figure 2.4	Structure of BaTiO ₃ above (a) and (b) Curie temperature(T _c).	12
Figure 2.5	Schematic representation of spins aligned in ferromagnetic (a), antiferromagnetic (b), ferrimagnetic (c) and canted antiferromagnetic (d) manner.	12
Figure 2.6	Systematic representative of spin arrangements in (a) A-type, (b) C-type and (c) G-type AF ordering.	13
Figure 2.7	Systematic representation of ferromagnetic(M-H) hystersis loop.	14
Figure 2.8	(a) Separation of two magnetic moments by oxygen atom, (b-c) different possibility of antiferromagnetic alignment of magnetic moment due to superexchange effect [9].	15
Figure 2.9	Relationship between magnetoelectric and multiferroic materials (a) and illustration of different types of possible coupling in multiferroic materials (b) [12].	16
Figure 2.10	Typical hysteresis loop of a ferromagnetic material displaying magnetization switching.	19
Figure 2.11	Hysteresis loops of (a) ferromagnetic,(b)ferroelectric and (c) ferroelastic materials.	20
Figure 2.12	The perovskite crystal structure of BiFeO ₃ .	26
Figure 2.13	Crystal structure of bulk BiFeO ₃ with opposite rotation of successive oxygen octahedral around [111] polar axes. Red arrow indicates orientation of Fe magnetic moments in (111) plane[23].	27
Figure 2.14	Hexagonal structure of BiFeO ₃ lattice with Fe ³⁺ and O ²⁻ ions. The arrows indicate direction of Fe spins .	30
Figure 2.15	Schematic representations of spiral spin structure of wavelength $\lambda = 62$ nm.	30

Figure 2.16	Representation of weak ferromagnetism in BFO due to D-M interaction .	31
Figure 3.1	Flow chart of solid state reaction technique).	41
Figure 3.2	(a)Basic scheme of a typical SEM .(b) Jeol JSM 6490LA scanning electron microscope	47
Figure 3.3	X-ray Diffractometer (XRD) .	48
Figure 3.4	XPS Spectroscopy.	51
Figure 3.5	Cutway view of the MPMS SQUID magnetometer.ate	52
Figure 3.6	Automatic P-E Loop tracer	55
Figure 3.7	Sawyer Tower (S-T) circuit	54
Figure 3.8	WAYNE KERR impedance analyzer 6500B series	56
Figure 4.1	FESEM micrograph of $\text{Bi}_{0.9}\text{Gd}_{0.1}\text{Fe}_{1-x}\text{Ti}_x\text{O}_3$ ceramics: (a)undoped BiFeO_3 (b) $x = 0.00$, (c) $x = 0.10$. Inset: respective histograms of images (a),(b) and (c).	61
Figure 4.2	Rietveld refined XRD patterns of (a) undoped BiFeO_3 , (b) Gd doped $\text{Bi}_{0.9}\text{Gd}_{0.1}\text{Fe}_{1-x}\text{Ti}_x\text{O}_3$ ($x = 0.00$), (c) Gd-Ti co-doped $\text{Bi}_{0.9}\text{Gd}_{0.1}\text{Fe}_{1-x}\text{Ti}_x\text{O}_3$ ($x = 0.10$) and (d) Gd-Ti co-doped $\text{Bi}_{0.9}\text{Gd}_{0.1}\text{Fe}_{1-x}\text{Ti}_x\text{O}_3$ ($x = 0.20$) ceramics carried out at RT.	63
Figure 4.3	The O 1s core XPS spectrum of (a) undoped BiFeO_3 ,(b) Gd doped $\text{Bi}_{0.9}\text{Gd}_{0.1}\text{Fe}_{1-x}\text{Ti}_x\text{O}_3$ ($x = 0.00$), (c) Gd-Ti co-doped $\text{Bi}_{0.9}\text{Gd}_{0.1}\text{Fe}_{1-x}\text{Ti}_x\text{O}_3$ ($x = 0.10$) and (d) Gd-Ti co-doped $\text{Bi}_{0.9}\text{Gd}_{0.1}\text{Fe}_{1-x}\text{Ti}_x\text{O}_3$ ($x = 0.20$) samples.	65
Figure 4.4	The M – H hysteresis loops of undoped, Gd doped and Gd-Ti co-doped BFO ceramics were carried out at RT with an applied magnetic field of up to ± 50 kOe.	67
Figure 4.5	The M – H hysteresis loops of 10% Gd and Ti co-doped $\text{Bi}_{0.9}\text{Gd}_{0.1}\text{Fe}_{0.9}\text{Ti}_{0.1}\text{O}_3$ ceramics for different H_{max} at RT.	68
Figure 4.6	The variation of H_c and H_{EB} of 10% Gd and Ti co-doped $\text{Bi}_{0.9}\text{Gd}_{0.1}\text{Fe}_{0.9}\text{Ti}_{0.1}\text{O}_3$ material as a function of maximum applied magnetic fields. The inset shows the variation of M_r also as a function of H_{max} .	70

- Figure 4.7 (a) The $M - H$ hysteresis loops of sample $x = 0.00$ (composition $\text{Bi}_{0.9}\text{Gd}_{0.1}\text{FeO}_3$) carried out at different temperatures. (b-h) An enlarged view of the low field $M - H$ hysteresis loops of sample $x = 0.00$ obtained at temperatures : (b) 20 K (c) 50 K (d) 100 K (e) 150 K (f) 200 K (g) 250 K and (h) 300 K. 71
- Figure 4.8 (a) The $M - H$ hysteresis loops of sample $x = 0.10$ (composition $\text{Bi}_{0.9}\text{Gd}_{0.1}\text{Fe}_{0.9}\text{Ti}_{0.1}\text{O}_3$) carried out at different temperatures. (b-h) An enlarged view of the low field $M - H$ hysteresis loops of sample $x = 0.10$ obtained at temperatures : (b) 20 K (c) 50 K (d) 100 K (e) 150 K (f) 200 K (g) 250 K and (h) 300 K. 72
- Figure 4.9 a) The M-H hysteresis loops of sample $x = 0.20$ (composition $\text{Bi}_{0.9}\text{Gd}_{0.1}\text{Fe}_{0.8}\text{Ti}_{0.2}\text{O}_3$) carried out at different temperatures. (b-h) An enlarged view of the low field M-H hysteresis loops of sample $x = 0.20$ obtained at temperatures : (b) 20 K (c) 50 K (d) 100 K (e) 150 K (f) 200 K (g) 250 K and (h) 300 K. 73
- Figure 4.10 The variation of (a) coercivity (H_c) and (b) remanent magnetization (M_r) as a function of temperature in $\text{Bi}_{0.9}\text{Gd}_{0.1}\text{Fe}_{1-x}\text{Ti}_x\text{O}_3$ ($x = 0.00-0.20$) compounds. Both H_c and M_r are higher over a wide range of temperatures in sample $x = 0.10$. 75
- Figure 4.11 The variation of M_s (the maximum magnetization at 50 kOe) and H_c as a function of temperature in sample $x = 0.10$ ($\text{Bi}_{0.9}\text{Gd}_{0.1}\text{Fe}_{0.9}\text{Ti}_{0.1}\text{O}_3$). 76
- Figure 4.12 The temperature dependence of magnetization (M-T curves) of $\text{Bi}_{0.9}\text{Gd}_{0.1}\text{FeO}_3$ sample measured in ZFC and FC processes in the presence of 500 Oe applied magnetic fields. Both ZFC and FC curves coincide with each other without showing any bifurcation. 78
- Figure 4.13 The temperature dependence of magnetization (M-T curves) of $\text{Bi}_{0.9}\text{Gd}_{0.1}\text{Fe}_{0.9}\text{Ti}_{0.1}\text{O}_3$ sample measured in ZFC and FC processes in the presence of 500 Oe applied magnetic fields. 78

- Both ZFC and FC curves coincide with each other without showing any bifurcation.
- Figure 4.14 The temperature dependence of magnetization (M - T curves) of $\text{Bi}_{0.9}\text{Gd}_{0.1}\text{Fe}_{0.8}\text{Ti}_{0.2}\text{O}_3$ sample measured in ZFC and FC processes in the presence of 500 Oe applied magnetic fields. Both ZFC and FC curves coincide with each other without showing any bifurcation. 79
- Figure 4.15 The variation of exchange bias fields (H_{EB}) as a function of temperature in $\text{Bi}_{0.9}\text{Gd}_{0.1}\text{Fe}_{0.9}\text{Ti}_{0.1}\text{O}_3$. The H_{EB} values were calculated from the asymmetric shift of the M - H hysteresis loops of figures 2(b-h). 81
- Figure 4.16 (a) The $M - H$ hysteresis loops of sample $x = 0.10$ measured at 150 K by applying cooling magnetic fields. (b-h) The enlarged views show the effect of cooling magnetic field on asymmetric shifting of the hysteresis loops. 83
- Figure 4.17 (a) The $M - H$ hysteresis loops of sample $x = 0.10$ measured at 250 K in presence of cooling magnetic fields. (b-h) The enlarged views demonstrate the effect of cooling magnetic field on asymmetric shifting of the field axes. 84
- Figure 4.18 Cooling field dependence of exchange bias field (H_{EB}) at 150 K and 250 K for $\text{Bi}_{0.9}\text{Gd}_{0.1}\text{Fe}_{0.9}\text{Ti}_{0.1}\text{O}_3$ ceramic. The graph also demonstrates the dependency of H_{EB} on temperature. 85
- Figure 4.19 Current density of undoped, Gd doped and Gd-Ti co doped $\text{Bi}_{0.9}\text{Gd}_{0.1}\text{Fe}_{1-x}\text{Ti}_x\text{O}_3$ ($x = 0.00, 0.10$ and 0.20) materials as a function of applied electric fields. The upper x-axis correspond to bulk BiFeO_3 . 87
- Figure 4.20 The P-E hysteresis loops of (a) undoped BFO, (b) $\text{Bi}_{0.9}\text{Gd}_{0.1}\text{FeO}_3$ ($x = 0.00$) (c) $\text{Bi}_{0.9}\text{Gd}_{0.1}\text{Fe}_{0.9}\text{Ti}_{0.1}\text{O}_3$ ($x = 0.10$) and (d) $\text{Bi}_{0.9}\text{Gd}_{0.1}\text{Fe}_{0.8}\text{Ti}_{0.2}\text{O}_3$ ($x = 0.20$) materials. 88
- Figure 4.21 The variation of (a) dielectric constant and (b) dielectric loss as a function of temperatures in $\text{Bi}_{0.9}\text{Gd}_{0.1}\text{Fe}_{0.9}\text{Ti}_{0.1}\text{O}_3$. The dielectric anomaly is clearly visible around antiferromagnetic Néel temperature. 90

LIST OF TABLES

Table 3.1	Variable in sintering	45
Table 4.1	Rietveld refined structural parameters and amount of phases present (in wt%) obtained from XRD studies of BFO, Gd doped BFO and Gd-Ti co-doped $\text{Bi}_{0.9}\text{Gd}_{0.1}\text{Fe}_{1-x}\text{Ti}_x\text{O}_3$ ($x = 0.10-0.20$).	64
Table 4.2	The table shows the calculated values of M_r , H_c and H_{EB} for undoped BiFeO_3 , Gd doped $\text{Bi}_{0.9}\text{Gd}_{0.1}\text{Fe}_{1-x}\text{Ti}_x\text{O}_3$ ($x = 0.00$) and Gd-Ti co-doped $\text{Bi}_{0.9}\text{Gd}_{0.1}\text{Fe}_{1-x}\text{Ti}_x\text{O}_3$ ($x = 0.10-0.20$) ceramics observed at RT.	68
Table 4.3	The table shows the exchange bias fields of $\text{Bi}_{0.9}\text{Gd}_{0.1}\text{Fe}_{1-x}\text{Ti}_x\text{O}_3$ ($x = 0.00-0.20$) compositions at different temperatures.	81
Table 4.4	The table shows the effect of cooling magnetic fields on H_c of $\text{Bi}_{0.9}\text{Gd}_{0.1}\text{Fe}_{0.9}\text{Ti}_{0.1}\text{O}_3$ sample at temperatures 150 K and 250 K.	85

Chapter 1

Introduction

1.1 Introduction

Multiferroic materials, in which ferromagnetic, ferroelectric, and/or ferroelastic orderings coexist, have attracted significant research interest since many years [1-5] due to their potential applications in data storage media, spintronics and ferroelectric random-access memories. The co-existence of 'ferro' orders in multiferroics allows the possibility that the magnetization can be tuned by an applied electric field and vice versa. Among the limited choices offered by the multiferroic materials, BiFeO₃ (BFO), one of the single-phase multiferroic materials at room temperature, exhibits the co-existence of ferroelectric ordering with Curie temperature (T_C) of 1123 K and antiferromagnetic (AFM) ordering with a Neel temperature (T_N) of 643 K [6]. In BiFeO₃, magnetic ordering is of antiferromagnetic type, having a spiral modulated spin structure (SMSS) with an incommensurate long-wavelength period of 62 nm [6]. This spiral spin structure cancels the macroscopic magnetization and inhibits the observation of the linear magnetoelectric effect [7]. These problems ultimately limit the use of bulk BiFeO₃ in functional applications. Recent investigations demonstrated that in order to perturb the SMSS and improve the magnetic properties of BiFeO₃, partial substitution of Bi by rare-earth ions [8, 9] or alkaline-earth ions [10] and also substitution of Fe by transition metal ions [11, 12] is an effective route. It is also reported that simultaneous minor substitution of Bi and Fe in BiFeO₃ by ions such as La and Mn, La and Ti, Nd and Sc etc, respectively [13-15] also enhance the magnetism and ferroelectricity in BiFeO₃.

Recently, Basith *et. al.* [16] observed that simultaneous substitution of Gd and Ti in place of Bi and Fe, respectively in BiFeO₃ multiferroics improved their morphological, dielectric and magnetic properties at room temperature. Later on, another group also observed fascinating magnetic, optical and dielectric properties in this Gd and Ti co-doped BiFeO₃ ceramic system at room temperature [17]. Therefore, the aim of this investigation is to conduct experiments on temperature dependence of magnetic properties of Gd and Ti co-doped Bi_{0.9}Gd_{0.1}Fe_{1-x}Ti_xO₃ (x= 0.00-0.20) multiferroic materials. In particular, our interest is to investigate the effect of

temperature on remanent magnetization, coercive fields and exchange bias (EB) fields of these bulk polycrystalline materials. Notably, the EB phenomenon which manifest itself by a shift of a magnetic hysteresis loop in systems containing ferromagnetic/antiferromagnetic bilayers has been studied extensively since many years due to its importance in spintronic applications [18]. The EB effect usually occurs when the system is cooled down in an external magnetic field through the magnetic ordering temperatures. Most of the research in this field is focused on specially prepared systems, however, recent investigations reported the presence of EB effect in perovskite manganites [19], cobaltites [20], Heusler alloys [21] and multiferroics [22]. Although EB has been observed in various bulk materials, the effect in most cases has been limited to far below room temperature (<100 K) [23, 24], thus making the systems less attractive for applications.

In previous investigation conducted by Basith *et. al.*[16], the magnetization vs. magnetic field (M – H) hysteresis loops indicated the presence of exchange bias effect in the Gd and Ti co-doped $\text{Bi}_{0.9}\text{Gd}_{0.1}\text{Fe}_{1-x}\text{Ti}_x\text{O}_3$ ($x = 0.00-0.20$) ceramics at room temperature although the biasing field was very small. Therefore, in the present investigation, the exchange bias effect was explored in this material system at different temperatures ranging from 20 K to 300 K. The influence of cooling magnetic fields at temperatures 150 K and 250 K was also carried out to observe a tunable exchange bias in 10% Gd and Ti co-doped $\text{Bi}_{0.9}\text{Gd}_{0.1}\text{Fe}_{0.9}\text{Ti}_{0.1}\text{O}_3$ composition. Along with magnetic characterization, the leakage current behavior and their effect on the ferroelectric properties were also part of this investigation. Finally, the temperature dependent dielectric properties of a selected sample were measured to confirm the presence of magnetoelectric coupling in this multiferroic material system. The compendium of these investigations is that the nominal composition of 10% Gd and Ti co-doped $\text{Bi}_{0.9}\text{Gd}_{0.1}\text{Fe}_{0.9}\text{Ti}_{0.1}\text{O}_3$ with significantly improved phase purity exhibited enhanced multiferroic properties.

1.2 Aim and Objective

The main objectives of this research are as follows:

- (a) Preparation of undoped BiFeO_3 , Gd doped $\text{Bi}_{0.9}\text{Gd}_{0.1}\text{FeO}_3$ and Gd-Ti co-doped $\text{Bi}_{0.9}\text{Gd}_{0.1}\text{Fe}_{1-x}\text{Ti}_x\text{O}_3$ ($x = 0.10, 0.20$) multiferroics by using solid state reaction method.

- (b) Structural analysis and phase identification of the synthesized samples by X-ray diffraction.
- (c) Investigation of the magnetic properties from temperature dependent magnetization experiments.
- (d) Measurements of the magnetic properties such as remanent magnetization (M_r), coercivity (H_c) and exchange bias field (H_{EB}) at particular temperatures from zero field cooled (ZFC) and field cooled (FC) magnetic hysteresis loops.
- (e) Investigation of the ferroelectric properties using a ferroelectric loop tracer (polarization vs electric field).
- (f) Investigation of the temperature dependent dielectric properties of a selected sample at different frequencies.

1.3 Outline of the Thesis

This research work has been configured into five chapters.

- ❖ **Chapter 1** presents a general introduction, aim and objectives of the present investigation.
- ❖ **Chapter 2** gives a brief overview of the materials as well as theoretical background.
- ❖ **Chapter 3** deals with the details of the sample preparation and characterization experimental techniques used in this thesis.
- ❖ **Chapter 4** represents result on temperature dependent magnetic and electrical properties of Gd and Ti co doped BiFeO_3 multiferroics.
- ❖ The conclusions drawn from the overall experimental results and discussion are presented in **chapter 5**.

References:

- [1] Spaldin, N. A., Fiebig, M., “The Renaissance of Magnetoelectric Multiferroics”, *Science*, 309, 391, 2005.
- [2] Eerenstein, W., Mathur, N. D., Scott, J. F., “Multiferroic and magnetoelectric materials”, *Nature* 442, 759-765, 2006.
- [3] Cheong, S.W., Mostovoy, M., “Multiferroics: a magnetic twist for ferroelectricity”, *Nat. Mater.*, 6, 1320, 2007.
- [4] Ramesh, R., “Emerging routes to multiferroics”, *Nature*, 461, 1218, 2009.
- [5] Wu, S. M., Cybart, S. A., Yi, D., Parker, J. M., Ramesh, R., and Dynes, R. C., “Full Electric Control of Exchange Bias”, *Phys. Rev. Lett.*, 110, 067202, 2013.
- [6] Fischer, P., Polomska, M., Sosnowska, I., and Szymanski, M., “Temperature dependence of the crystal and magnetic structures of BiFeO_3 ”, *J. Phys. C: Solid State Phys.*, 13, 1931, 1980.
- [7] Ederer, C., Spaldin N.A., “Weak ferromagnetism and magnetoelectric coupling in bismuth ferrite”, *Phys. Rev. B.*, 71, 060401, 2005.
- [8] Yuan, G. L., Wing S., Liu, J. M., and Liu, Z. G., “Structural transformation and ferroelectro magnetic behavior in single-phase $\text{Bi}_{1-x}\text{Nd}_x\text{FeO}_3$ multiferroic ceramics”, *Appl. Phys. Lett.* 89, 052905, 2006.
- [9] Khomchenko, V. A., Paixao, J. A., Costa, B. F. O., Karpinsky, D.V., Kholkin, A. L., Troyanchuk, I.O., Shvartsman, V.V., Borisov, P., Kleeman, W., “Structural, ferroelectric and magnetic properties of $\text{Bi}_{0.85}\text{Sm}_{0.15}\text{FeO}_3$ perovskite, *Cryst. Res. and Tech.*”, 46, 238, 2011.
- [10] Khomchenko, V. A., Kiselev, D. A., “Comparative study on aging effect in BiFeO_3 thin films substituted at A and B site”, *Appl. Phys. Lett.* 90, 242901, 2007.
- [11] Xu, Q. Y., Zai, H. F., Wu, D., Qiu, T., Xu, M. X., “The magnetic properties of $\text{Bi}(\text{Fe}_{0.95}\text{Co}_{0.05})\text{O}_3$ ceramics”, *Appl. Phys. Lett.*, 95, 112510, 2009.
- [12] Chang, F. G., Zhang, N., Yang, F., Wang, S. X., Song G. L., “Effect of Cr substitution on the structure and electrical properties of BiFeO_3 ceramics”, *J. Phy. D: Appl. Phys.* 40, 7799, 2007.

- [13] Anjum, G., Kumar, R., Mollah, S., Shukla, D. K., Kumar, S.S., Lee S., “Structural, dielectric, and magnetic properties of $\text{La}_{0.8}\text{Bi}_{0.2}\text{Fe}_{1-x}\text{Mn}_x\text{O}_3$ ($0.0 < x < 0.4$) multiferroics”, *J. App.Phys.*,107, 103916, 2010.
- [14] Agarwal, R. A., Ashima, S. S., Ahlawat, N., “Structural transformation and improved dielectric and magnetic properties in Ti-substituted $\text{Bi}_{0.8}\text{La}_{0.2}\text{FeO}_3$ multiferroics”, *J. Phys. D: Appl. Phys.*,45,165001, 2012.
- [15] Rao, T. D., Asthana, S., “Evidence of improved ferroelectric phase stabilization in Nd and Sc co-substituted BiFeO_3 ”, *J. Appl. Phys.*, 116, 164102, 2014.
- [16] Basith, M. A., Kurni, O., Alam, M. S., Sinha, B. L., Ahammad, B., “Room temperature dielectric and magnetic properties of Gd and Ti co-doped BiFeO_3 ceramics”, *J. Appl. Phys.*, 115, 024102, 2014.
- [17] Kumar, M., Sati, P. C., Chhoker, S., “Grain size and Fe_2 concentration-dependent magnetic, dielectric, and magneto dielectric properties of $\text{Y}_3\text{Fe}_5\text{O}_{12}$ ceramics”, *J. Mater. Sci: Mat. Elect.*,25,5366, 2014.
- [18] Dieny, B., Speriosu, V. S., Parkin, S. S. P., Gurney, B. A., Wilhoit, D. R., Mauri, D., “Giant magnetoresistive in soft ferromagnetic multilayers”, *Phys. Rev. B.*, 43, 1297,1991.
- [19] Zhang, T., Dressel, M., “Grain size effects on the charge ordering and exchange bias in $\text{Pr}_{0.5}\text{Ca}_{0.5}\text{MnO}_3$: The role of spin configuration”, *Phys. Rev. B.*, 80, 014435, 2009.
- [20] Pradheesh, R., Nair, H. S.,Sankaranarayanan,V., Sethupathi, K., “Exchange bias and memory effect in double perovskite $\text{Sr}_2\text{FeCoO}_6$ ”, *App. Phys. Lett.*, 101,142401, 2012.
- [21] Nayak, A. K., Nicklas, M., Chadov, S., Khuntia, P., Shekhar, C., Kalache, A., Baenitz, M., Skourski, Y., Veerendra, K., Guduru, Puri, A., Zeitler, U., Felser, C.C., J.M.D., “Design of compensated ferromagnetic Heusler alloys for giant tunable exchange bias”, *Nat. Mat.*, 14, 679684, 2015.
- [22] Tian, Z. M., Yuan, S. L., Zheng, X. F., Jia, L. C., Huo, S.X., Duan, H. N., Liu, L., “Spin-glass like behavior and exchange bias in multiferroic $\text{Bi}_{1/3}\text{Sr}_{2/3}\text{FeO}_3$ ceramics”, *App. Phys. Lett.*, 96, 142516, 2010.

- [23] Yu, P., Lee, J. S., Okamoto, S., Rossell, M. D., Huijben, M., Yang, C. H., He Q., Zhang, J. X., Yang, S. Y., Lee, M. J., Ramasse, Q. M., Erni, R., Chu, Y. H., Arena, D. A., Kao, C.C., Martin, L. W., Ramesh, R., “Interface Ferromagnetism and Orbital Reconstruction in $\text{BiFeO}_3\text{-La}_{0.7}\text{Sr}_{0.3}\text{MnO}_3$ Heterostructures”, *Phys. Rev. Lett.*, 105, 027201, 2010.
- [24] Ang, R., Sun, Y. P., Luo, X., Hao, C. Y., Zhu, X. B., Song W. H., “Interface-induced magnetic coupling in multiferroic/ferromagnetic bilayer: An ultrafast pump probe study”, *J. App. Phys.*, 104, 023914, 2008.

CHAPTER 2

THEORETICAL BACKGROUND

Recently, multiferroics have been an exciting study field because of their attractive phenomena in physics and wide ranging applications. One of the most attractive characteristic of multiferroics is the magnetoelectric (ME) effect, i.e. ferroelectric polarization can be controlled by a magnetic field and, on the contrary, magnetization can be controlled by an electric field [1]. Such coexistence of magnetic and electric polarization might be exploited as an additional degree of freedom in the design of novel devices such as actuators, transducers and storage devices [2]. At the present time, the industry is trying to improve the efficiency of the computers. One of the important problems is the fabrication of data storage media with a higher data density, consequently, working on the computers becomes fast and same with the less space. From this viewpoint the current research in the field of multiferroics might be very exciting. Presently, either ferroelectric or ferromagnetic materials are used for data storage media. If in its place a multiferroic could be employed as a memory, it would include an extra dimension to the field of data storage to increase of the data density. In recent years, the development in magnetoelectric multiferroic materials is so fast that it becomes one of the new topics of materials science. Bi-containing perovskites and Hexagonal manganites becomes most examined multiferroic material. The compatibility of two materials, silicon (Si) and silicon dioxide (SiO₂) with perovskite oxides on which whole information industry is based, make these materials most promising for technological applications. Bismuth ferrite is one of the most studied single phase multiferroic materials exhibiting multiferroism at room temperature [3]. Besides, these potential applications, these materials also demonstrate exciting and complex physics. Moreover, for fabrication and integration of these materials into devices, it is essential that they should be compatible thermodynamically and chemically [4-5].

2.1 ELECTRICAL PROPERTIES OF MATERIALS

2.1.1 DIELECTRICS

A dielectric material is an electrical insulator that displays or can be made to display a polar state when subject to an applied electric field. The displacement of the center of negative charge related to the center of positive charge in a material gives rise to a dipole moment or a polar structure. A structure may display such displacements spontaneously or may be induced by an applied electric field. The polarization in an ideal dielectric material is independent of temperature and is linearly dependent on the applied electric field. Therefore, the polarization is returned to zero on the removal of applied electric field. The four main mechanisms for polarization, by which a polar state or dipole moment exists within a dielectric material, are electronic, ionic, dipolar and space charge (Figure 2.1).

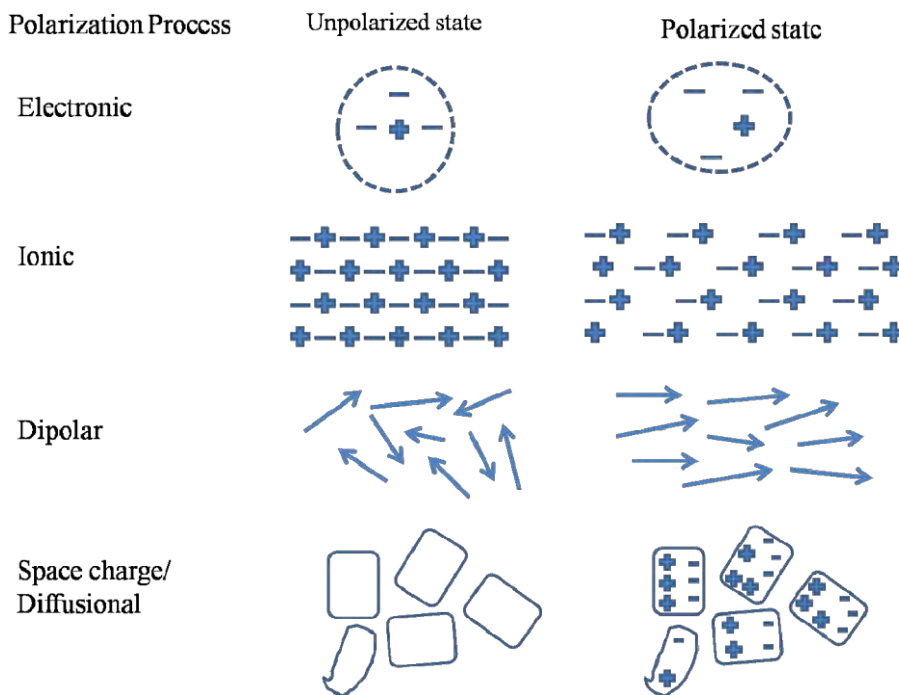


Figure 2.1: Systematic representation of possible four types of polarization process.

- (i) Electronic or atomic polarization involves a slight relative shift of the center of the electron cloud in the atom and center of positive charge (i.e. Nucleus) in an opposite direction within a dielectric material of an applied electric field. The

electronic polarization occurs when an applied electric field distorts the cloud of electrons in an atom in a direction opposite to the field.

(ii) Ionic polarization occurs in solids with ionic bonding which voluntarily have dipoles. However, the dipole moments get cancelled due to the symmetry of the crystals and the net polarization is zero in the absence of applied electric field. A small relative displacement of ions takes place from their equilibrium position in an applied electric field and hence inducing a net dipole moment or polarization [6].

(iii) Dipolar or orientational polarization happens only in polar molecules which possess permanent dipole moment. The permanent molecular dipoles present in the material are randomly distributed due to thermal randomization. However, the orientational polarization occurs due to the orientation of permanent molecular dipoles present in the material by an applied electric field [6].

(iv) Interface or space charge polarization originates due to the accumulation of charge dipoles at grain boundaries as well as the electrode material interface. It involves the limited movement of charges resulting in alignment of charges dipoles under an applied electric field.

In the above four polarization mechanism, the masses of entities to be displaced are increasing from electronic to ionic to orientational polarization and have direct relation with the frequency of applied electric field as shown in **Figure 2.2**. Obviously, heavier the particular entity more will be the time taken to displace it from one place to another. Interface or space charge polarization involves charge dipoles (defects, etc.) which are unable to follow the rapidly changing applied electric field, and hence occurs at frequencies below 100 Hz. The orientational polarization involving the moments of molecular dipoles occurs below 10^9 Hz, while ionic polarization is faster and typically happens at frequencies 10^9 - 10^{13} Hz due to involvement of ions. In contrast, ionic polarization is fastest and typically exists at frequencies between 10^{13} - 10^{15} Hz due to the involvement of lighter electrons.

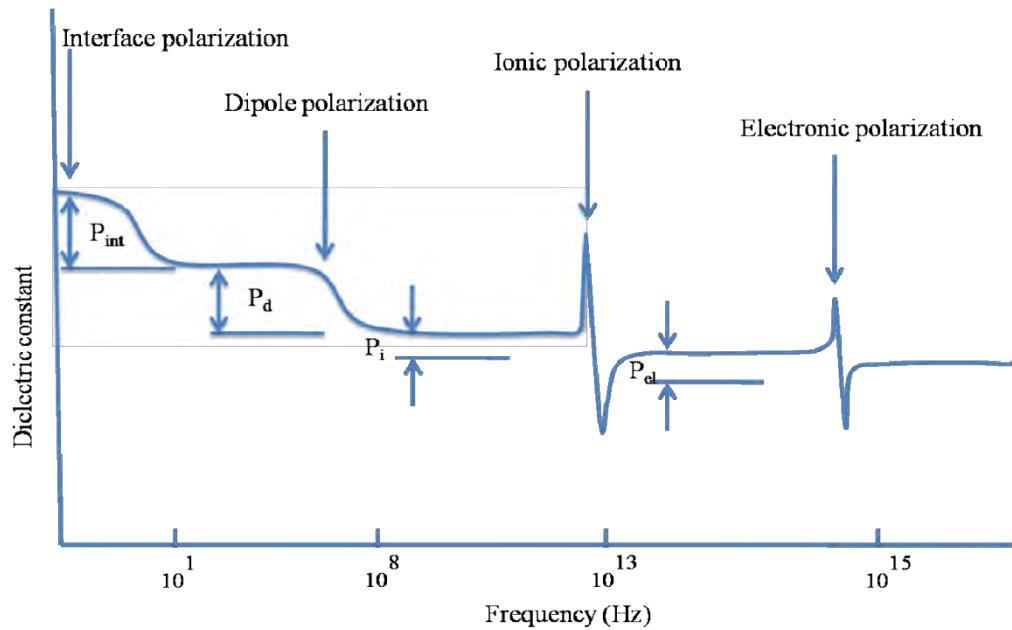


Figure 2.2 : systematic representation of various mechanisms in dielectric constant versus frequency plot.

In presence of applied electric field, the polarization induced inside a dielectric material is referred as dielectric behavior. The polarization behavior of dielectric materials increases the charge storage capacities when placed between the plates of a parallel plate capacitor. Hence, dielectric materials are extensively used in capacitors. A dipole moment developed in response to the applied field induces a buildup of charge on the surface of the dielectric material when placed between two conducting plates.

2.1.2 FERROELECTRICITY

A ferroelectric material is a nonlinear dielectric that exhibits a spontaneous electric polarization whose direction can be switched by an applied electric field [7]. A ferroelectric material undergoes a phase transition from a centrosymmetric phase at high temperature to a noncentrosymmetric phase at low temperature. Several properties of ferroelectric materials are analogous to ferromagnetic materials and therefore the prefix ferro (iron) was used to describe the property despite the fact the most ferromagnetic material do not possess iron. Amongst, 21 non centrosymmetric classes, 20 are piezoelectric out of which 10 are pyroelectric that exhibits spontaneous electric polarization which varies with temperature.

Ferroelectric materials demonstrate a hysteresis effect of polarization with an applied electric field E as shown in **Figure 2.3**. The hysteresis effect induced due to a permanent dipole moment in the material. At first, increase in electric field leads to an increase in polarization or alignment of dipoles in the direction of the applied field. When an electric field is strong enough such that all the dipoles are aligned in the direction of the applied electric field, consequently the material is in a saturated polarization state (P_s). The reduction in electric field leads to the reduction in polarization and reaches a point where electric field and polarization are zero and non-zero, respectively. Such non zero polarization at zero field is known as remnant polarization (P_r). To bring this remnant polarization to zero, the electric field is reversed in a negative direction. The reversed field at which polarization becomes zero is called a coercive field (E_c). The additional negative field will give saturation polarization P_s and upon reversal of the field the hysteresis loop closes.

Above the Curie temperature T_C , a ferroelectric material no longer exhibits spontaneous polarization (P_r) and therefore the structure becomes centrosymmetric (nonpolar) and consequently, the material becomes paraelectric. Ferroelectrics maintain their polar behaviour below T_C and show enhancement in polarizability up to T_C . Further, when the temperature of the material is decreased, many ferroelectric materials display several phase transitions. These phase transitions are between one noncentrosymmetric to another noncentrosymmetric phase and therefore exhibit a unique polar axis. The materials remain ferroelectric despite the transformations in crystal symmetry. The change in crystal symmetry leads to the change in the direction of the polar axis. The origin of ferroelectricity can be explained using the well-known example of barium titanate (BaTiO_3).

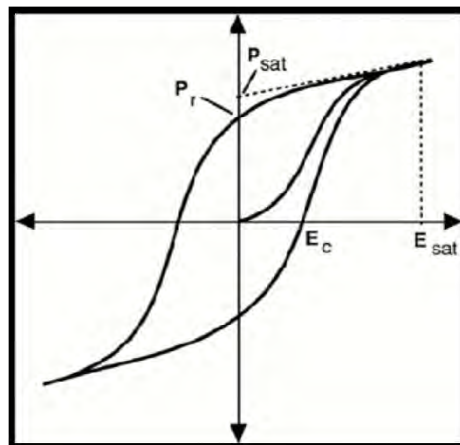


Figure 2.3: Systematic representation of ferroelectric (P-E) hysteresis loop [8].

Barium titanate is a ferroelectric material with a perovskite structure as shown in **Figure 2.4**. It has a cubic structure above $T_C \sim 120^\circ\text{C}$. It is non-ferroelectric (i.e. cubic) because the centers of positive and negative charges overlap with each other. In BaTiO_3 , below T_C , it has tetragonal structure, in which the O^{2-} ions are shifted towards negative c direction, whereas the Ti^{4+} ions are shifted towards positive c -direction. This results in formation of electric dipole along the c -direction and consequently it remains ferroelectric state in tetragonal structure.

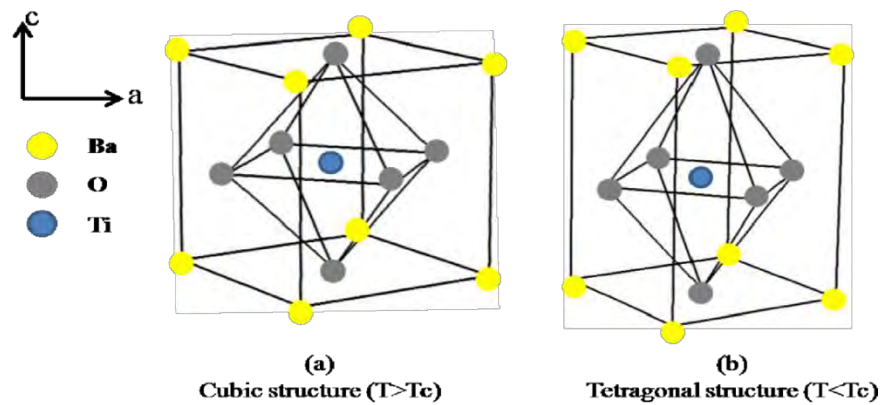


Figure 2.4 : Structure of BaTiO_3 above (a) and (b) Curie temperature(T_c)

2.2 MAGNETIC PROPERTIES OF MATERIALS

2.2.1 MAGNETIC ORDERING

Magnetism is displayed by only those compounds which possess partially filled d -transition metal elements or partially filled f -lanthanides.

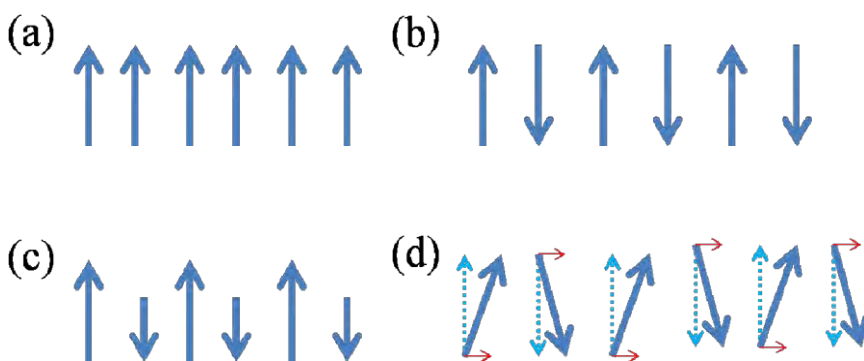


Figure 2.5: Schematic representation of spins aligned in ferromagnetic (a), antiferromagnetic (b), ferrimagnetic (c) and canted antiferromagnetic (d) manner.

The magnetic materials can be classified into various classes depending upon ordering of magnetic moments. In paramagnetic materials, magnetic moments are aligned randomly in different directions and can be aligned in one direction under the application of an external applied magnetic field. The mutual interaction of unpaired electrons leads to an alignment of electrons and therefore, results in spontaneous magnetic ordering. **Figure 2.5 (a)-(c)** illustrate three main classes of magnetic behavior. If the orientation of the spins is parallel with equal magnitude, ordering of spins is ferromagnetic (**Figure 2.5 (a)**). If the orientation of the spins is opposite with equal magnitude, ordering of spins is anti-ferromagnetic (**Figure 2.5 (b)**). If the orientation of the spins is anti-parallel with unequal magnitude, the ordering of spins is ferrimagnetic (**Figure 2.5 (c)**). Like ferrimagnetism, a residual magnetic moment survives in a canted antiferromagnet. It demonstrates the almost anti-parallel arrangement of the spins with canted spins (**Figure 2.5 (d)**) and such type of spin arrangement is termed as weak-ferromagnetism.

Depending on the interplane and intraplane couplings, three types of antiferromagnetic (AF) ordering are possible within a structure (**Figure 2.6**):

- (i) A-type AF: In A-type antiferromagnetic ordering, the intra-plane coupling is ferromagnetic while inter-plane coupling is antiferromagnetic.
- (ii) C-type AF: In C-type antiferromagnetic ordering, the intra-plane coupling is antiferromagnetic while inter-plane coupling is ferromagnetic.
- (iii) G-type AF: In G-type antiferromagnetic ordering, both intra-plane and inter-plane coupling are antiferromagnetic. For an ideal cubic perovskite type structure, each magnetic atom is surrounded by six AF neighbours in a G-type antiferromagnetic arrangement.

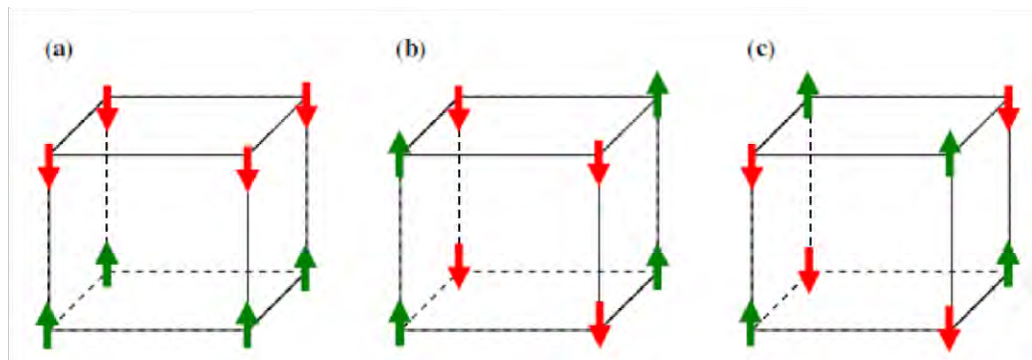


Figure 2.6: Systematic representative of spin arrangements in (a) A-type, (b) C-type and (c) G-type AF ordering.

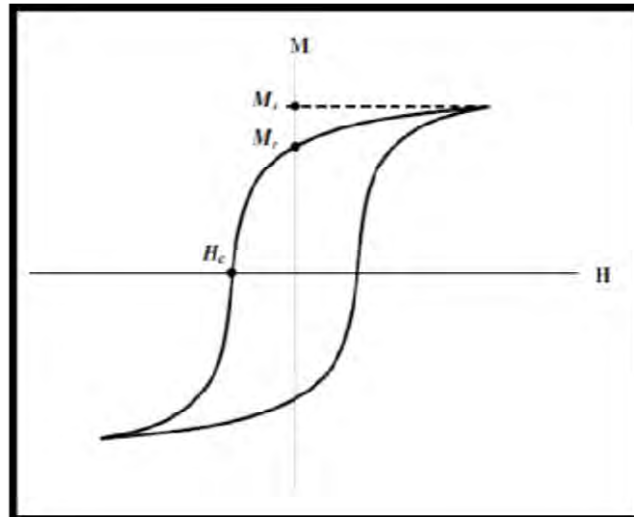


Figure 2.7: Systematic representation of ferromagnetic (M-H) hysteresis loop.

Figure 2.7 shows a characteristic hysteresis loop for ferromagnetic materials. With increasing applied external magnetic field, a ferromagnetic material becomes magnetized in one direction and the saturated magnetization (M_s) is achieved when the magnetization reaches a maximum value. The magnetization will be non-zero when the field is removed and therefore an extra magnetic field in a negative direction is required to relax the magnetization. This non-zero magnetization at zero field is known as remanant magnetization (M_r), while the coercive field (H_c) is the opposite magnetic field applied when the magnetization is relaxed to zero. If a cyclic magnetic field is applied, the magnetization will sketch a hysteresis loop. The existences of magnetic domains are responsible for the formation of magnetic hysteresis loop in any material. The materials in the large hysteresis loop area are known as hard magnetic material while the materials in small hysteresis loop area are known as soft magnetic material.

2.2.2 MAGNETIC INTERACTIONS

I. SUPER EXCHANGE

The exchange interaction between magnetic moments leads to origin of long range magnetic ordering. If neighbouring magnetic moments interact with each other, a process is referred to as a direct exchange effect. But if this procedure takes place via some midway processes it is expressed as indirect exchange or super exchange effect.

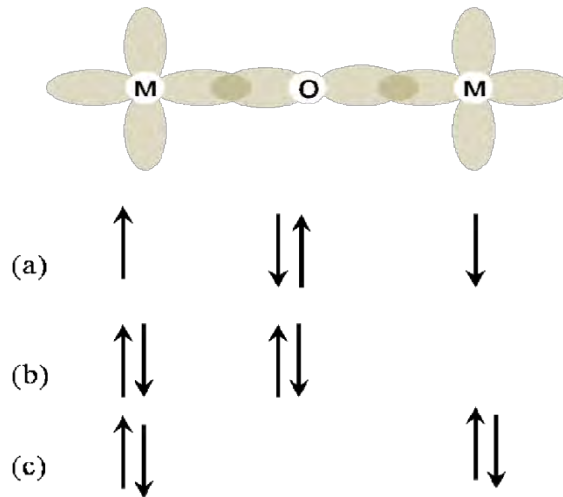


Figure 2.8(a) Separation of two magnetic moments by oxygen atom,(b-c) different possibility of antiferromagnetic alignment of magnetic moment due to super exchange effect [9].

For illustration, consider two magnetic atoms, each with a single d-orbital electron bounded by an oxygen atom. The oxygen ion has two electrons in its p-orbital which overlap with its neighbouring d-orbital, in an ionically bonded system (**Figure 2.8**). When the magnetic ions aligned antiferromagnetically, the electrons are free to move from the oxygen ion to either magnetic ion in such a way that the energy of the system will be minimized. On the other hand, due to Pauli Exclusion Principle electrons of oxygen are bounded if the magnetic ions are arranged ferromagnetically.

II. DZIALOSHINSKII-MORIYA INTERACTION

Like super exchange, Dzyaloshinskii-Moriya (DM) interaction occurs via spin-orbit interaction rather than an oxygen ion. Exchange interactions take place between the excited state of a magnetic ion and the ground state of the neighboring ion. For spins S_i and S_j , a new term in the Hamiltonian is expressed as [10]:

$$H = D \cdot (S_i \times S_j).$$

When the crystal field does not have inversion symmetry with respect to the center between S_i and S_j , Dzyaloshinskii-Moriya vector D remains finite. In antiferromagnetic structure, DM interaction is responsible for small canting of magnetic moments and consequently weak ferromagnetism occurs. The DM interaction favors non-collinear spin ordering, which has important implications for multiferroic properties.

2.3 MULTIFERROICS

The term multiferroism is used to express those materials which possess simultaneously two or all of the three properties, i.e. ferroelectricity, ferromagnetism, and ferroelasticity in the same phase. It means these materials possess spontaneous magnetization that can be reversed by an applied external magnetic field, a spontaneous electric polarization that can be reversed by an applied external electric field, and a spontaneous deformation that can be reversed by an applied external stress [11]. Multiferroic materials include specific device applications such as multistate memory devices, magnetically modulated piezoelectric transducers and electrically controlled ferromagnetic resonance devices. Moreover, the ability of coupling of magnetic and electric polarization provides an additional degree of liberty in the design of conventional transducers, actuators, and storage devices.

The description of magnetoelectric materials is much less limited compared to multiferroics. Those materials which are both electrically as well as magnetically polarizable are known as magnetoelectrics as long as these two parameters are inter-coupled directly or indirectly, such as strain-mediated magnetoelectric composites that are not even a single phase material. In small words we can say that multiferroic includes the coexistence of spontaneous ferroic orders and the coupling between them while magnetoelectrics illustrate only a close coupling phenomenon in the materials irrespective of the character of the electric and magnetic order parameters. The relationship between magnetoelectric and multiferroic materials with all possible coupling is demonstrated in **Figure 2.9**.

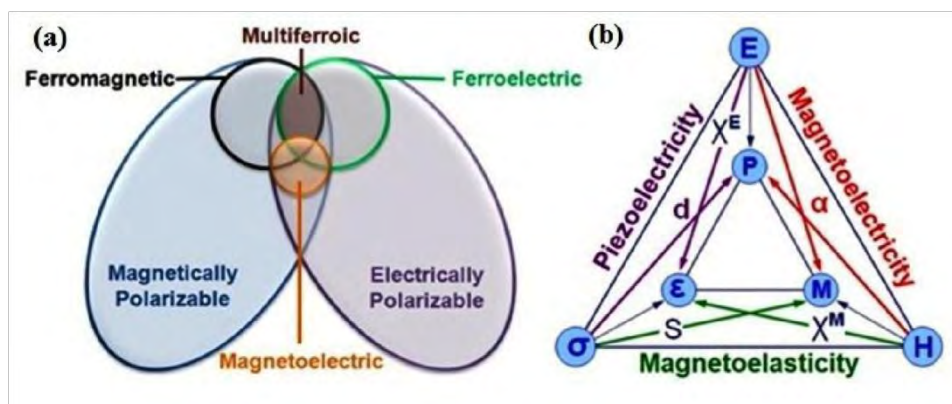


Figure 2.9: Relationship between magnetoelectric and multiferroic materials (a) and illustration of different types of possible coupling in multiferroic materials (b) [12].

2.3.1 Ferromagnetic materials

The origin of magnetism lies in the orbital and spin motions of electrons and the Pauli Exclusion Principle. The best way to introduce the different types of magnetism is to describe how materials respond to magnetic fields. According to the response to the external magnetic field, the material can be classified as

1. Diamagnetism
2. Paramagnetism
3. Ferromagnetism
4. Antiferromagnetism
5. Ferrimagnetism.

Paramagnetic materials have the characteristic of displaying disordered orientations of the magnetic moments due to thermal fluctuations. The strongest way of magnetic response is the ferromagnetic one that has the feature of showing a parallel alignment of adjacent magnetic moments. On the contrary, the antiferromagnetic behavior corresponds to an antiparallel alignment of equal moments. As a last example, we have the ferrimagnetic behavior that is characterized by antiparallel moments having different magnitudes and thus producing a non-zero net magnetic moment.

Two phenomenological theories have successfully expounded many of the ferromagnetic properties. One is the Curie-Weiss localized-moment theory [13] and the other is Stoner band theory of ferromagnetism [14]. In 1907, Weiss advanced his hypothesis that an internal 'molecular field' acts in ferromagnetic materials to align the magnetic moments parallel to each other. Weiss localized-moment theory explains the experimentally observed Curie-Weiss law behaviour for the susceptibility χ of many magnetic materials, that is to say

$$\chi = \frac{C}{T - T_c} \quad (1.1)$$

In the Stoner theory [4], ferromagnetism is also produced by the exchange interaction which is minimized if all of the spins are aligned. Opposite alignment of the spins conducts to an enhance in the band energy involved in transferring electrons from the lowest band states to band states of higher energy. This band energy does not allow

simple metals to be ferromagnetic.

Two distinct characteristics of ferromagnetic materials are their

1. Spontaneous magnetization and the existence of
2. Magnetic ordering temperature

The spontaneous magnetization is the net magnetization that is produced inside a uniformly magnetized microscopic volume when there is not a magnetic field. The value of this magnetization, at 0 K, is dependent on the spin magnetic moments of electrons.

Another related term with the spontaneous magnetization is the saturation magnetization which we can measure in the laboratory. The saturation magnetization is the maximum induced magnetic moment that can be obtained in a magnetic field (H_{sat}).

In addition to the Curie temperature and saturation magnetization, ferromagnetic materials can retain a memory of an applied field once it is removed. This behavior is called hysteresis and a plot of the variation of magnetization with magnetic field is called a hysteresis loop. There are various hysteresis parameters and they are not solely intrinsic properties but are dependent on grain size, domain state, stresses, and temperature. Ferromagnetics show a hysteretic response to an external magnetic field as shown in figure 2.10. The saturation magnetization (M_s), coercive field (H_c) and remnant magnetization (M_r) are all displayed in the figure. Based on the value of a coercive field, magnetic materials are classified into hard (large H_c) and soft (small H_c) magnets. Because hysteresis parameters are dependent on grain size, they are useful for magnetic grain sizing of natural samples.

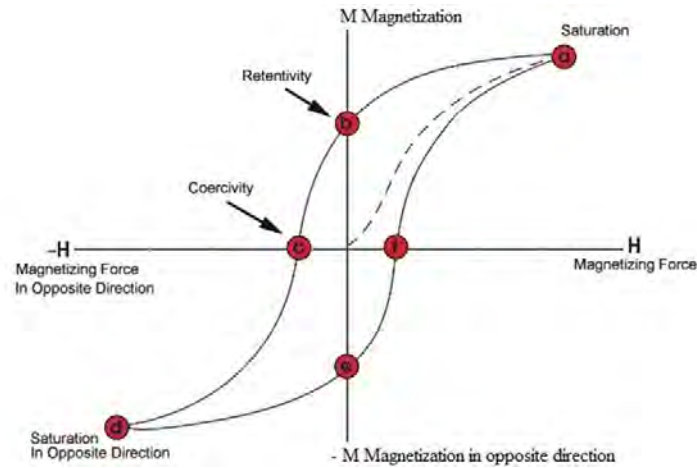


Figure 2.10: Typical hysteresis loop of a ferromagnetic material displaying magnetization switching.

Regions of a ferromagnetic material in which the magnetic dipole moments are aligned parallel are called domains. When the material is demagnetized the vector summation of all the dipole moments from all the domains equals zero. When the material is magnetized the vector summation of the dipoles gives a net magnetic moment. Thus a crystal in its ferromagnetic phase can have domain structure, with magnetic moments of domains pointing in different directions. Suppose we apply a magnetic field to such a sample. The applied field has a specific direction chosen by us. Depending on the field applied, several different responses can result from the specimen [15].

But the main outcome is that, if the applied field has a large enough magnitude, then those spontaneous magnetic moments which are oppositely or nearly oppositely oriented with respect to the direction of the applied field will switch to directions parallel or nearly parallel to the field direction. For a large enough field, practically all the magnetic moments will point along directions close to that of the applied field. The applications of ferromagnetic materials are widely related to the characteristics of their hysteresis loops. That is, a square-shaped hysteresis loop, with two stable magnetization states, is suitable for magnetic data storage, whereas a small hysteresis loop that is easily switched between the two states is suitable for a transformer core.

2.3.2 Ferroelectric materials

Ferroelectricity is the electrical analogue of the phenomenon of ferromagnetism. It was discovered in 1920, when it was known that crystals of Rochelle salt (sodium potassium tartrate tetrahydrate) have spontaneous polarization, the direction of which can be switched by the application of a strong enough electric field. This property was denominated 'ferroelectricity', by analogy with ferromagnetism, taking into account no iron or spontaneous magnetization is present in the crystal [15].

A ferroelectric material is one that experiences a phase transition from a high temperature phase (paraelectric) to a low temperature phase (ferroelectric), it has a spontaneous polarization whose direction can be reversed by an applied electric field. The existence or absence of ferroelectricity in an ionic material is determined by a balance between the short-range repulsions, which choose the nonferroelectric symmetric structure and additional bonding consideration which might stabilize the ferroelectric phase.

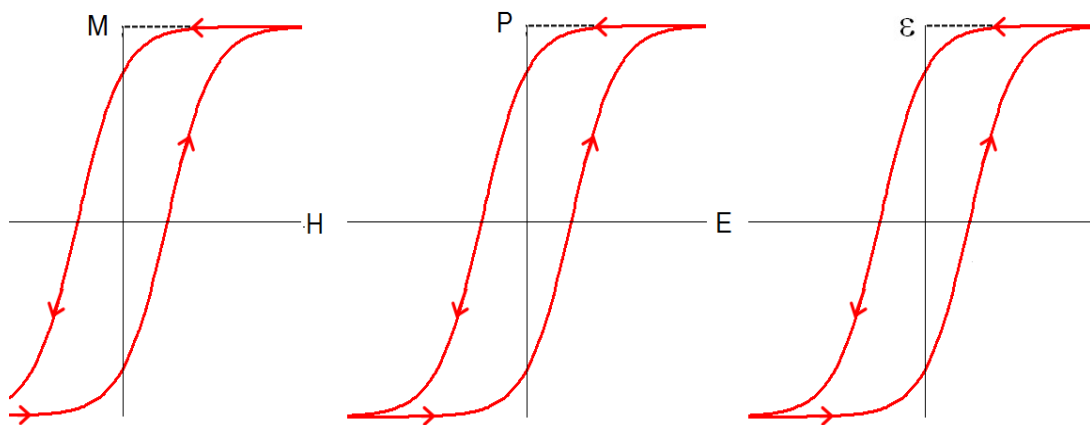


Figure 2.11: Hysteresis loops of (a) ferromagnetic, (b) ferroelectric and (c) ferroelastic materials.

The most known and used ferroelectric materials are oxides with perovskite structure, of the form ABO_3 , such as $BaTiO_3$; it is a common example of a ferroelectric crystal. Above 130°C it has a crystal structure such that a macroscopic polarization, that is, electric dipole moment per unit volume can arise in it only when an electric field is applied. It is a paraelectric phase, and the polarization is a single-valued function of

the applied electric field. Its directional symmetry is the same as that of a cube. When we cool down this substance below 130°C we find a phase transition to a crystal structure in which the centroids of the positive charges and the negative charges do not coincide, giving rise to a net dipole moment or polarization, even though there is not external electric field acting. Dielectric permittivity is a 'response function': it is a measure of how large is the response, that is to say, induced polarization, when a given electric field is applied to the material. For ferroelectrics, this response function becomes particularly large when the material is at or near the temperature of the ferroelectric phase transition. Similarly, many applications of ferromagnetic materials are based on their high magnetic permeability.

2.3.3: Ferroelastic materials

There is a mechanical or elastic analogue of ferromagnetism and ferroelectricity, and this property is called ferroelasticity. Ferroelastic crystals are, in some aspects, similar to the more familiar ferromagnetic and ferroelectric materials. Instead of spontaneous magnetization or polarization, these materials develop a spontaneous strain below a phase transition from paraelastic to ferroelastic. The transition is accompanied by critical behavior of the elastic compliance (the effective susceptibility for the strain). Ferroelastic materials are defined by having switchable domains, or twins, which may be switched on applications of an external field: stress. Such domain microstructures often result from phase transitions.

Ferroelasticity was first analyzed by physical metallurgists in the beginning of the last half of XX century in the context of the rubber like behavior of a material known as gold-cadmium and indium-thallium alloys. A formal description of ferroelasticity as an independent property in its own right, which can occur even without accompanying property of ferroelectricity or ferromagnetism, and even when no defects, are present in the crystal, was provided by the scientist Aizu in Japan in 1969 [15].

It is easy to understand ferroelastic behavior in a simple way by analyzing the case of spontaneous distortion of a square to a rectangle. We observe that the rectangle has spontaneous strain, that is, the strain is occurring and there is not an applied stress with respect to the square. A three-dimensional version of this would be a cube distorting to a square prism. This is exactly what takes place in the case of the

ferroelectric phase transition in barium titanate. So this is both a ferroelectric phase transition, as well as a ferroelastic phase transition. There is a change in the dimensions of the cube that now are different from a prism and as a result we have three possible directions that give rise to three orientation states.

According to their different character, multiferroics can be assembled in various ways. One way to classify the multiferroic materials is based on the mechanism that drives the ferroelectricity: proper and improper ferroelectrics [16] (**Table 2.1**). In proper ferroelectric multiferroics, polarization is a major effect inducing ferroelectricity and driven by hybridization and strong covalency or other purely structural effects. In improper ferroelectric, multiferroic materials, polarization is a minor effect. In these materials, ferroelectricity is determined by an electronic degree of freedom such as spin, charge or orbital ordering creating polarization as a derivative. The electronic order must be short of inversion symmetry if the ferroelectricity is to be induced. Magnetoelectric multiferroics are the case of improper ferroelectrics where polarization is created by an internal magnetic field [16-17].

Another scheme to categorize different multiferroics is based on the origin of magnetic and ferroelectric ordering: Single phase multiferroics can be classified into two groups :

- a) Type-I multiferroics
- b) Type-II multiferroics

In type-I multiferroic materials, the two order parameters have distinct sources. Some coupling exists between two order parameters, but the ferroelectric ordering temperature is commonly higher than the magnetic ordering temperature. In type-II multiferroic materials, ferroelectricity induced via magnetic ordering. In type-II multiferroics the magnetic and electric order parameters are strongly coupled because both parameters are set in the same temperature range. Polarization has typically smaller values within type-II multiferroics materials [18].

In scientific research, magnetoelectric coupling achieved more attention between all coupling effects due to its potential for a wide variety of applications. Normally, magnetoelectric coupling can be alienated into two major classes. Particularly the first one refers to magnetoelectric effect, or typically linear magnetoelectric effect. Linear magnetoelectric effect includes the induction of magnetization by an electric field or induction of polarization by a magnetic field. According to Landau theory, the induced electric polarization P and magnetization M can be expressed by the subsequent equations [12]:

$$P_i = \alpha_{ij} H_j + \beta_{ijk} H_j H_k + \gamma_{ijk} H_i E_j - \text{LLL}, \quad (1.1)$$

$$M_i = \alpha_{ij} E_j + \beta_{ijk} E_i H_j + \gamma_{ijk} E_j E_k - \text{LLL}, \quad (1.2)$$

Table 2.1: Classification of multiferroics [17].

	Methods of breaking inversion symmetry	Compounds
Proper	Covalent bonding between Ti^{4+} ($3d^0$) and O^{2-} ions	BaTiO_3
	Polarization due to $6s^2$ -lone pair of Pb or Bi	BiFeO_3 , BiMnO_3 , and $\text{Pb}(\text{Fe}_{2/3}\text{W}_{1/3})\text{O}_3$
Improper	Structural transition (Geometrical ferroelectrics)	Hexagonal RMnO_3 , Cs_2CdI_4 , K_1SeO_4
	Charge Ordering (Electronic Ferroelectrics)	LuFe_2O_4
	Magnetic ordering (Magnetic ferroelectrics)	Orthorhombic RMnO_3 , CoCr_2O_4 , RMn_2O_4 ,

Material this effect can take place only when the electric and magnetic order parameters are coupled to each other. However, this effect is very small in most single-phase materials. In composite multiferroic materials, the coupling of ferroelectricity and ferromagnetism from separate phases can be done via strain-mediated piezoelectric (electrostriction) and piezomagnetic (magnetostriction) effects

in contrast to magnetoelectric coupling in single-phase systems. It could provide orders-of-magnitude enhancement in coupling coefficient. Such linear magnetoelectric effect might discover applications in transducers, magnetic field sensors and tunable microwave devices.

The other type of magnetoelectric coupling where the electric and magnetic long range orders are strongly correlated exists only in multiferroics. Such coupling may provide magnetization reversal by electric field or polarization reversal by magnetic field. Hence, this event is referred as magnetoelectric switching [19]. A dissimilar linear magnetoelectric effect which expressed combined properties, magnetoelectric switching attains effect on a microscopic scale.

2.4 APPLICATIONS OF MULTIFERROICS

Multiferroics that display ferroelectricity and magnetism simultaneously, offer an effective approach to encode and store the data. In addition, it is more exciting to see the mutual control of electric polarization and magnetization due to its strong magnetoelectric coupling and consequently, the possible applications in spintronics, sensors etc [20].

2.4.1 MAGNETIC FIELD SENSORS

In order to develop a magnetic field sensor, the sensitivity of electric polarization (voltage) to an external magnetic field is used. Magnetoelectric materials offer different type of possibility to tune magnetic parameters with voltage. When a voltage is applied across the slab of multiferroic material, the absorption line shifted to modulate phase and amplitude of the propagating wave with the electric field. But, unfortunately, it is very difficult to switch the magnetization by an electric field. On the other hand, most of the present multiferroic materials exhibit antiferromagnetic nature with a very small macroscopic magnetic moment. Therefore, it is difficult to detect a minute effect of external electric field on magnetization and the corresponding change in electric polarization directly.

2.4.2 ELECTRIC FIELD CONTROL OF EXCHANGE BIAS

The utilization of multiferroics in controlling the transport behavior of spin valve structures could be a promising direction towards its potential applications.

Generally, there are two types of exchange interactions at the interface of antiferromagnetic core and ferromagnetic surface. First one is the exchange bias of magnetic hysteresis due to the pinning of uncompensated spin at the interface, which comes under the practical interest of usual antiferromagnetic layer in spin-valve structures [21]. This type of exchange bias shifts hysteresis loop along the axis of the magnetic field for the ferromagnetic layers. The second type of exchange bias is associated with enhancement of coercivity of the ferromagnetic layer due to increasing spin viscosity or spin drag effect.

2.4.3 MULTIFERROIC-SEMICONDUCTOR HETEROSTRUCTURES AS SPIN FILTERS

Multiferroic semiconductor heterostructures are very interesting due to their some novel effects. A lot of effort has been done to synthesize and characterize YMnO_3 thin films to use it as a potential gate dielectric in semiconductor devices [21]. YMnO_3/GaN heterostructure is the most studied systems because both YMnO_3 and GaN possess hexagonal symmetry. Up to that time, not much interest has been paid to the role of the heterostructure interface. According to first principle calculation, in antiferromagnetically ordered YMnO_3 and GaN there are different band offsets for spin-up and spin-down states at the interface. This type of behavior associated to spin splitting of the valence band induced at the interface. The dependence of energy barrier on the relative orientation of electric polarization relative to the polarization direction of GaN substrate leads an opportunity for producing a magnetic tunnel junction in the hetero structure.

2.4.4 MULTISTATE MEMORY DEVICES

In the case of memory devices, multiferroic materials that can be integrated into semiconductor devices are of great interest, not only in high-density ferroelectric memory devices (FeRAM) and ferroelectric field-effect transistors (FeFET-RAM), but also in the concept of four-state memories. In recent years, one of the typical device for ferroelectric applications is ferroelectric random-access memories (FeRAMs) having 5ns access speed and 64M byte memory density [20]. But the major disadvantage of FeRAMs is destructive read and reset operation. On the other hand, magnetic random access memories (MRAMs) have lagged far behind FeRAMs, due

to its slow and high power read-write operation. But in multiferroic materials, we can combine the advantages of both FeRAMs and MRAMs in order to get electrically erasable programmable read only memories (EEPROMs) [20].

2.5 : SINGLE PHASE MULTIFERROIC COMPOUNDS

2.5.1 BISMUTH FERRITE (BiFeO_3)

Due to the simplicity of their crystal structure and a large variety of compositions, perovskite and perovskite-like structures have become the foundation for the design of numerous functional materials. One of the most studied multiferroics with the perovskite structure is bismuth ferrite (BiFeO_3). Amongst the various magnetoelectric (ME) materials, BiFeO_3 (BFO) with ABO_3 -type perovskite structure is the rarest single phase multiferroics. BiFeO_3 is widely studied multiferroics because it possesses magnetoelectric (ME) coupling at room temperature. It was first synthesized by Royen and Swars in 1957.

2.5.2 CRYSTAL STRUCTURE OF BiFeO_3

In perovskite (ABO_3) type BiFeO_3 structure, Fe^{3+} ions are situated at B-sites surrounded by six neighboring oxygen ions to form FeO_6 octahedra that are associated with each other by sharing their corners as shown in **Figure 2.12**.

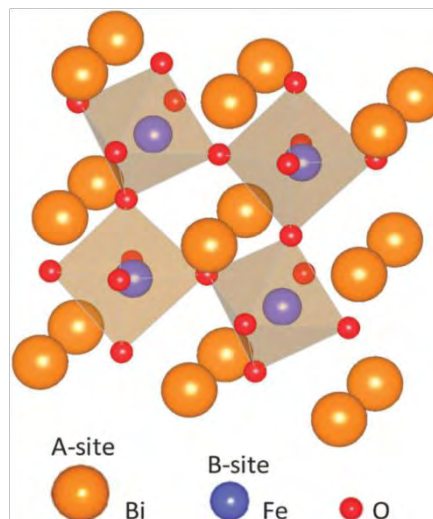


Figure 2.12: The perovskite crystal structure of BiFeO_3 .

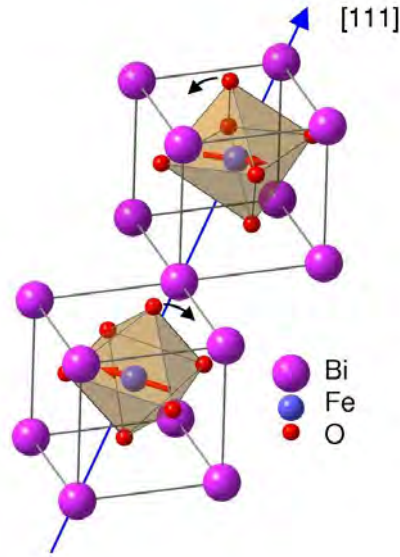


Figure 2.13: Crystal structure of bulk BiFeO_3 with opposite rotation of successive oxygen octahedral around $[111]$ polar axes. Red arrow indicates orientation of Fe magnetic moments in (111) plane[23].

Bismuth ions (Bi^{3+}) occupy empty spaces between FeO_6 backbones. Such perovskite structures are formed by occupying B-sites by transition metal elements while A-sites are occupied by trivalent rare earth element or alkali earth metals [22]. The Physical properties of such perovskite structures, mainly, depend on the transition metal element located at B-sites. Furthermore, the electronic band formation and electronic conduction are mostly affected by chemical bonding between Fe^{3+} and oxygen ions [22]. In bulk form BFO is known to be ferroelectric-antiferromagnetic multiferroic with a ferroelectric Curie temperature of $T_C \sim 1103$ K and antiferromagnetic Néel temperature of $T_N \sim 643$ K [19]. Bulk BFO can be described as a rhombohedrally distorted ferroelectric perovskite with $R3c$ space group as shown in **Figure 2.13**. The lattice parameters of the rhombohedral unit cell are $a = 5.59$ Å and $\alpha = 60.68^\circ$ [23]. In such a distorted perovskite structure, $R3c$ symmetry allow spontaneous polarization (P_s) along the pseudo cubic $[111]$ direction [24].

An important parameter used to determine the fitness of ions into the perovskite unit cell is defined by ratio $(r_{\text{Bi}^{3+}} + r_{\text{O}})/l$, known as rotation angle of the oxygen octahedra or octahedra tilting angle [25]. Here, r represents an ionic radius of respective ion and l define the length of octahedral edge. This angle would be zero for cubic perovskite with perfectly matched ionic sizes. It is entirely comparable to the normally used Goldschmid tolerance factor (t) defined as $t = (r_{\text{Bi}^{3+}} + r_{\text{O}})/(r_{\text{Fe}^{3+}} + r_{\text{O}})$ [26]. Using ionic radii of Shannon, t has been reported to be 0.88 for BiFeO_3 with Bi^{3+} ions in eight fold coordination and Fe^{3+} ions in six fold coordination and high spin [25]. When t is

smaller than one, the oxygen octahedra tend to buckle in order to get fit into the unit cell [25]. For BiFeO_3 , the octahedral tilting angle is found to be $\sim 11\text{-}14^\circ$ around the polar [111] axis, with directly related Fe-O-Fe angle, equal to around $154\text{-}156^\circ$ [27].

The Fe-O-Fe angle is essential because not only it controls both magnetic exchange and orbital overlap between Fe and O ions, but, also determines magnetic ordering temperature and conductivity [27]. In that case, the reduction in the tolerance factor by the substitution of smaller ionic radii A-site ions would induce more buckling in FeO_6 octahedra by improving insulating behavior [22]. Since most of the rare earth ions have a smaller ionic radii compared to Bi^{3+} ion, therefore substitution of these ions is expected to bring a more insulating behavior in bismuth ferrite [22]. But, a large variation in t value from 1 by the substitution of too small A-site ions would cause the chemical structure unstable that will be corresponded to the late lanthanide based perovskites having a tendency to be hexagonal perovskites rather than a normal perovskite [22].

2.5.3 FERROELECTRICITY IN BiFeO_3

Bulk BiFeO_3 is known to be exhibited ferroelectric ordering below Curie temperature $T_C \sim 1103$ K. Both X-ray and neutron diffraction studies confirmed the ferroelectric phase of BFO. The origin of ferroelectricity in BFO can be understood its highly distorted perovskite structure with rhombohedral symmetry and space group $R3c$. As shown in **Figure 2.13**, the primitive unit cell contains two formula units (ten atoms), arising from counter rotations of neighboring oxygen octahedra around [111] axis [28]. The $R3c$ symmetry allows development of a spontaneous polarization along [111] direction in such a way that Bi, Fe, and O are displaced relative to one another along [111] axis [28]. The largest relative displacements take place in Bi relative to O, which is consistent with a stereochemically active Bi $6s^2$ lone pair compared to cubic perovskite [29]. The polar displacements in BFO are very large in comparison of non lone-pair active perovskite ferroelectrics such as BaTiO_3 and KNbO_3 , but consistent with those observed for other bismuth based perovskite structures [30]. According to first principle calculations, it has been reported that BFO has a large spontaneous polarization (P_s) of the order $\sim 90\text{-}100 \mu\text{C}/\text{cm}^2$ for a rhombohedral structure with $R3c$ space group and around $150 \mu\text{C}/\text{cm}^2$ for tetragonal structure. But, experimentally

observed spontaneous polarization is found to be much lesser than theoretically predicted values [25]. This discrepancy in the values of polarization is attributed to the presence of secondary phases, defects, volatilization of the bismuth atoms at high temperatures, electron hopping between Fe ions that lead to high leakage current.

2.5.4 FERROMAGNETISM IN BiFeO_3

With $R3c$ space group, BiFeO_3 exhibits antiferromagnetic ordering below Neel temperature $T_N \sim 643$ K. The magnetic structure of BFO is a G-type antiferromagnetic, where spin is provided by the transition metal Fe^{3+} ions. In this arrangement, each Fe spins is surrounded by six antiparallel nearest neighbor Fe spins as shown in **Figure 2.14**. It means that Fe magnetic moments are ferromagnetically coupled within (111) plane, while antiferromagnetically aligned within adjacent planes [31]. However, it was observed that the antiferromagnetic spin structure of BFO is modified by a long rang modulation of 62 nm leading to a spin cycloid structure, also known as spiral modulated spin structure (SMSS) (**Figure 2.15**) [31]. This spiral modulated spin structure leads to cancellation of any macroscopic magnetization. As $R3c$ space group allows the linear magnetoelectric effect, but at the same time SMSS prohibited linear magnetoelectric effect while allowed second order magnetoelectric effect. According to Dzyaloshinski-Moriya (D-M) interaction theory, the domain walls of BFO might show a weak ferromagnetic moment if Fe moments are oriented perpendicular to [111] direction as shown in **Figure 2.16** [10]. However, this theory has not been established so far [3].

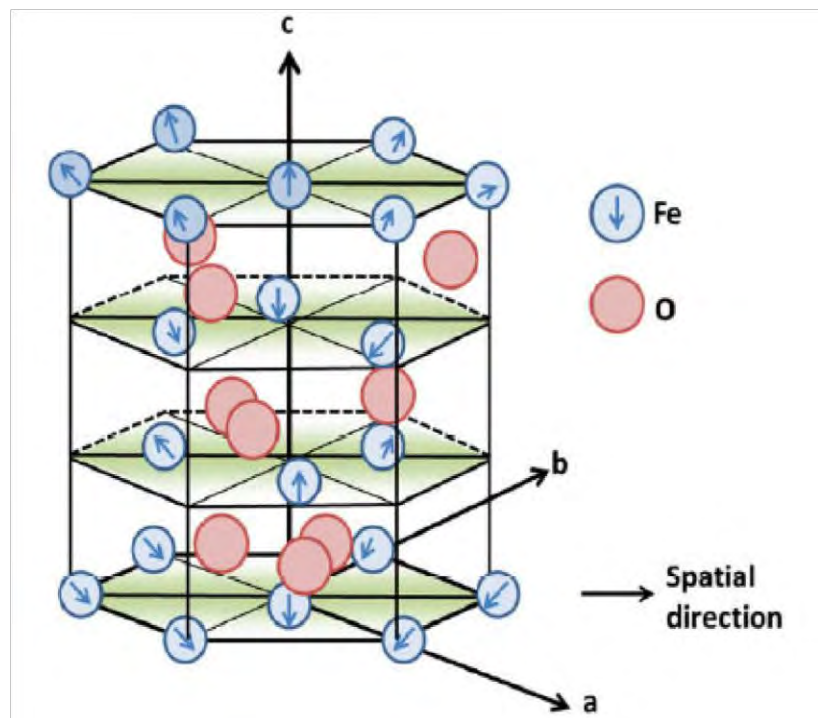


Figure 2.14: Hexagonal structure of BiFeO_3 lattice with Fe^{3+} and O^{2-} ions. The arrows indicate direction of Fe spins .

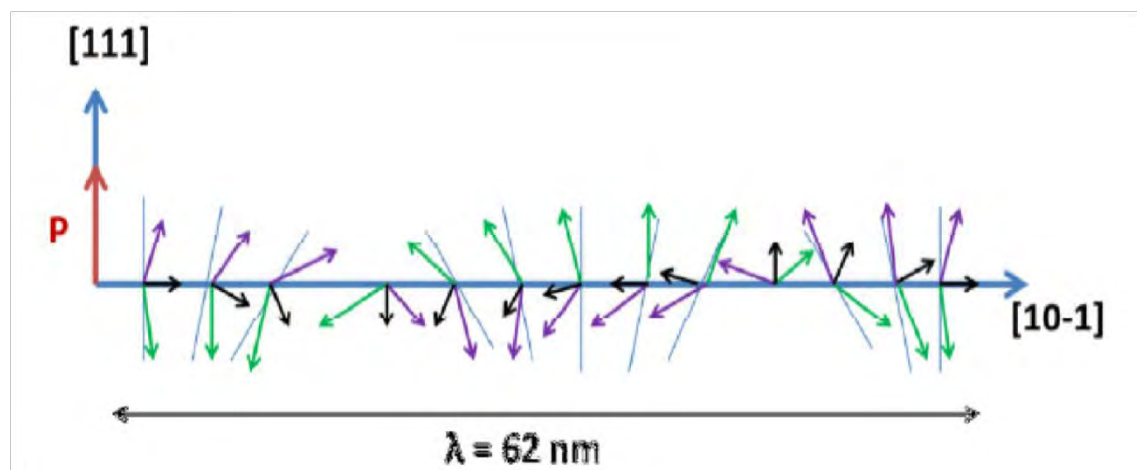


Figure 2.15: Schematic representations of spiral spin structure of wavelength $\lambda = 62 \text{ nm}$. The canted antiferromagnetic spins (purple and green arrows) give rise to a net magnetic moment (black arrows) which spatially averaged out to zero due to the cycloid rotation .

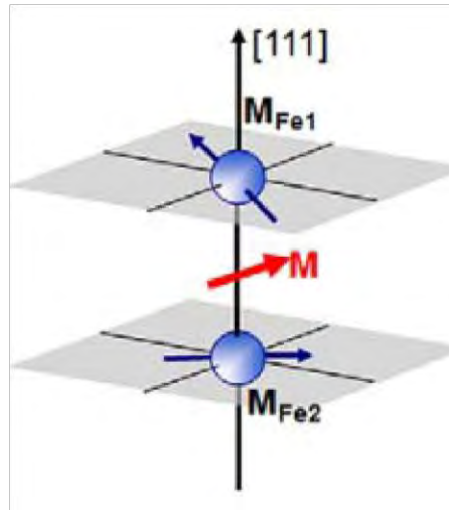


Figure 2.16: Representation of weak ferromagnetism in BFO due to D-M interaction .

2.5.5 MAGNETOELECTRIC COUPLING IN BiFeO_3

The importance of multiferroic bismuth ferrite lies in the coupling between the electric and magnetic order parameters rather than a simple sum-up of the individual properties. The cycloidal modulation of the spiral spin structure prevents a macroscopic weak ferromagnetism as well as hides the observation of the linear magnetoelectric effect. At large magnetic fields >20 Tesla, the cycloidal modulation is suppressed and consequently the observation of linear magnetoelectric coupling is possible. As the ferroelectric polarization can couple to magnetic gradients and induce the spin cycloid, therefore, ferroelectric polarization is believed to be responsible for the origin of the cycloidal spin structure.

It can be considered as the opposite effect of the polarization induced by spiral magnetic order in improper ferroelectric multiferroics [32-33]. It is known that bismuth ferrite is a proper ferroelectric with weak ferromagnetism due to the Dzyaloshinskii-Moriya (DM) interaction, ferroelectric control of the magnetic structure is obviously more feasible than vice versa, as e.g. demonstrated in TbMnO_3 [34]. On the basis of theoretical studies of bismuth ferrite, it has been established that the direction of the weak ferromagnetic moment can be reversed by switching the direction of antiferro distortive rotation of the FeO_6 octahedra, but it remains invariant under 180° switching of the direction of polar displacements of the Bi^{3+} and Fe^{3+} cations [19].

2.5.6 CHALLENGES WITH BiFeO₃

Despite the advantages of being exhibiting room temperature ferroelectricity and antiferromagnetism (or weak ferromagnetism), BFO suffers many serious drawbacks like low values of polarization and magnetization, high conductivity due to leakage current, the formation of secondary phase, the presence of oxygen and bismuth vacancies etc, which limit the potential applications of BFO in devices [25]. According to phase diagram analysis of the Bi₂O₃-Fe₂O₃ binary system, BiFeO₃ is a linear compound prepared from equal parts of bismuth oxide (Bi₂O₃) and iron oxide (Fe₂O₃) [25]. A slight difference in stoichiometric ratio can produce several types of secondary phases such as Bi₂Fe₄O₉ (mullite phase), Bi₂₄Fe₂O₃₉, Bi₃₆Fe₂O₅₇, Bi₄₆Fe₂O₇₂, or a sillenite type phase (Bi₂₅FeO₄₀) and parasite ferromagnetic phase Fe₂O₃ due to volatilization of bismuth at high temperature and valence fluctuation in Fe ion from Fe²⁺ to Fe³⁺ [35-37]. BFO is very prone to show parasite phases and therefore it has a tendency to nucleate at grain boundaries and give rise to impurities. However, it has also been reported that BiFeO₃ phase is metastable along with optically visible impurity spots appearing well below the melting temperature [38]. The synthesis of single phase BiFeO₃ is still under examination. Although, a small fraction of impurities does not affect significantly the structural and magnetic properties of BiFeO₃, but it can alter its dielectric, electrical and optical properties. Due to volatilization of bismuth atoms, electron hopping between Fe ions, and conducting parasites phase, BFO exhibits high dielectric loss and large leakage current. Moreover, BFO exhibits lossy ferroelectric loops with small remnant polarization and large coercive fields. The absence of saturated ferroelectric loop in BFO hinders its potential applications at room temperature. In addition, the electromechanical coefficients of BFO are much smaller than those reported for traditional lead-based compositions like PZT owing to large leakage current [39]. Therefore, it becomes necessary to adopt artificial method for the formation of pure BFO compounds. Furthermore, a large number of other problems in BFO such as antiferromagnetic nature, low magneto-electric (ME) coupling coefficients, large differences between T_C (Curie temperature) and T_N (Neel temperature) remains to be overcome to the technological point of view [25]. The major problem is the G-type canted antiferromagnetic ordering with an incommensurate space modulated spiral spin structure of 62 nm that inhibits the observation of any linear ME effect in BFO [19].

In order to overcome these problems much efforts have been devoted which include the chemical substitution of rare earth ions (like Eu³⁺, Sm³⁺, Gd³⁺) [40] or divalent ions (like Pb²⁺, Sr²⁺, Ca²⁺) [41-42] at the A site and doping of nonmagnetic ions (like Ti⁴⁺, Nb⁵⁺) [43,46] at the B site of BFO have proved effective ways to enhance multiferroic

properties. Furthermore, attempts have also been made towards fabrication of different solid solution composites and multilayer structures of BFO with other ABO_3 based perovskites materials such as $BaTiO_3$ - $BiFeO_3$ [43] and $PbTiO_3$ - $BiFeO_3$ [44] which leads to favorable structure distortion resulting in enhanced electrical and ferroic properties [37]. However, site engineering technique with substitution of dopants either at A-site or B-site in BFO perovskite cell is the most successful and effective approach. This is because a slight change in atomic composition can produce large distortion within perovskite unit cell that might have dramatic impacts on the properties of the material such as structural evolution, transport properties, magnetic properties and polarization [45].

References:

- [1] Mitoseriu, L., "Magnetoelectric phenomena in single-phase and composite systems", *Bol. Soc. Esp. Ceram. V.*, vol. 44, pp. 177, 2005.
- [2] Zheng, H., Wang, J., Lofland, S.E., et al., "Multiferroic BaTiO₃-CoFe₂O₄ Nanostructures", *Science*, vol. 303, pp. 66, 2004
- [3] Zhao, T., Scholl, A., Zavaliche, F., et al., "Electrical control of antiferromagnetic domains in multiferroic BiFeO₃ films at room temperature", *Nature mater.*, vol 5, pp. 823, 2006.
- [4] Schlom, D.G., Haeni, J.H., "A thermodynamic approach to selecting alternative gate dielectrics", *Mater. Res. Bull.*, vol. 27, pp. 198, 2002.
- [5] Hubbard, K.J., Schlom, D.G., "Thermodynamic stability of binary oxides in contact With silicon", *J. Mater. Res.*, vol. 11, pp. 2757, 1996.
- [6] Moulson, A.J., Herbert, J.M., "Electroceramics: Materials, Properties and Applications", 2nd Edition. Chichester, UK: John Wiley and Sons Ltd., 2003.
- [7] Jaffe, B., Cook, W. R., Jaffe, H., "Piezoelectric Ceramics", New York, Academic Press, 1971.
- [8] Polla, D.L., "Processing and characterization of piezoelectric materials and integration into microelectromechanical systems", *Annu. Rev. Mater. Sci.*, vol. 28, pp. 563, 1998.
- [9] Blundell, S., "Magnetism in Condensed Matter", Oxford University Press, 2001.
- [10] Moriya, T., "Anisotropic Super exchange Interaction and Weak Ferromagnetism", *Phys. Rev.*, vol. 120, pp. 91, 1960.
- [11] Hill, N.A., "Why Are There so Few Magnetic Ferroelectrics?", *J. Phys. Chem. B*, vol. 104, pp. 6694, 2000.
- [12] Martin, L.W., Crane, S.P., Chu, Y.H., Holcomb, M.B., Gajek, M., Huijben, M., Yang, C.H., Balke, N., Ramesh, R., "Multiferroics and magnetoelectrics: thin films and nanostructures", *J. Phys. Condens. Matter*, vol. 20, pp. 434220, 2008
- [13] Cullity, B.D., "Introduction to magnetic materials". Addison-Wesley Publishing Company, pag151, 1972.

- [14] Cullity, B.D., "Introduction to magnetic materials", Addison-Wesley Publishing Company, pag136, 1972.
- [15] Wadhawan, V.K., *Ferroic Materials: A Primer*, Resonance, 7, Number 6, 15-24, July 2002.
- [16] Picozzi, S., Ederer, C., "First principles studies of multiferroic materials", *J. Phys.: Condens. Matter*, vol. 21, pp. 303201, 2009.
- [17] Cheong, S.W., Mostovoy, M., "Multiferroics: a magnetic twist for ferroelectricity", *Nature Mater.*, vol. 6, pp. 13, 2007.
- [18] Brink, J.V.D., Khomskii, D.I., "Multiferroicity due to charge ordering", *J. Phys.: Condens. Matter*, vol. 20, pp. 434217, 2008.
- [19] Ederer, C., Spaldin, N.A., "Weak ferromagnetism and magnetoelectric coupling in bismuth ferrite", *Phys. Rev. B*, vol. 71, pp. 060401, 2005.
- [20] Wang, K.F., Liu, J.M., Ren, Z.F., "Multiferroicity: the coupling between magnetic and polarization orders", *Adv. Phys.*, vol. 58, pp. 321, 2009.
- [21] Nogues, J., Schuller, I.K., "Exchange bias", *J. Magn. Magn. Mater.*, vol. 192, pp. 203, 1999.
- [22] Yang, C.H., Kan, D., Takeuchi, I., Nagarajan, V., Seidel, J., "Doping BiFeO₃: approaches and enhanced functionality", *Phys. Chem. Chem. Phys.*, vol. 14, pp. 15953, 2012.
- [23] Lubk, A., Gemming, S., Spaldin, N.A., "First-principles study of ferroelectric domain walls in multiferroic bismuth ferrite", *Phys. Rev. B*, vol. 80, pp. 104110, 2009.
- [24] Porporati, A.A., Tsuji, K., Valant, M., Axelsson, A.K., Giuseppe, P., "Raman tensor elements for multiferroic BiFeO₃ with rhombohedral R3c symmetry", *J. Raman Spectrosc.*, vol. 41, pp. 84, 2010.
- [25] Catalan, G., Scott, J.F., "Physics and Applications of Bismuth Ferrite", *Adv. Mater.*, vol. 21, pp. 2463, 2009.
- [26] Goldschmidt, V.M., "Die Gesetze der Krystallochemie", *Naturwissenschaften*, vol., 14, pp. 477, 1926.

- [27] Kubel, F., Schmid, H., "Structure of a ferroelectric and ferroelastic mono domain crystal of the perovskite BiFeO_3 ", *ActaCryst. B*, vol. 46, pp. 698, 1990.
- [28] Neaton, J.B., Ederer, C., Waghmare, U.V., Spaldin, N.A., Rabe, K.M., "First-principles study of spontaneous polarization in multiferroic BiFeO_3 ", *Phys. Rev. B*, vol. 71, pp. 014113, 2005.
- [29] Seshadri, R., Hill, N.A., "Visualizing the role of Bi 6s "lone pairs" in the off-center distortion in ferromagnetic BiMnO_3 ", *Chem. Mater.*, vol. 13, pp. 2892, 2001.
- [30] Íñiguez, J., Bellaiche, L., Vanderbilt, D., "First-principles study of $(\text{BiScO}_3)_{1-x}(\text{PbTiO}_3)_x$ piezoelectric alloys", *Phys. Rev. B*, vol. 67, pp. 224107, 2003.
- [31] Sosnowska, I., Neumaier, T. P., Steichele, E., "Spiral magnetic ordering in bismuth ferrite", *J. Phys. C.*, vol. 15, pp. 4835, 1982.
- [32] Popov, Y.F., Zvezdin, A.K., Vorobev, G.P., Kadomtseva, A.M., Murashev, V.A., Rakov, D.N., "Linear Magnetoelectric Effect and Phase Transitions in Bismuth Ferrite, BiFeO_3 " *JETP Lett.*, vol. 57, pp. 69, 1993.
- [33] Kadomtseva, A.M., Zvezdin, A.K., Popov, Y.F., Pyatakov, A.P., Vorob'ev, G.P., "Space time parity violation and magnetoelectric interactions in antiferromagnets", *JETP Lett.*, vol. 79, pp. 571, 2004.
- [34] Kimura, T., Goto, T., Shintani, H., Ishizaka, K., Arima, T., Tokura Y., "Magnetic control of ferroelectric polarization", *Nature*, vol. 426, pp. 55, 2003.
- [35] Lahmara, A., Zhao, K., Habouti, S., Dietze, M., Solterbeck, C.H., Sounia, M.Es., "Off stoichiometry effects on BiFeO_3 thin films", *Solid State Ionics*, vol. 202, pp. 1, 2011.
- [36] Das, S., Basu, S., Mitra, S., Chakravorty, D., Mondal, B.N., "Wet chemical route to transparent BiFeO_3 films on SiO_2 substrates", *Thin Solid Films*, vol. 518, pp. 4071, 2010.

- [37] Kumar, M. M., Palker, V. R., Srinivas, K., Suryanarayana, S. V., “Ferroelectricity in a pure BiFeO₃ ceramics”, *Appl. Phys. Lett.*, vol. 76, pp. 2764, 2000.
- [38] Palai, R., Katiyar, R. S., Schmid, H., Tissot, Clark, S. J., Robertson, J., Redfern, S. A. T., Catalan, G., Scott, J. F., “ β phase and γ - β metal insulator transition in multiferroic BiFeO₃”, *Phys. Rev. B*, vol. 77, pp. 014110, 2008.
- [39] Cheng, C.J., Kan, D., Lim, S.H., McKenzie, W.R., Munroe, P.R., Riba, L.G.S., Withers, R.L., Takeuchi, I., Nagarajan, V., “Structural transitions and complex domain structures across a ferroelectric to antiferroelectric phase boundary in epitaxial Sm-doped BiFeO₃ thin films”, *Phys. Rev. B*, vol. 80, pp. 014109, 2009.
- [40] Khomchenko, V.A., Kiselev, D.A., Bdikin, I.K., Shvartsman, V.V., Borisov, P., Kleemann, W., Vieira, J.M., Kholkin, A.L., “Crystal structure and multiferroic properties of Gd substituted BiFeO₃”, *Appl. Phys. Lett.*, vol. 93, pp. 262905, 2008.
- [41] Mazumder, R., Sen, A., “Effect of Pb doping on dielectric properties of BiFeO₃ ceramics”, *J. Alloys Compd.*, vol. 475, pp. 577, 2009.
- [42] Catalan, G., Sardar, K., Church, N.S., Scott, J.F., Harrison, R.J., Redfern, S.A.T., “Effect of chemical substitution on the Néel temperature of multiferroic Bi_{1-x}Ca_xFeO₃”, *Phys. Rev. B*, vol. 79, pp. 212415, 2009.
- [43] Wei, J., Haumont, R., Jarrier, R., Berhtet, P., Dkhil, B., “Nonmagnetic Fe site doping of BiFeO₃ multiferroic ceramics”, *Appl. Phys. Lett.*, vol. 96, pp. 102509, 2010.
- [44] Buscaglia, M. T., Mitoseriu, L., Pellechi, L., Buscaglia, V., Viviani, M., Siri, A.S., “Preparation and characterisation of the magneto-electric xBiFeO₃-(1-x)BaTiO₃ ceramics”, *J. Eur. Ceram. Soc.*, vol. 26, pp. 3027, 2006.

- [45] Singh, K., Negri, N.S., Kotnala, R.K., Singh, M., “Dielectric and magnetic properties of $(\text{BiFeO}_3)_{1-x} - (\text{PbTiO}_3)_x$ ferromagnetoelectric system”, *Solid State Commun.* vol. 148, pp. 18, 2008.
- [46] Jun, Y.K., Moon, W.T., Chang, C.M., Kim, H.S., Ryu, H.S., Kim, J.W., Kim, K.H., Hong, S.H., “Effects of Nb doping on electric and magnetic properties in multiferroic BiFeO_3 ceramics”, *Solid State Commun.*, vol. 135, pp. 133, 2005.




Chapter 3

Sample Preparation

3.1 Sample preparation

3.1.1 Introduction

Ferrites can be prepared by a wide variety of forms polycrystalline, aggregates, thin and thick films, single crystals. Preparation methods have been developed to prepare ferrites with specific microstructures. The preparation of polycrystalline ceramics with optimum desired properties is still a complex and difficult task and the control of the chemical composition, homogeneity and microstructure are very crucial. As the most of the properties needed for ceramics applications are not intrinsic but extrinsic, preparation of samples has to encounter added complexity. Now a day, the majority of ceramic powders are made by the conventional ceramic process or standard solid state reaction technique. Most of the non-conventional process are involved in producing the powder. The four basic operations in the ceramic method are shown schematically shown in below.

Ceramic method	Basic operations	New methods
Miling of raw materials	Powder preparation 	Coprecipitation Precursor routes Sol-gel methods Spray-drying Freeze-drying Combustion synthesis Glass crystallization
Uniaxial pressing	Green body forming 	Isostatic pressing Slip casting
Solid state sintering	Sintering 	Hot isostatic pressing Liquid phase sintering Microwave sintering
Surface treatment	Finishing	Laser annealing

Here, the standard solid state reaction technique that will be used in this research work has been described.

3.1.2 Standard solid-state reaction technique

The preparation of polycrystalline solids from a mixture of solid starting materials is known as solid-state reaction. Solids do not react together at room temperature over normal time scales and it is necessary to heat them to much higher temperatures, often to 1000 to 1500 °C in order for the reaction to occur at an appreciable rate because temperature provides the necessary energy for the reaction to occur. The factors on which the feasibility and rate of a solid state reaction depend include reaction conditions, structural properties of the reactants, surface area of the solids, their reactivity and the thermodynamic free energy change associated with the reaction. Solid-state reaction occurs much more quickly with increasing temperature and reaction does not normally occur until the reaction temperature reaches at least 2/3 of the melting point of one of the reactants.

In solid-state reaction method, raw materials are weighted out according to the stoichiometry of the compound with due consideration for impurity and moisture contents. Raw materials are mechanically mixed and then grinding operations are performed to control the particle size and to make the mixture homogeneous. For this purpose milling operation is performed which can reduce the particle size to 1-10µm range. Sufficient amount of some volatile organic liquid preferably acetone or alcohol is added to the mixture to aid homogenization. This forms a paste which is mixed thoroughly. During the process of grinding and mixing, the organic liquid gradually volatilizes and has usually evaporated completely after 10 to 15 minutes.

Since ferrites possess a very high melting temperature, both reaction and densification usually take place in solid state. Initial formation of the product occurs at the contact surface between particles of the two reactants.

The flow chart for the preparation of samples by solid state reaction technique is shown in figure no 3.1:

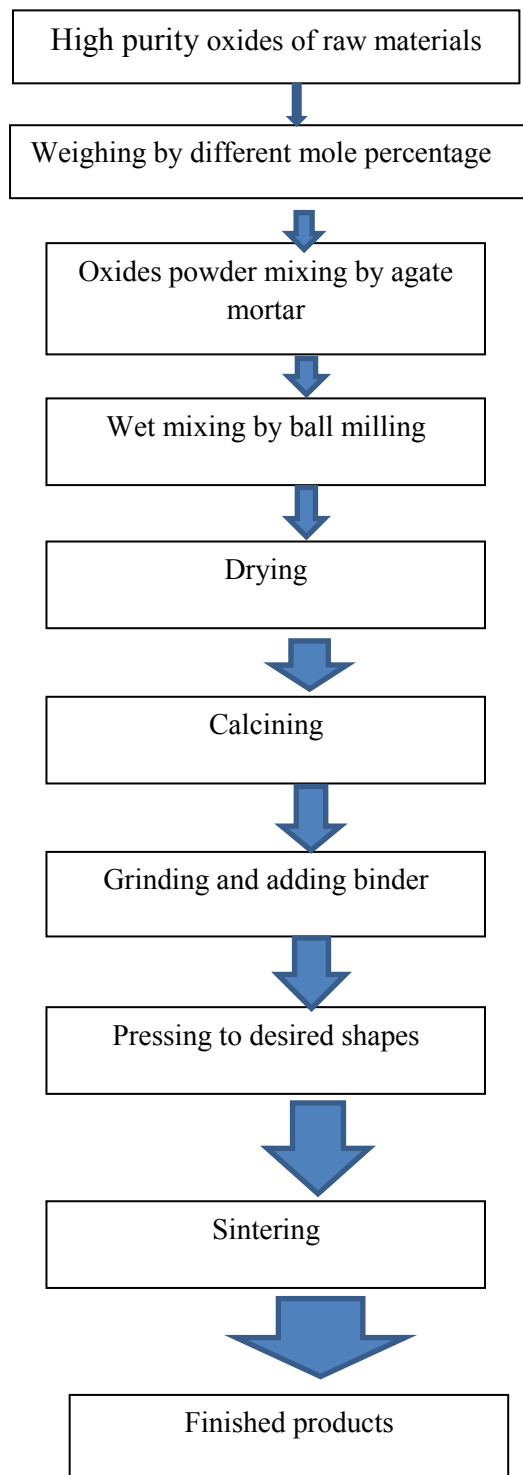


Figure 3.1: Flow chart of solid state reaction technique

As reaction proceeds, the product layer becomes thicker, the length of the diffusion paths of the reactants increases and thus the reaction rate decreases. A simple method

of increasing reaction rates is to crush, mill and repress the product of a first thermal treatment and perform a second sintering.

Next step is the solid-state reaction between the constituents of starting materials at suitable temperature. This process is called firing or calcinations. During calcinations, control over stoichiometry is essential and for it volatile constituents have to be compensated. Calcination causes the constituents to interact by inter-ionic diffusion and resulting in a homogeneous body. Hence it is considered the part of the mixing process. After calcinations powder is compacted to give desired shape, known as green body and it's densified through sintering. A good furnace is used for heat treatment. Pelleting of samples is preferred prior to heating, since it increases the area of contact between the grains. A general discussion on calcinations and sintering is given in the next sections.

3.1.3 Calcination

The solid state synthesis route consists of two steps of thermal treatments, calcination and sintering, which take place below the melting temperatures of the materials. The function of calcination is to remove undesired substances by decomposition and volatilization and to homogenize the material and to alleviate material shrinkage for the subsequent sintering process.

The conventional solid state synthesis route, also known as the ceramic method, refers to a procedure of heating two or more non-volatile solid state materials that can react with one another forming a new compound. The calcination reaction usually takes place at or above the thermal decomposition or transition temperature. This temperature is usually defined as the temperature at which the standard Gibbs free energy for a particular calcination reaction is zero [1].

Typically, the high temperature treatment (500°C-2000°C) is required during the process, which provides the energy condition that enables the ions to leave their original sites and diffuse to different sites. The solid state reaction is quite slow but the reaction can speed up considerably if the temperature is increased. However, due to the decomposition or melting of materials, extremely high temperature is not

avored. In principal, the optimal temperature is defined by a rule of thumb that two-thirds of the melting temperature of the compound always gives best reaction time.

The solid state reactions are always performed in either box furnace or tube furnace, high resistances of metal heating elements inside the furnaces create heat by conversion of electrical energy. In general the tube furnace can with stand higher temperatures (<2300°C) than that of box furnaces. If the reactants are volatile and vulnerable to the oxygen in air, experiments are supposed to be performed in a sealed tube with or without certain gas flowing over the reactant during heating and cooling processes.

3.1.4 Shaping

Calcined powders are ball milled again to give suitable shaping to the powder. Then uniaxial pressing is used to make compacts of small sizes with simple shapes of Calcined powder. It is carried out in a die having movable top. A cavity is formed at the bottom in lower portion. This cavity is filled with free flowing granulated powder and it is stuck with top to die. With the help of the top-punch, pressure in the range of 20-50Mpa is applied using hydraulic press. The powders have been pressed into pellets of thickness 1 mm and diameter 12 mm by using a uniaxial hydraulic press.

Typically cold pressed pellets are 20% to 40% porous. Depending upon requirement of our sample formation, sometimes hot press is required. So that the combined effect of temperature and pressing may cause the particle to fit together better but densification process is usually slow and may require several hours [2].

3.1.5 Sintering

Sintering is defined as the process of obtaining a dense, tough body by heating a compacted powder for a certain time at a temperature high enough to significantly promote diffusion, but clearly lower than the melting point of the main component. The ideal sintering process results in fully dense material by elimination of the porosity.

Sintering is a technique based on atomic diffusion at higher temperature. Thermal expansion caused by the diffusion of atoms diminishes the area between two grains in contact. Atoms in solids are compressed on the surface of their neighboring grains by diffusion of atoms across the boundaries of grains, which increase the density of ceramics. The driving force for sintering is the reduction in surface free energy of the powder. Part of this energy is transferred into interfacial energy (grain boundaries) in the resulting polycrystalline body [3, 4].

Sintering of crystalline solids is dealt by Coble and Burke [5] who found the following empirical relationship regarding rate of grain growth:

$$\bar{d} = kt^n$$

Where \bar{d} is the mean grain diameter, n is about 1/3, t is sintering time and k is a temperature dependent parameter.

Sintering is divided into three stages, Fig. 3.1 [3, 6].

- Stage 1. Contact area between particles increases,
- Stage 2. Porosity changes from open to closed porosity,
- Stage 3. Pore volume decreases; grains grow.

In the initial stage, neighboring particles form a neck by surface diffusion and presumably also at high temperatures by an evaporation-condensation mechanism. Grain growth begins during the intermediate stage of sintering. Since grain boundaries are sinks for vacancies, grain growth tends to decrease the pore elimination rate due to the increase in distance between pores and grain boundaries, and by decreasing the total grain boundary surface area. In the final stage, the grain growth is considerably enhanced and the remaining pores may become isolated.

The interacting variables in sintering process:

Table3.1: variable in sintering

Powder	Composition Average particle size Particle size distribution Particle shape Compaction(green body density)
Impurities	Melting temperature Solubility in product phase Cation valencies
Conditions	Heating rate Temperature Time Cooling rate Oxygen partial pressure

The purposes of sintering process are:

- To bind the particles together so as to impart sufficient strength to the product
- To densify the material by eliminating the pores and
- To homogenize the materials by completing the reactions left unfinished in the calcining step.

3.1.6 Synthesis of the present composition

The polycrystalline samples having compositions $\text{Bi}_{0.9}\text{Gd}_{0.1}\text{Fe}_{1-x}\text{Ti}_x\text{O}_3$ ($x = 0.00-0.20$) were synthesized by using standard solid state reaction technique. The high purity oxides of Bi_2O_3 , Gd_2O_3 , Fe_2O_3 , and TiO_3 powders were carefully weighed in stoichiometric proportion mixed thoroughly with acetone and grounded in an agate mortar until a homogeneous mixture was formed. The compacted mixtures of reagents taken in desired cation ratios were calcined at 800 °C for 1.5 h in a programmable furnace. The calcined powders were grounded again for 2 h to get more homogeneous mixture. The powders were pressed into pellets of thickness 1mm and diameter 12mm

by using a uniaxial hydraulic press and sintered at 825 °C for 5 h at heating rate 10 °C per minute. The sintered pellets and powders were used to measure the required morphological, structural, magnetic, electrical and dielectric properties.

3.2 Characterization technique

The following characterization techniques were used in the present investigation:

- Field Emission Scanning Electron Microscope
- X- ray Diffraction analysis
- X-ray Photoelectron Spectroscopy
- SQUID Magnetometer
- Ferroelectric (P-E) measurement using loop tracer
- Dielectric property measurement using impedance analyser

3.2.1 Field emission scanning electron microscopy

Field emission scanning electron microscopy (FESEM) is an electronic microscope that permits taking high resolution three dimensional appearance images of the surface of samples. Alike TEM microscopes, the difference between a FESEM and a conventional SEM is the way the electrons are produced. In FESEM a field emission electron gun is used, whereas in conventional SEM the electrons are produced thermoionically by heating a W or LaB₆ cathode. FESEM has the advantage of producing much smaller-diameter electron beam ($< 100 \text{ \AA}$), which leads to obtain much higher resolution images (it can be attained spatial resolutions down to 2 nm, between 3 and 6 times better than the resolution of a conventional SEM). In addition, since the electron beam has a smaller diameter, the affected area of the sample is reduced. As a consequence, samples are less electrostatically charged and the need of covering insulating materials with conducting coatings is reduced to a large extent or even eliminated.

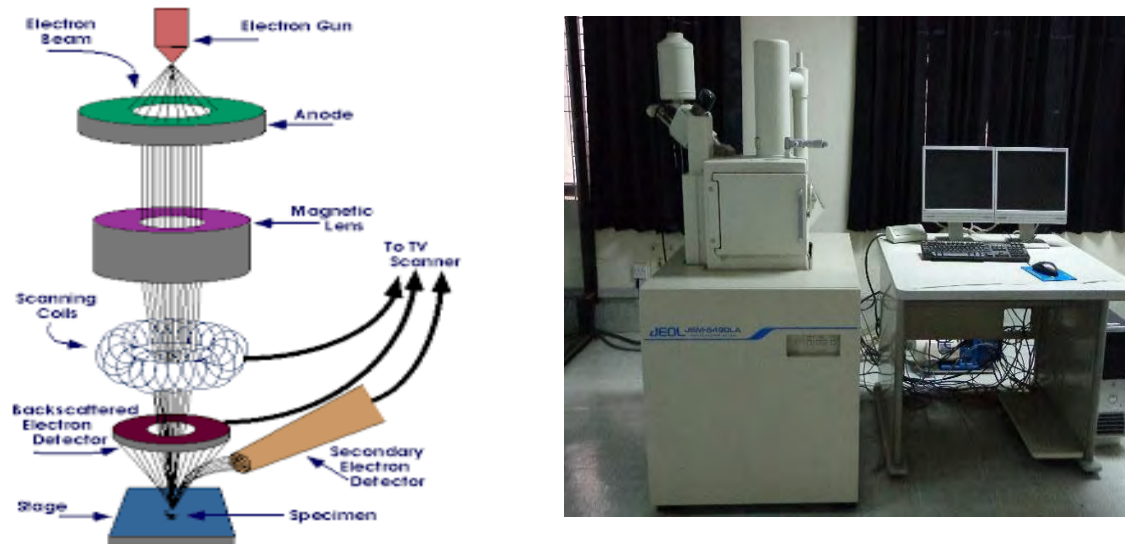


Figure 3.2: (a) Basic scheme of a typical SEM, (b) Jeol JSM 6490LA scanning electron microscope

The SEM process is schematically depicted in Fig. 3.2(a). The electron beam follows a vertical path through the column of the microscope in ultra-high vacuum, where electromagnetic lenses focalizes the beam onto the sample. The scanning coils are used to move the electron beam on the sample. When the electron beam hits the sample, then an interaction between the primary electrons (electron beam) and the matter takes place.

From the sample both electron and photon signals are emitted. Not all the signals are detected and used for information. The signals most commonly used are the so-called secondary electrons, backscattered electrons and X-rays. The secondary electrons are the electrons coming from atoms of the sample that have been ionized by the impact of the primary electrons; the backscattered electrons are primary electrons that have been elastically backscattered; and the production of X-ray is due to electron transitions of the atoms of the sample as they have been excited on being hit by the primary electrons. Both the secondary and the backscattered electrons are used to form the image. They are collected and turned into a signal that is represented by a two-dimensional distribution of intensities and it is viewed as an image by means of a cathode-ray-screen. The X-rays give compositional information and therefore they are not used to characterize the topography.

There are two basic modes for taking the image: by collecting the secondary electrons or by collecting the backscattered electrons. The first ones have the advantage of

giving higher resolution images since they tend to have energies around 50eV and they are therefore ejected from a region very close to the surface. It is necessary to apply a low voltage in order to collect them. The second ones might come from deeper regions as they have higher energy. Because of this they lose surface resolution; however, they give a better contrast as they follow rectilinear trajectories. In this work it has been collected the secondary electrons in order to attain higher spatial resolutions. The microstructure of the surface of pellets was observed using a field emission scanning electron microscope (FESEM, JEOL, JSM 5800) (figure 3.2(b)).

3.2.2 X-ray Diffraction:

X-ray diffraction (XRD) is a rapid analytical technique primarily used for phase identification of a crystalline material and can provide information on unit cell dimensions [7]. The analyzed material is finely ground, homogenized, and average bulk composition is determined.

The atomic planes of a crystal cause an incident beam of X-rays to interfere with one another as they leave the crystal. The phenomenon is called X-ray diffraction. X-ray diffraction is now a common technique for the study of crystal structures and atomic spacing. X-ray diffraction is based on constructive interference of monochromatic X-rays and a crystalline sample.



Figure 3.3: X-ray Diffractometer (XRD).

X-ray diffractometers consist of three basic elements: an X-ray tube, a sample holder, and an X-ray detector. X-rays are generated by a cathode ray tube by heating a filament to produce electrons, accelerating the electrons toward a target by applying a voltage, and bombarding the target material with electrons. When electrons have sufficient energy to dislodge inner shell electrons of the target material, characteristic X-ray spectra are produced. These spectra consist of several components, the most common being K_{α} and K_{β} . Copper is the most common target material for single-crystal diffraction, with Cu- K_{α} radiation = 1.5418Å. Then the diffracted X-rays are filtered to produce monochromatic radiation, collimated to concentrate, and directed toward the sample. The interaction of the incident rays with the sample produces constructive interference (and a diffracted ray) when conditions satisfy Bragg's Law which is given by:

$$2d_{hkl} \sin \theta = n\lambda$$

This law relates the wavelength (λ) of electromagnetic radiation to the diffraction angle (θ) and the lattice spacing (d_{hkl}) between two crystal plane in a crystalline sample. These diffracted X-rays are then detected, processed and counted. By scanning the sample through a range of 2θ angles, all possible diffraction directions of the lattice should be attained due to the random orientation of the powdered material.

The intensity of diffracted X-rays is continuously recorded as the sample and detector rotate through their respective angles. A peak in intensity occurs when the mineral contains lattice planes with d_{hkl} spacings appropriate to diffract X-rays at that value of θ . Once all d_{hkl} -spacings have been determined they can be compared with standard data, available from the International Centre for Diffraction Data as the Powder Diffraction File (PDF), which facilitates to identify any impurity phases appeared as extra peaks.

The average size of particles of crystals in the form of powder can be determined from XRD patterns using Scherrer equation which is given by:

$$\tau = \frac{K\lambda}{\beta \cos \theta}$$

Where τ is the mean size of the ordered (crystalline) domains, which may be smaller or equal to the grain size; K is a dimensionless shape factor, with a value close to

unity. The shape factor has a typical value of about 0.9, but varies with the actual shape of the crystallite; λ is the X-ray wavelength; β is the line broadening at half the maximum intensity (FWHM). θ is the Bragg angle. The crystal structure of the samples (sintered powder) was determined from x-ray diffraction (XRD) data. XRD patterns were collected at RT using a diffractometer (Rigaku Ultimate VII) with Cu-K α ($\lambda = 1.5418 \text{ \AA}$) radiation.

3.2.3 X-ray Photoelectron Spectroscopy:

X-ray photoelectron spectroscopy (XPS) is a surface-sensitive quantitative spectroscopic technique that identifies the composition and valence state of the elements in the samples. It is used to measure the elemental composition at the parts per thousand range, empirical formula, chemical state and electronic state of the elements that exist within a material.

X-ray photoelectron spectroscopy uses soft x-rays (with a photon energy of 200-2000 eV) to examine core-levels. The energy of a photon of all types of electromagnetic radiation is given by the Einstein relation:

$$E = h\nu$$

Where, h - Planck constant ($6.62 \times 10^{-34} \text{ J s}$), ν - frequency (Hz) of the radiation.

In XPS the photon is absorbed by an atom in a molecule or solid, leading to ionization and the emission of a core (inner shell) electron. The kinetic energy distribution of the emitted photoelectrons (i.e. the number of emitted photoelectrons as a function of their kinetic energy) can be measured using any appropriate electron energy analyzer and a photoelectron spectrum can thus be recorded. An electron at a given electronic level is characterized by its binding energy (E_B) which can be determined by using the energy conservation law

$$h\nu = E_B + E_K + \phi_o$$

where, $h\nu$ is known as the incident photon energy, E_B represents the binding energy and ϕ_o is the work function of the sample, and E_K is kinetic energy possessed by emitting electron.

The XPS spectrum shows the peaks that are directly related to the electronic structure of atoms. The peaks are indexed like the electronic levels from where the photoelectrons are coming. Since each element has a unique binding energy, the XPS spectrum can be used to give quantitative information on the elemental composition of a sample and the chemical state. Because each element has unique set of binding energies, XPS can be used to identify and determine the concentration of the elements in the surface. Variation in the elemental binding energies (the chemical shifts) arise from differences in the chemical potential and polarizability of compounds.

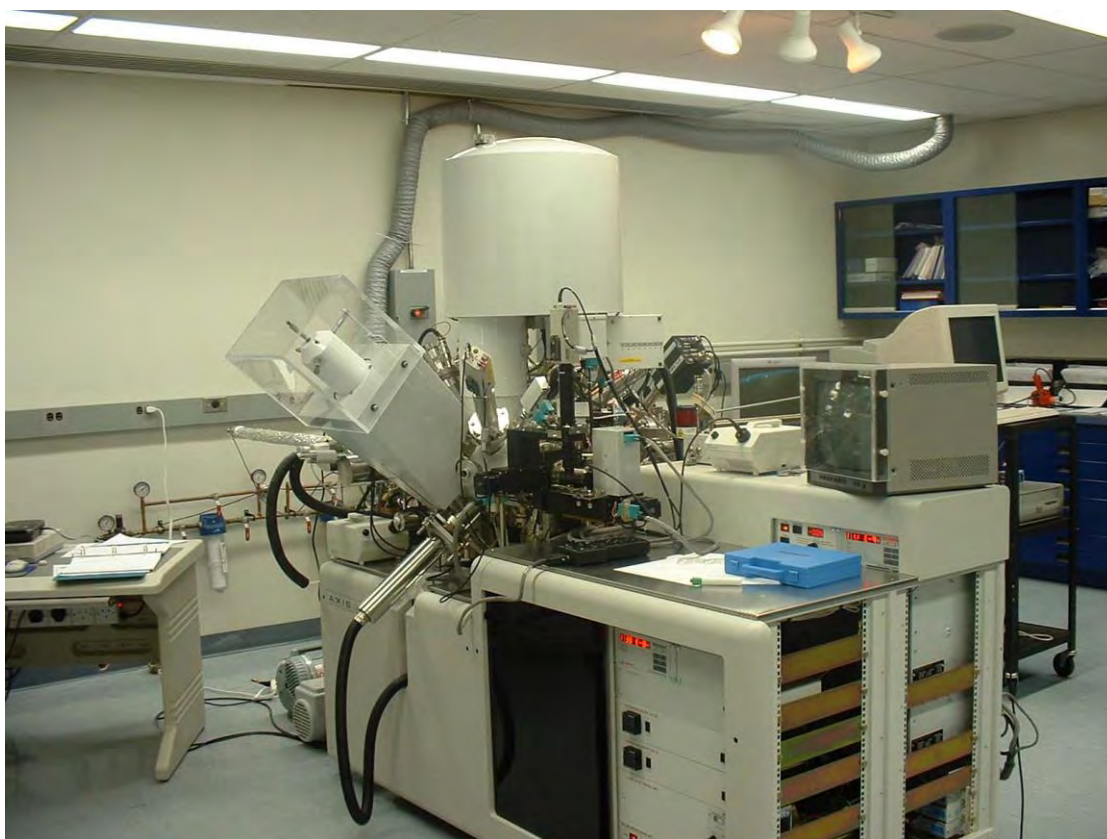


Figure 3.4: XPS Spectrometer.

These chemical shifts can be used to identify the chemical state of the material being analyzed. In our studies, X-ray photoelectron spectroscopy (XPS, ULVAC-PHI Inc., Model 1600) analysis was carried out with a $Mg-K_{\alpha}$ radiation source.

3.2.4 The SQUID Magnetometer

The influence of magnetic flux on a Josephson junction may be employed for measuring magnetic fields or magnetizations. The basic element of a Superconducting Quantum Interference Device (SQUID) magnetometer is a ring of superconducting metal containing critical current of an array of two Josephson junctions is periodic in field units of one or two weak links. The name quantum interference is derived from the fact that the due to interference effects of the electron-pair wave functions. A dc SQUID is built with two Josephson junctions and a dc current is applied to this device. The effect of a radio frequency (RF) field on the critical current is used to detect quasi-static flux variations. The RF SQUID is a simple ring with only one Josephson junction. Variation of the flux in the ring results in a change of impedance [8]. This change in impedance results in detuning of a weakly coupled resonator circuit driven by an RF current source.

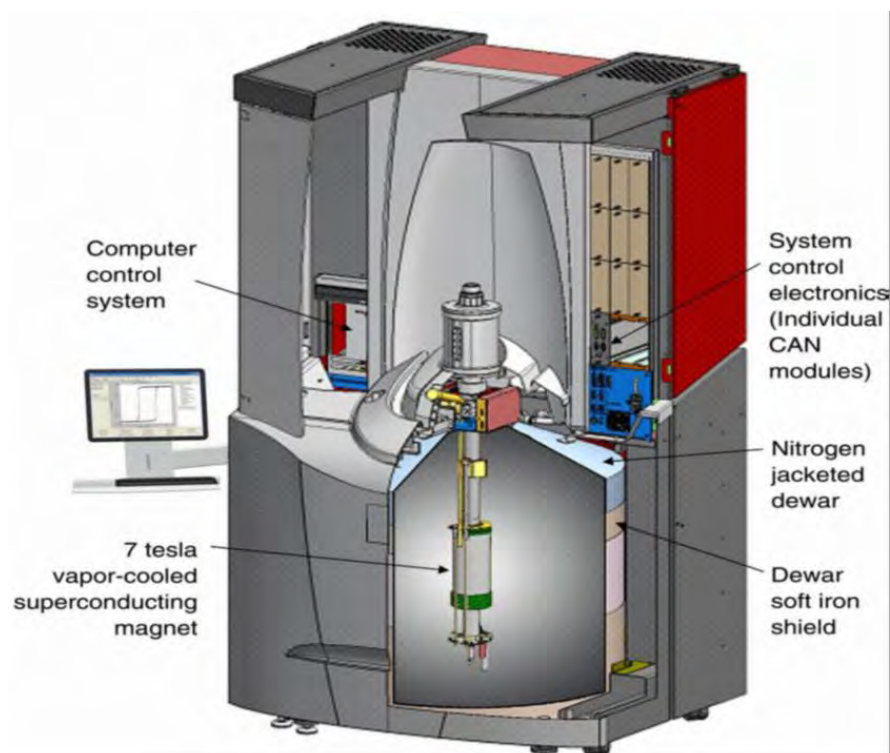


Figure 3.5: Cutway view of the MPMS SQUID magnetometer

When magnetic flux is applied to the ring, an induced current flows through the superconducting ring. In turn, this current induces a variation of the RF voltage across

the circuit. With a lock-in amplifier this variation is detected. A feedback arrangement is used to minimize the current flowing in the ring, the size of the feedback current being a measure of the applied magnetic flux. The method is capable of measuring magnetic moments in the range 10^{-10} - 10^3 Am² with an accuracy of 1%. Custom-designed dc SQUIDs can have a few orders of magnitude higher.

The traditional superconducting materials for SQUIDs are pure niobium or a lead alloy with 10% gold or indium, as pure lead is unstable when its temperature is repeatedly changed. To maintain superconductivity, the entire device needs to operate within a few degrees of absolute zero, cooled with liquid helium.

High-temperature SQUID sensors are made of high-temperature superconductors, particularly YBCO, and are cooled by liquid nitrogen which is cheaper and more easily handled than liquid helium. They are less sensitive than conventional low temperature SQUIDs but good enough for many applications.

Magnetoencephalography (MEG), for example, uses measurements from an array of SQUIDs to make inferences about neural activity inside brains. Another area where SQUIDs are used is magnetogastrography, which is concerned with recording the weak magnetic fields of the stomach. A novel application of SQUIDs is the magnetic marker monitoring method, which is used to trace the path of orally applied drugs. In the clinical environment SQUIDs are used in cardiology for magnetic field imaging (MFI), which detects the magnetic field of the heart for diagnosis and risk stratification. Probably the most common commercial use of SQUIDs is in magnetic property measurement systems (MPMS). SQUIDs are being used as detectors to perform magnetic resonance imaging (MRI). While high-field MRI uses precession fields of one to several teslas, SQUID-detected MRI uses measurement fields that lie in the microtesla range. The use of SQUIDs in oil prospecting, mineral exploration, earthquake prediction and geothermal energy surveying is becoming more widespread as superconductor technology develops.

A cutaway view of the Quantum Design MPMS XL7 SQUID 45 magnetometer used for the measurement of magnetization of materials is shown in figure 3.5.

3.2.5 Ferroelectric measurements

A ferroelectric measurement (automatic P-E Loop tracer, MARINE INDIA) system (Figure 3.6) was carried out for electrical characterization of synthesized materials. The system measured the hysteresis loops and leakage current for these materials. Measurements were performed at line frequency of 50 Hz.

The complete measurement system consists of the following:

- PE main unit
- Sample holder
- Furnace with temperature controller
- Desktop PC



Figure 3.6: Automatic P-E Loop tracer at Nanotechnology Research Laboratory, BUET.

The following studies can be done with the apparatus

- 1) Determination of spontaneous polarization (P_s)
- 2) Determination of Remnant polarization (P_r)
- 3) Determination of coercive field (E_c)
- 4) Determination of Curie temperature (T_c)

3.2.5.1 Basic theory of operation

The basic PE test system is based on Sawyer Tower (S-T) circuit [3] (Figure 3.7).

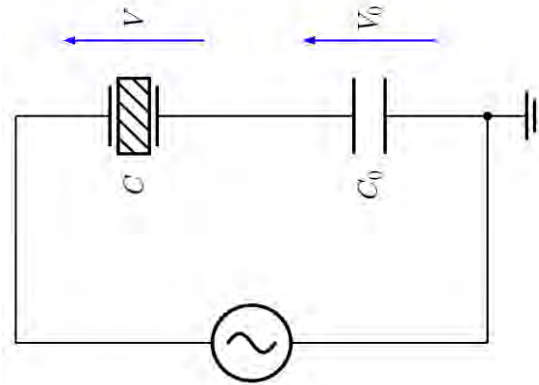


Figure 3.7: Sawyer Tower (S-T) circuit

The circuit consists of two capacitors, one due to sample (C) and other one is a linear known valued internal capacitor (C₀) they are connected in series. The principle is simple when two capacitors are connected in series and AC voltage is applied on both in series, the charge on both will be same. In order to get complete saturation the internal capacitance must be bigger than of the sample capacitance.

A high voltage oscillator produces an adjustable sinusoidal output from 0 to 350V (r.m.s.). The frequency is variable in a small range around 30Hz. The oscillator output is applied to the dielectric sample kept in a temperature-controlled oven. Due to the large amplitude of the alternating source, the dielectric material exhibits a hysteresis loop similar to that observed in a ferromagnetic material under the influence of an alternating magnetic field. The loop can be displayed on a CRO with the help of a circuit, which basically monitors the charge flow through the sample and plots it against the voltage applied on it.

3.2.6: Dielectric Properties Measurement

A dielectric is an electrical insulator that may be polarized by the action of an applied electric field. When a dielectric material is placed in an electric field, electric charge do not flow through the material, as in a conductor, but only slightly shift from their average equilibrium positions causing dielectric polarization: positive charges are displaced along the field and negative charges shift in the opposite direction. Dielectric typically means materials with a high polarizability. The latter is expressed by a number called the relative permittivity (also known in older texts as dielectric constant). A common example of a dielectric is the electrically insulating material between the metallic plates of a capacitor. The polarization of the dielectric by the applied electric field increases the capacitor's surface charge for the given electric field strength.

The dielectric properties were measured using Wayne Kerr impedance analyzer 6500 B series. Measurements of dielectric properties normally involve the measurements of the change in capacitance and loss of a capacitor in presence of the dielectric materials. The behavior of a capacitance can now be described as follows. Here an ideal loss less air capacitor of capacitance C_0 . On insertion of a dielectric material in a space the capacitance will be changed. The dielectric constant (ϵ') and electrical properties measurements on disk-spaced specimens will be carried out at room temperature on all the samples in the high frequency range.

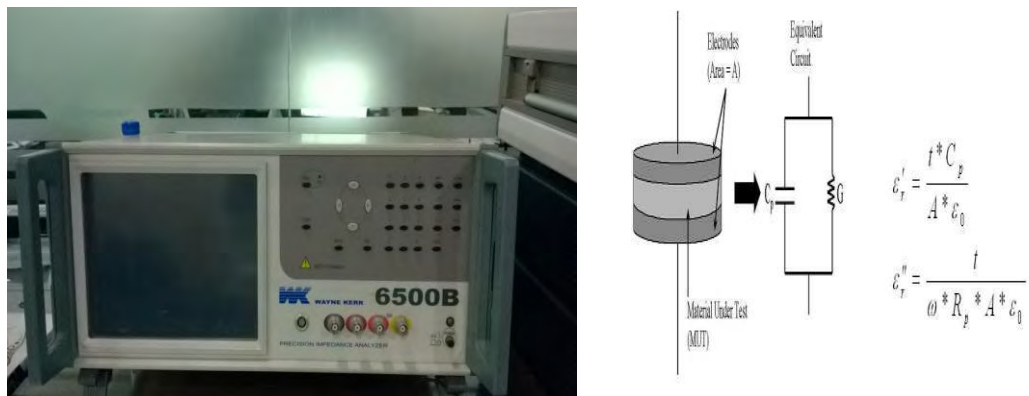


Figure 3.8: WAYNE KERR impedance analyzer 6500B series

The dielectric constant ϵ' will be calculated using the following relations, $\epsilon' = C/C_0$ and $\epsilon'' = \epsilon' \tan \delta$ where, C is the capacitance of the sample and $C_0 = \epsilon_0 A/d$, is derived geometrically. Here C_0 is the capacitance of the capacitor without the dielectric materials, d is the thickness of the capacitor and $A (= \pi r^2)$ is the area of cross section of the disk space sample. For the measurement of dielectric properties the samples will be painted on either side with silver paste to ensure good electric contacts.

References:

- [1] Goldman, A., Handbook of Modern Ferromagnetic Materials, Kulwer Acad. Pub, Boston, U.S.A., 1999.
- [2] West, A. R., "Solid state chemistry and its applications", John Willey Sons, 1887.
- [3] Valenzuela, R., Magnetic Ceramics, Cambridge University Press, Cambridge, 1994.
- [4] Kingery, W. D., Bowen, H. K. and Uhlman, D. R., "Introduction to Ceramics", 2nd edition, Wiley Interscience, New York, 476, 1976.
- [5] Coble, R. L. and Burke, J. E., "4th Int. Symp. On the Reactivity of Solid", Amsterdam, 38-51, 1960.
- [6] McColm, I. J. and Clark, N. J., "Forming, Shaping and Working of high Performance Ceramics", Blackie, Glasgow, 1-338, 1988.
- [7] Basith, M. A., Manjura Hoque, Sk., Shahparan, Md., Hakim, M.A., Huq, M., "Temperature features of magnetoresistance of layered manganites $\text{La}_2\text{Sm}_{0.4}\text{Sr}_{0.6}\text{Mn}_2\text{O}_7$ " Physica B. 126-129, 395, 2007.
- [8] Josephson, B.D., "The discovery of tunneling super currents", Rev. Mod. Phys. 46,251, 1974.

Chapter 4

Results and Discussion

The nominal compositions of $\text{Bi}_{0.9}\text{Gd}_{0.1}\text{Fe}_{1-x}\text{Ti}_x\text{O}_3$ ($x = 0.00\text{--}0.20$) ceramics were synthesized by conventional solid state reaction technique and their temperature dependent magnetic properties were investigated in details. The outcome of this investigation is presented in this chapter.

4.1 Morphological Studies

To investigate the microstructure of the surface of the pellets, FESEM imaging was carried out for all of the samples. Figure 4.1(a) and (b) demonstrates the surface morphology of the pellet of undoped BiFeO_3 sample and the 10% Gd doped $\text{Bi}_{0.9}\text{Gd}_{0.1}\text{FeO}_3$ sample respectively. Notably, in the nominal compositions of $\text{Bi}_{0.9}\text{Gd}_{0.1}\text{Fe}_{1-x}\text{Ti}_x\text{O}_3$ ceramics, it is expected that titanium is in its tetravalent state and the non-magnetic Ti^{4+} substitutes Fe^{3+} . This is in fact not very simple because in order to accommodate a charge balance some Fe must be present as Fe^{2+} or there must be present some type of non-stoichiometry. Figure 4.1(c) shows the microstructure of the Ti doped $\text{Bi}_{0.9}\text{Gd}_{0.1}\text{Fe}_{0.9}\text{Ti}_{0.1}\text{O}_3$ ceramic with $x = 0.10$ as a representative of the $x = 0.20$ ceramics. Insets of Figs. 4.1(a), 4.1(b) and 4.1(c) show the histograms of the grain size distributions of the respective micrographs. It is clear from Figs. 4.1(b) and 4.1(c) and their respective histograms that the average grain size is reduced from ~ 1.5 μm to ~ 200 nm with increasing Ti concentration. Previous studies demonstrated that undoped BiFeO_3 had a dense microstructure with an average size of ~ 5 to ~ 15 μm [1,2]. In our investigation, we have also observed that the average grain size of pure BiFeO_3 is around ~ 3.5 μm .

Therefore, unlike the non-modified BiFeO_3 sample, the average grain size of the Ti undoped, i.e., 10% Gd doped $\text{Bi}_{0.9}\text{Gd}_{0.1}\text{FeO}_3$ sample is ~ 1.5 μm which is well consistent with previous investigation [3]. The substitution of the Ti content to 10% ($x = 0.10$) reduced the average grain size to ~ 200 nm as well as made the distribution

of the grains homogeneous (Fig. 4.1(c)). Notably, increase of the Ti content from $x = 0.10$ to $x = 0.20$ does not reduce the average grain size from ~ 200 nm. Due to the substitution of Ti, the average grain size was reduced and the peak in the XRD pattern of the Ti substituted sample was widened as shown in Fig.4.2. Previous investigation suggested that the grain growth depends upon the concentration of oxygen vacancies [4] and diffusion rate of the ions. Large number of oxygen vacancies are generate in pure BiFeO_3 due to highly volatile nature of Bi.

An increment of the Ti doping concentration in $\text{Bi}_{0.9}\text{Gd}_{0.1}\text{Fe}_{1-x}\text{Ti}_x\text{O}_3$ decreased the average grain size significantly due to the fact that Ti possesses a higher valence than Fe and suppresses the formation of oxygen vacancies. Therefore, the significant reduction of the average grain size in Gd and Ti co-doped BiFeO_3 samples could be interpreted by the suppression of the formation of oxygen vacancies because of the requirements of the charge compensation. The decreased oxygen vacancies lead to a lower grain growth rate which is actually a consequence of slower oxygen ion motion [5].

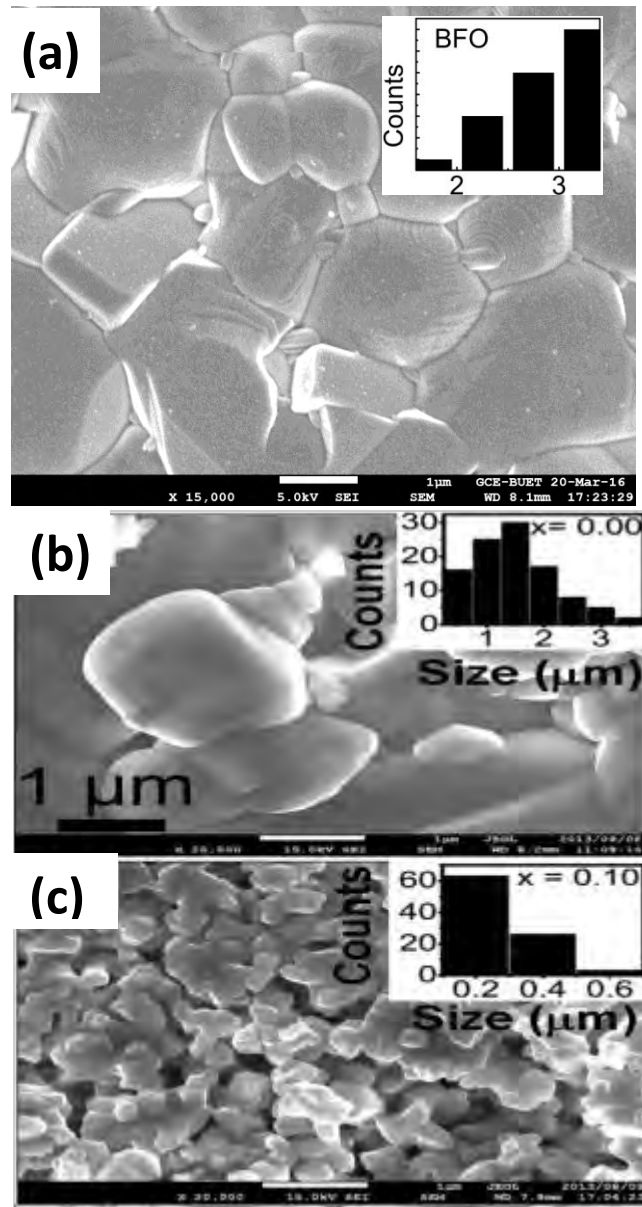


Figure 4.1: FESEM micrograph of $\text{Bi}_{0.9}\text{Gd}_{0.1}\text{Fe}_{1-x}\text{Ti}_x\text{O}_3$ ceramics: (a) undoped BiFeO_3 (b) $x = 0.00$, (c) $x = 0.10$. Inset: respective histograms of images (a), (b) and (c).

4.2 Structural Characterization

The XRD patterns of undoped BFO, Gd doped BFO and Gd-Ti co-doped BFO ceramics, sintered at 825 °C and their optimum density indicate the formation of polycrystalline structure. The formation of secondary phases during the solid state synthesis of bulk undoped BFO and cations substituted BFO was almost unavoidable in a number of previous investigations [6–9]. The final distribution of these secondary phases [10] was influenced greatly by the specific reaction path way, however, the latent mechanism behind this formation is still unknown.

In a previous investigation [11], the structural analysis and phase identification of

these multiferroic ceramics was not performed using Rietveld refinement. This time around, Rietveld refinement was carried out using the FULLPROF package [12] to analyze the crystal structure as well as to quantify the crystallographic phases of these compounds. The Rietveld refined XRD patterns of the four samples under scrutiny are depicted in Fig. 4.2. The structural parameters obtained with the help of the refinement as well as phases present are (in wt%) obtained from XRD studies of BFO, Gd doped BFO and Gd-Ti co-doped BFO are listed in supplemental Table 4.1. In each of the sample, we found that the major phases namely, BFO, Gd doped BFO and Gd-Ti co-doped BFO are of rhombohedral $R3c$ type crystal structure. In BFO, besides the major phase, the impurity phase $\text{Bi}_2\text{Fe}_4\text{O}_9$ is present as well (3.91%) as shown in Fig. 4.2. This undesired phase has orthorhombic structure ($pbam$) with lattice parameters, $a = 8.3502\text{\AA}$, $b = 7.8489\text{\AA}$ and $c = 5.9275\text{\AA}$. Next, for the Gd doped BFO, again a significant amount of impurity phase concentration is observed which is $\text{Bi}_2\text{Fe}_4\text{O}_9$ (7.51%). Interestingly, when we performed Gd and Ti co-substitution, this unintended phase is suppressed significantly as the wt% of $\text{Bi}_2\text{Fe}_4\text{O}_9$ reduces to 1.38% in 10% Gd and Ti co-doped $\text{Bi}_{0.9}\text{Gd}_{0.1}\text{Fe}_{0.9}\text{Ti}_{0.1}\text{O}_3$. Further more, when the Ti doping is increased to 20% in $\text{Bi}_{0.9}\text{Gd}_{0.1}\text{Fe}_{0.8}\text{Ti}_{0.2}\text{O}_3$, the amount of undesired phases increases to 4.2% which substantiates our idea of the 10% Gd and Ti co-doped BFO, $\text{Bi}_{0.9}\text{Gd}_{0.1}\text{Fe}_{0.9}\text{Ti}_{0.1}\text{O}_3$ being the most suitable composition to perform extensive investigation of its multiferroic properties. This is also illustrated in Fig. 4.2 from the difference between the observed and calculated XRD patterns of the samples obtained from Rietveld refinement. We note that highest match occurs between these two patterns for 10% Gd and Ti co-doped $\text{Bi}_{0.9}\text{Gd}_{0.1}\text{Fe}_{0.9}\text{Ti}_{0.1}\text{O}_3$ which indicates very negligible impurities present in this particular composition. The atomic coordinates of the samples have also been listed in the Table 4.1.

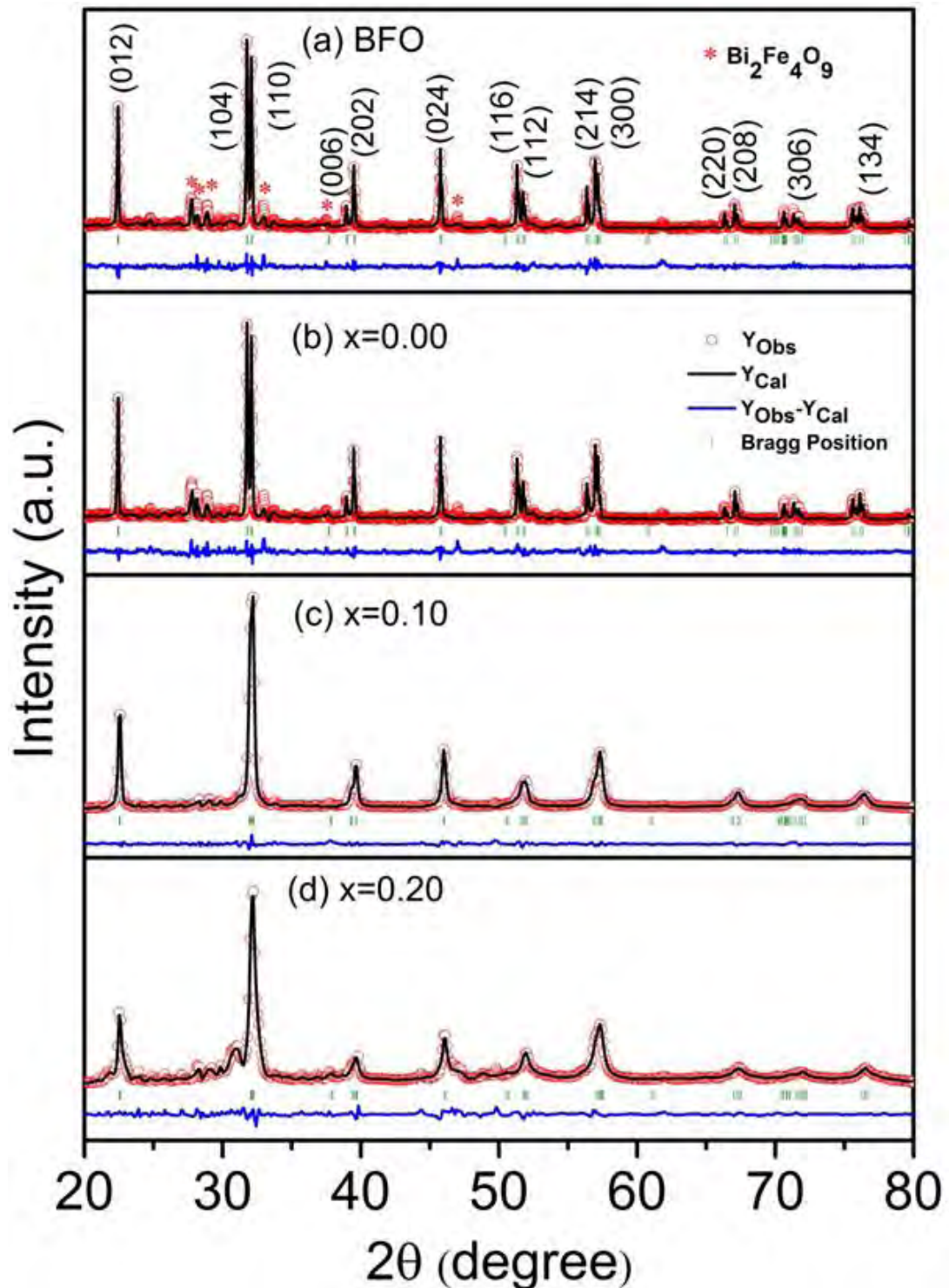


Figure 4.2: Rietveld refined XRD patterns of (a) undoped BiFeO_3 , (b) Gd doped $\text{Bi}_{0.9}\text{Gd}_{0.1}\text{Fe}_{1-x}\text{Ti}_x\text{O}_3$ ($x = 0.00$), (c) Gd-Ti co-doped $\text{Bi}_{0.9}\text{Gd}_{0.1}\text{Fe}_{1-x}\text{Ti}_x\text{O}_3$ ($x = 0.10$) and (d) Gd-Ti co-doped $\text{Bi}_{0.9}\text{Gd}_{0.1}\text{Fe}_{1-x}\text{Ti}_x\text{O}_3$ ($x = 0.20$) ceramics carried out at RT. Here the observed data are represented by red circles (Y_{Obs}), the black solid line represents the calculated pattern (Y_{Cal}) and the blue bottom curve is their difference ($Y_{\text{Obs}}-Y_{\text{Cal}}$), green bars correspond to Bragg positions of the major phase of the corresponding samples.

Table 4.1: Rietveld refined structural parameters and amount of phases present (in wt%) obtained from XRD studies of BFO, Gd doped BFO and Gd-Ti co-doped $\text{Bi}_{0.9}\text{Gd}_{0.1}\text{Fe}_{1-x}\text{Ti}_x\text{O}_3$ ($x = 0.10-0.20$).

Sample	Crystal Structure	Lattice Parameters	R Factor (%)
BiFeO_3	BFO (Rhombohedral) (R3c) (77.09%)	$a = b = 5.5775 \text{ \AA}$, $c = 13.8661 \text{ \AA}$ $V = 373.564 \text{ \AA}^3$	$\chi^2 = 14.3$
	$\text{Bi}_2\text{Fe}_4\text{O}_9$ (Orthorhombic) (pbam) (3.91%)	$a = 8.3502 \text{ \AA}$, $b = 7.8489 \text{ \AA}$ $c = 5.9275 \text{ \AA}$, $V = 388.485 \text{ \AA}^3$	$\chi^2 = 14.3$
	BFO (Orthorhombic) (pnma) (18.75%)	$a = 3.6970 \text{ \AA}$, $b = 3.9195 \text{ \AA}$ $c = 6.5145 \text{ \AA}$, $V = 94.397 \text{ \AA}^3$	$\chi^2 = 14.3$
$\text{Bi}_{0.9}\text{Gd}_{0.1}\text{FeO}_3$	Gd doped BFO (Rhombohedral) (R3c) (88.33%)	$a = b = 5.5772 \text{ \AA}$, $c = 13.8655 \text{ \AA}$ $V = 373.514 \text{ \AA}^3$	$\chi^2 = 15.1$
	$\text{Bi}_2\text{Fe}_4\text{O}_9$ (Orthorhombic) (pbam) (7.51%)	$a = 8.3429 \text{ \AA}$, $b = 7.8151 \text{ \AA}$ $c = 5.9403 \text{ \AA}$, $V = 387.315 \text{ \AA}^3$	$\chi^2 = 15.1$
	BFO (Orthorhombic) (pnma) (3.83%)	$a = 3.6665 \text{ \AA}$, $b = 3.9159 \text{ \AA}$ $c = 6.458347 \text{ \AA}$, $V = 92.728 \text{ \AA}^3$	$\chi^2 = 15.1$
$\text{Bi}_{0.9}\text{Gd}_{0.1}\text{Fe}_{0.9}\text{Ti}_{0.1}\text{O}_3$	Gd-Ti co-doped BFO ($x=0.1$) (Rhombohedral) (R3c) (97.16%)	$a = b = 5.5631 \text{ \AA}$, $c = 13.7541 \text{ \AA}$ $V = 368.632 \text{ \AA}^3$	$\chi^2 = 7.279$
	Gd-Ti co-doped BFO ($x=0.1$) (Orthorhombic) (pn21a) (1.38%)	$a = 5.1989 \text{ \AA}$, $b = 5.6205 \text{ \AA}$ $c = 4.9757 \text{ \AA}$, $V = 145.395 \text{ \AA}^3$	$\chi^2 = 7.279$
	$\text{Bi}_2\text{Fe}_4\text{O}_9$ (Orthorhombic) (pbam) (1.38%)	$a = 8.2986 \text{ \AA}$, $b = 7.8021 \text{ \AA}$ $c = 5.9263 \text{ \AA}$, $V = 383.707 \text{ \AA}^3$	$\chi^2 = 7.279$
$\text{Bi}_{0.9}\text{Gd}_{0.1}\text{Fe}_{0.8}\text{Ti}_{0.2}\text{O}_3$	Gd-Ti co-doped BFO ($x=0.2$) (Rhombohedral) (R3c) (88.25%)	$a = b = 5.5582 \text{ \AA}$, $c = 13.7105 \text{ \AA}$ $V = 366.822$	$\chi^2 = 12.15$
	Gd-Ti co-doped BFO ($x=0.2$) (Orthorhombic) (pn21a) (7.54%)	$a = 5.1195 \text{ \AA}$, $b = 5.6373 \text{ \AA}$ $c = 5.0653 \text{ \AA}$, $V = 146.184$	$\chi^2 = 12.15$
	$\text{Bi}_2\text{Fe}_4\text{O}_9$ (Orthorhombic) (pbam) (2.56%)	$a = 8.2995 \text{ \AA}$, $b = 7.7482 \text{ \AA}$ $c = 5.9225 \text{ \AA}$, $V = 380.849$	$\chi^2 = 12.15$
	Fe_2O_3 (Rhombohedral) (R3c) (1.64%)	$a = b = 4.9435 \text{ \AA}$, $c = 13.9028 \text{ \AA}$ $V = 294.245$	$\chi^2 = 12.15$

The X-ray photoelectron spectroscopy (XPS) of the above mentioned samples was performed. To investigate the oxygen vacancy related effects, in Fig. 4.3 the O 1s core XPS spectra of the corresponding samples are shown. The plots display an asymmetric peak very close to 529 eV along with an additional peak at slightly higher binding energy (HBE). The asymmetric curves of the samples have been Gaussian fitted by two symmetrical peaks. The lower binding energy (LBE) peak around 529.3 eV corresponds to the O 1s core spectrum, while the HBE peak is related to the oxygen vacancy in the samples [13]. The area ratios of the two peaks (HBE/ LBE) for the samples BFO, Gd doped BFO, $\text{Bi}_{0.9}\text{Gd}_{0.1}\text{Fe}_{0.9}\text{Ti}_{0.1}\text{O}_3$ and $\text{Bi}_{0.9}\text{Gd}_{0.1}\text{Fe}_{0.8}\text{Ti}_{0.2}\text{O}_3$ are 1.59, 3.46, 1.21 and 1.07 respectively. So, clearly the ratio decreases with Gd-Ti co-substitution as compared to BFO and Gd doped BFO indicating reduction in oxygen

vacancies. The effect of this reduced vacancy is further explored in section C where we investigate the leakage current density of the samples.

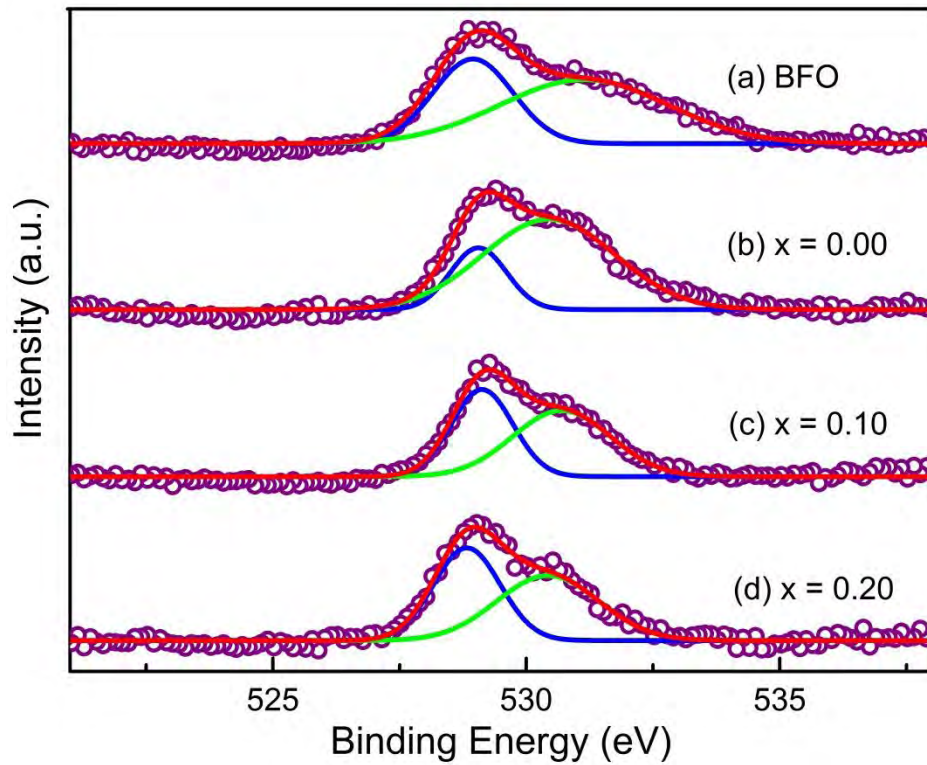


Figure 4.3: The O 1s core XPS spectrum of (a) undoped BiFeO_3 , (b) Gd doped $\text{Bi}_{0.9}\text{Gd}_{0.1}\text{Fe}_{1-x}\text{Ti}_x\text{O}_3$ ($x = 0.00$), (c) Gd-Ti co-doped $\text{Bi}_{0.9}\text{Gd}_{0.1}\text{Fe}_{1-x}\text{Ti}_x\text{O}_3$ ($x = 0.10$) and (d) Gd-Ti co-doped $\text{Bi}_{0.9}\text{Gd}_{0.1}\text{Fe}_{1-x}\text{Ti}_x\text{O}_3$ ($x = 0.20$) samples.

4.3 Magnetic characterization

Room Temperature Magnetic Characterization carried out by SQUID magnetometer:

For magnetic characterization, the $M - H$ hysteresis loops of undoped, Gd doped and Gd-Ti co-doped BFO ceramics were carried out at RT with an applied magnetic field of up to ± 50 kOe. The undoped BFO sample possesses a very narrow hysteresis loop with a very small but non-zero remanent magnetization (0.001 emu/g) and a coercive field of ~ 132 Oe at RT. This is due to antiferromagnetic (AFM) nature of undoped BFO which possesses no spontaneous magnetization [14] but has residual magnetic moment for a canted spin structure. The Gd doped $\text{Bi}_{0.9}\text{Gd}_{0.1}\text{FeO}_3$

and Gd-Ti co-doped $\text{Bi}_{0.9}\text{Gd}_{0.1}\text{Fe}_{1-x}\text{Ti}_x\text{O}_3$ ($x = 0.10-0.20$) samples also exhibit unsaturated hysteresis loops but with large remanent magnetizations and coercive fields. Due to the substitution of Gd and co-substitution of Gd and Ti in place of Bi and Fe in BiFeO_3 , respectively, the unsaturated magnetization behavior of the samples remains unaltered, however, the center of the hysteresis loops was many folds wider compared to that of undoped BFO. For obtaining quantitative measures of the coercive fields (H_c) and remanent magnetization (M_r) from the hysteresis loops, formulas used were: $H_c = (H_{c1} - H_{c2})/2$, where H_{c1} and H_{c2} are the left and right coercive fields [11, 15] and $M_r = |(M_{r1} - M_{r2})|/2$ where M_{r1} and M_{r2} are the magnetization with positive and negative points of intersection with $H = 0$, respectively [16]. Calculated values of M_r and H_c for undoped, Gd doped and Gd-Ti co-doped BFO bulk materials are inserted in Table 4.2.

Both the coercive fields and remanent magnetizations are higher for 10% Gd and Ti co-doped $\text{Bi}_{0.9}\text{Gd}_{0.1}\text{Fe}_{1-x}\text{Ti}_x\text{O}_3$ ($x = 0.10$) sample than those for other materials. However, when we further increased the Ti concentration to 20% in $\text{Bi}_{0.9}\text{Gd}_{0.1}\text{Fe}_{1-x}\text{Ti}_x\text{O}_3$ ($x = 0.20$), H_c and M_r got reduced despite their net values being still higher compared to that of Gd doped $\text{Bi}_{0.9}\text{Gd}_{0.1}\text{Fe}_{0.9}\text{Ti}_{0.1}\text{O}_3$ sample. The larger values of H_c and M_r in sample $x = 0.10$ are associated with the microstructure of the composition, i.e. with its homogeneous reduced grain size than that of the other materials as reported in a previous investigation [11]. Zhai et al. attributed increase in coercive field with the co-substitution of La and Nb in BiFeO_3 [17]. Similar reasoning was reported for P_r and Z_r co-substituted BiFeO_3 compounds in Ref. [18]. The unsaturated magnetization behavior at higher fields clearly indicates the dominating AFM nature of these ceramics. A large coercive field, of up to 6399 Oe is observed for 10% Gd and Ti codoped $\text{Bi}_{0.9}\text{Gd}_{0.1}\text{Fe}_{0.9}\text{Ti}_{0.1}\text{O}_3$ sample owing to the strong magnetocrystalline anisotropy of the compound despite having a FM component.

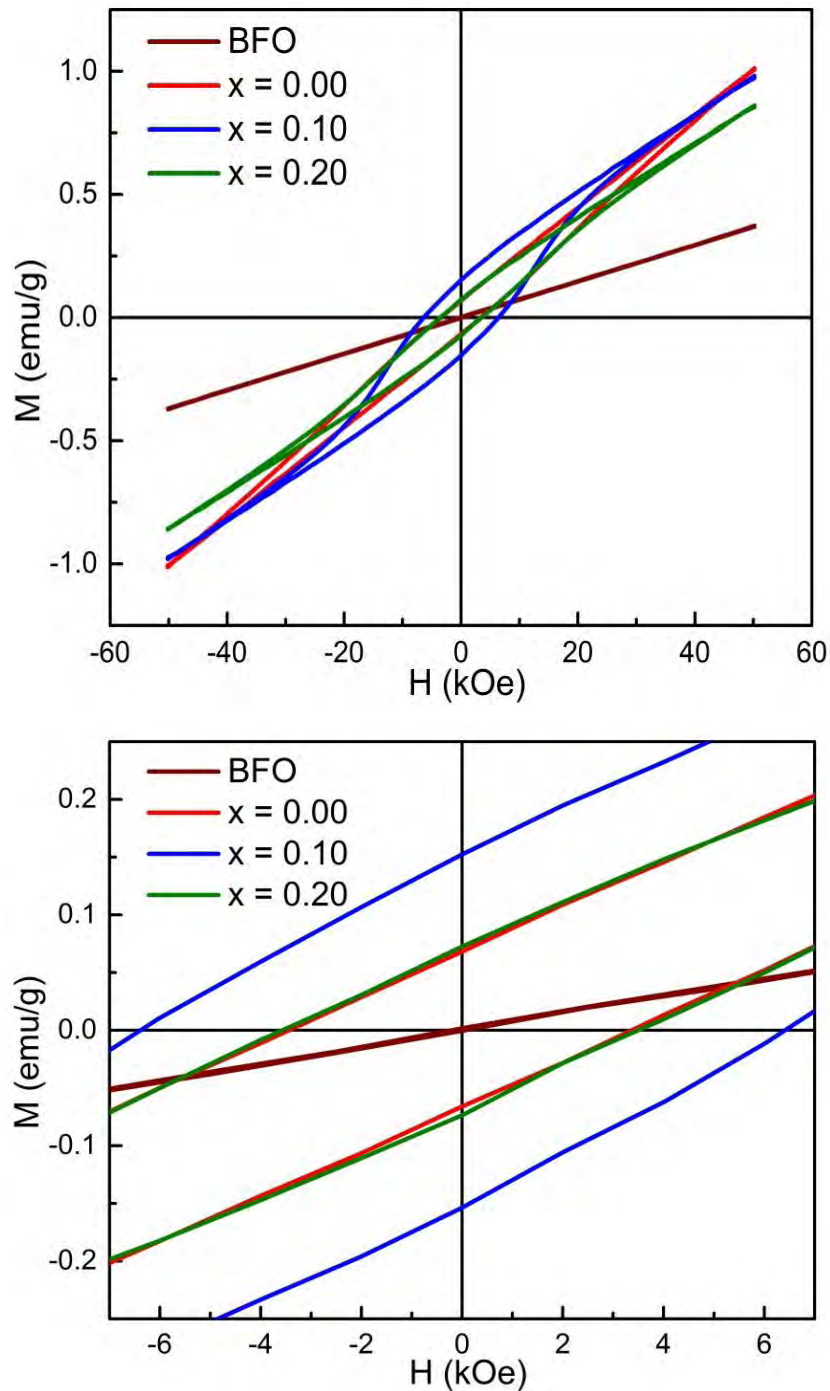


Figure 4.4: The $M - H$ hysteresis loops of undoped, Gd doped and Gd-Ti co-doped BFO ceramics were carried out at RT with an applied magnetic field of up to ± 50 kOe.

An asymmetric shift towards the magnetic field axes [19] in the $M - H$ hysteresis loops at RT is observed as depicted in Fig. 4.4. The asymmetry was shown in the Fig. 4.4 for sample $x = 0.00-0.20$. The presence of an exchange bias (EB) effect is evinced by this asymmetry phenomenon in this multiferroic material [11, 19, 20].

TABLE 4.2: The table shows the calculated values of M_r , H_c and H_{EB} for undoped BiFeO_3 , Gd doped $\text{Bi}_{0.9}\text{Gd}_{0.1}\text{Fe}_{1-x}\text{Ti}_x\text{O}_3$ ($x = 0.00$) and Gd-Ti co-doped $\text{Bi}_{0.9}\text{Gd}_{0.1}\text{Fe}_{1-x}\text{Ti}_x\text{O}_3$ ($x = 0.10-0.20$) ceramics observed at RT.

Samples	M_r (emu/g)	H_c (Oe)	H_{EB} (Oe)
BFO	0.001	132	81
0.00	0.065	3406	33
0.10	0.155	6399	-13
0.20	0.073	3532	40

As mentioned earlier, the hysteresis loops of these ceramics showed in Fig.4.4, confirm the basic AFM nature of the compounds. We notice that the centers of $M - H$ loops of $\text{Bi}_{0.9}\text{Gd}_{0.1}\text{Fe}_{1-x}\text{Ti}_x\text{O}_3$ ($x = 0.00-0.20$) compounds get widened when compared to undoped BFO. This provides an indication of their weak ferromagnetic nature [21]. The temperature dependent magnetization curves [21] further assert this weak ferromagnetic nature as described later on. I presume that this multiferroic material system bears the coexistence of the anisotropic ferri/ferromagnetic (FM) and anti-ferromagnetic domains. The exchange coupling at the interfaces between the multiple magnetic domains, forces the system to act as a natural system for generating EB effect [15, 22–24].

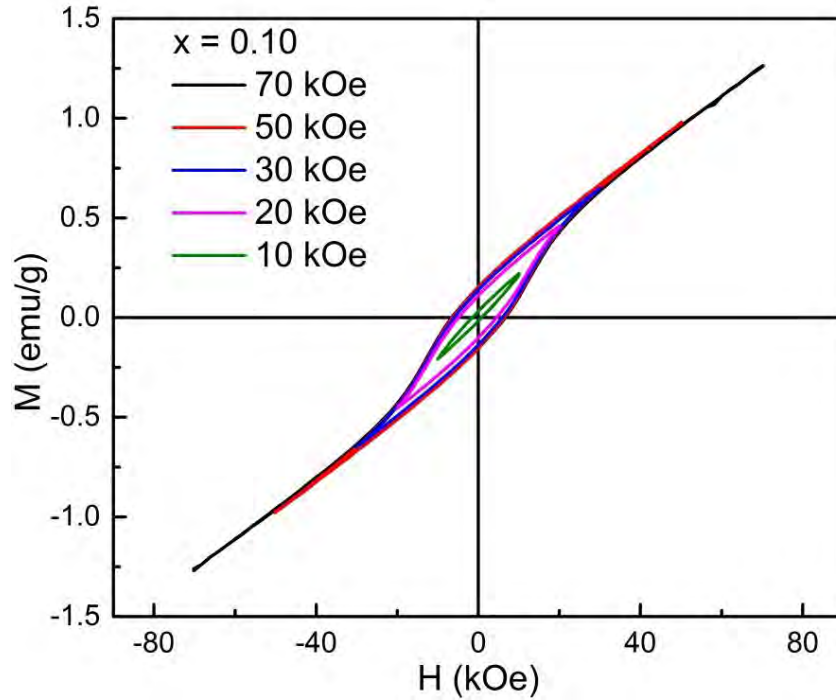


Figure 4.5: The $M - H$ hysteresis loops of 10% Gd and Ti co-doped $\text{Bi}_{0.9}\text{Gd}_{0.1}\text{Fe}_{0.9}\text{Ti}_{0.1}\text{O}_3$ ceramics for different H_{\max} at RT.

The quantification of the exchange bias field (H_{EB}) found from the loop asymmetry along the field axis was performed using $H_{EB} = -(H_{c1} + H_{c2})/2$ where H_{c1} and H_{c2} are the left and right coercive fields, respectively [19, 22]. The variation of H_{EB} calculated from the asymmetric shift of the M-H hysteresis loops was inserted in Table 4.2. Generally, the EB effect is observed when a system is cooled down in an external magnetic field through the Neel temperature (T_N). Notably, the BiFeO_3 ceramic system exhibited the EB effect without any quintessential method of inducing unidirectional anisotropy [25] during the magnetic field annealing process through T_N [26]. This ceramic system also showed the EB effect without using any alloy layers [27] at RT.

The coupling strength of an exchange bias system is indicated by the EB fields. The H_{EB} values inserted in Table 4.2 are observed without applying any cooling magnetic field and therefore the biasing strength is weak and random. The effect of temperature and cooling magnetic fields on EB effect of this multiferroic system is elaborately described in Ref. [28]. Previously, EB effect has been observed in various bulk materials, however, this effect in most cases was limited to far below RT ($< 100\text{K}$) [29–31] making the systems less lucrative for applications. Therefore, the observation of EB in this co-doped BFO multiferroics up to RT, albeit small, is promising from the perspective of practical applications.

Notably, the $M-H$ hysteresis loops of this multiferroic ceramic at RT demonstrate the unsaturated magnetization behavior even by applying a high magnetic field of up to ± 50 kOe. The cation doped multiferroic materials which involve mixed magnetic ordering with large anisotropy do not show a saturating trend even for $H > 50$ kOe. Thus, the proper choice of maximum field applied for recording a magnetic hysteresis loop, H_{max} is crucial for investigating the magnetization parameters, in particular to investigate the EB effect at RT.

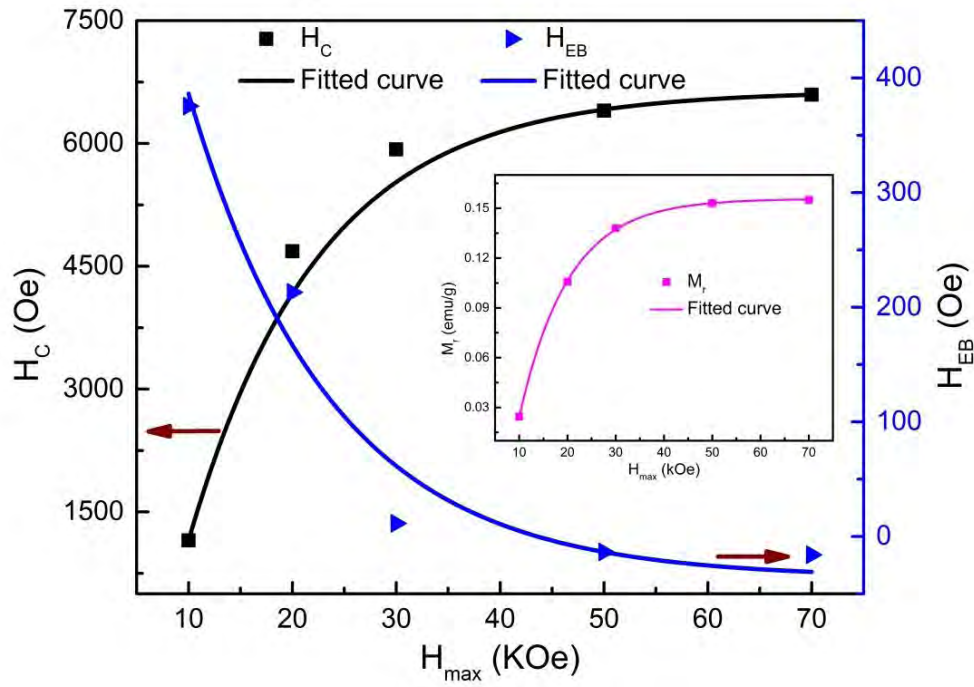


Figure 4.6: The variation of H_c and H_{EB} of 10% Gd and Ti co-doped $\text{Bi}_{0.9}\text{Gd}_{0.1}\text{Fe}_{0.9}\text{Ti}_{0.1}\text{O}_3$ material as a function of maximum applied magnetic fields. The inset shows the variation of M_r also as a function of H_{max} .

Therefore, we have carried out $M - H$ hysteresis loops at different maximum applied magnetic fields (H_{max}) for 10% Gd and Ti co-doped $\text{Bi}_{0.9}\text{Gd}_{0.1}\text{Fe}_{0.9}\text{Ti}_{0.1}\text{O}_3$ samples as showed in Fig. 4.6. This particular composition was chosen due to its improved structural properties with significantly reduced impurities. The magnetization parameters were calculated from the respective $M-H$ loops (Fig. 4.5). The influence of measuring magnetic fields on the H_c and H_{EB} are shown in Fig. 4.6. The inset of Fig.4.6 shows the variation of M_r with H_{max} . The H_c and M_r were found to increase with H_{max} while recording a hysteresis loop, however, the H_{EB} decreased. Notably, the H_c , M_r and H_{EB} values are almost stabilized (considering experimental values) at higher H_{max} i.e. at $>30\text{kOe}$. Moreover, at RT, we observed a transition from positive to negative exchange bias with decreasing H_{max} to record the respective hysteresis loops. A similar transition was observed in $\text{La}_{0.5}\text{Sr}_{0.5}\text{Mn}_{0.8}\text{Co}_{0.2}\text{O}_3$ ceramics at temperature much lower than RT [31].

Temperature Dependent Magnetic Hysteresis (M-H) Loops:

For magnetic characterization, the $M-H$ hysteresis loops of $\text{Bi}_{0.9}\text{Gd}_{0.1}\text{Fe}_{1-x}\text{Ti}_x\text{O}_3$ ($x = 0.00-0.20$) samples were measured at different temperatures ranging from 20 K to 300 K with an applied magnetic field of up to 50 kOe. As a typical example, the $M-H$ loops of sample $x = 0.0$ (composition $\text{Bi}_{0.9}\text{Gd}_{0.1}\text{FeO}_3$) at different temperatures were presented in figure 4.7 (a). Figures 4.7 (b-h) demonstrate an enlarge view of the low field $M-H$ hysteresis loops of this sample measured at temperatures: (b) 20 K (c) 50 K (d) 100 K (e) 150 K (f) 200 K (g) 250 K and (h) 300 K.

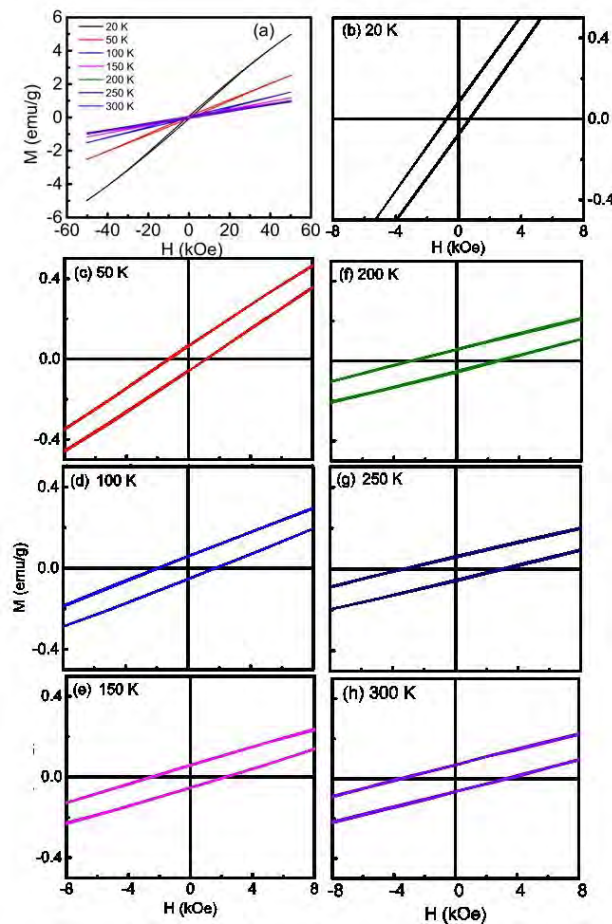


Figure 4.7: (a) The $M-H$ hysteresis loops of sample $x = 0.00$ (composition $\text{Bi}_{0.9}\text{Gd}_{0.1}\text{FeO}_3$) carried out at different temperatures. (b-h) An enlarged view of the low field $M-H$ hysteresis loops of sample $x = 0.00$ obtained at temperatures: (b) 20 K (c) 50 K (d) 100 K (e) 150 K (f) 200 K (g) 250 K and (h) 300 K.

Figure 4.7(a) demonstrates the $M - H$ hysteresis loops of $\text{Bi}_{0.9}\text{Gd}_{0.1}\text{Fe}_{1-x}\text{Ti}_x\text{O}_3$ ($x = 0.00$) sample measured at different temperatures. This is a Ti undoped and only Gd doped $\text{Bi}_{0.9}\text{Gd}_{0.1}\text{FeO}_3$ multiferroic material. The asymmetric shift along the field axes are shown in the enlarged view at temperatures: (b) 20 K (c) 50 K (d) 100 K (e) 150 K (f) 200 K (g) 250 K and (h) 300 K. Figure 4.8 (a) demonstrates the $M-H$ hysteresis loops of $\text{Bi}_{0.9}\text{Gd}_{0.1}\text{Fe}_{1-x}\text{Ti}_x\text{O}_3$ ($x = 0.10$) sample measured at different temperatures. The asymmetric shift along the magnetic field axes are also shown separately in the enlarge view at temperatures: (b) 20 K (c) 50 K (d) 100 K (e) 150 K (f) 200 K (g) 250 K and (h) 300 K. The value of the exchange bias field at different temperatures in $\text{Bi}_{0.9}\text{Gd}_{0.1}\text{Fe}_{1-x}\text{Ti}_x\text{O}_3$ ($x = 0.00$ and 0.20) compositions are shown in table 4.3.

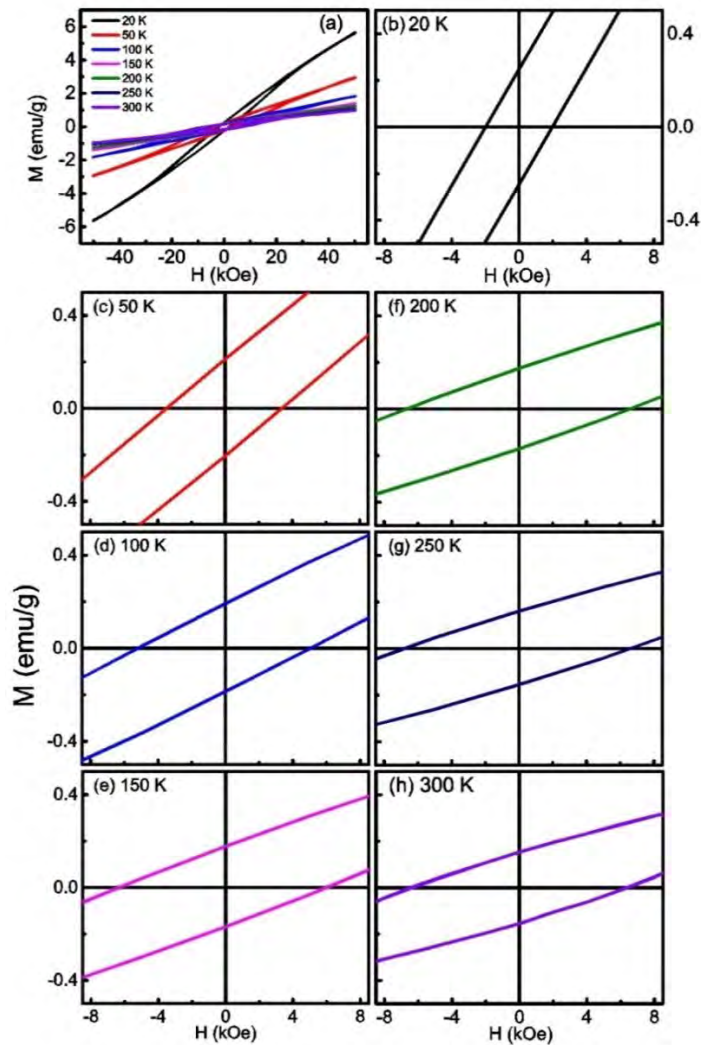


Figure 4.8: (a) The $M - H$ hysteresis loops of sample $x = 0.10$ (composition $\text{Bi}_{0.9}\text{Gd}_{0.1}\text{Fe}_{0.9}\text{Ti}_{0.1}\text{O}_3$) carried out at different temperatures. (b-h) An enlarged view of the low field $M - H$ hysteresis loops of sample $x = 0.10$ obtained at temperatures: (b) 20 K (c) 50 K (d) 100 K (e) 150 K (f) 200 K (g) 250 K and (h) 300 K.

As shown in figure 4.7 and figure 4.8 and figure 4.9, the Gd and Ti co-doped $\text{Bi}_{0.9}\text{Gd}_{0.1}\text{Fe}_{1-x}\text{Ti}_x\text{O}_3$ ($x = 0.00-0.20$) samples show unsaturated magnetization loops even with an applied magnetic field of up to 50 kOe which confirm the basic antiferromagnetic nature of the compounds. Notably, pure BiFeO_3 possesses a very narrow hysteresis loop with a very small but non-zero remanent magnetization (0.0009emu/g) and a coercive field of 110 Oe at room temperature [11]. Compared to pure BiFeO_3 , the center of M-H loops of $\text{Bi}_{0.9}\text{Gd}_{0.1}\text{Fe}_{1-x}\text{Ti}_x\text{O}_3$ ($x = 0.00-0.20$) compounds are wider (as shown typically in the enlarged view of sample $x=0.1$, figures 4.8(b-h)) which indicate the co-existence of weak ferromagnetic nature along with the antiferromagnetic nature of the compounds [52].

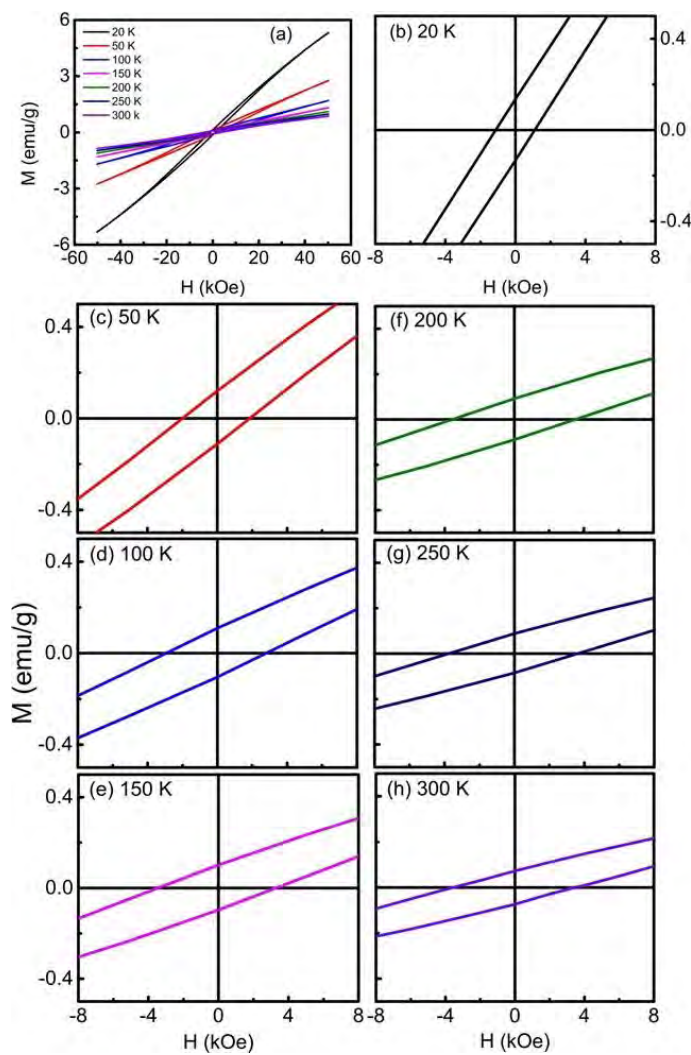


Figure 4.9: (a) The M-H hysteresis loops of sample $x = 0.20$ (composition $\text{Bi}_{0.9}\text{Gd}_{0.1}\text{Fe}_{0.8}\text{Ti}_{0.2}\text{O}_3$) carried out at different temperatures. (b-h) An enlarged view of the low field M-H hysteresis loops of sample $x = 0.20$ obtained at temperatures: (b) 20 K (c) 50 K (d) 100 K (e) 150 K (f) 200 K (g) 250 K and (h) 300 K.

Effect of Temperature on Coercive Field (H_c) and Remanent Magnetization (M_r):

From the hysteresis loops, the coercive fields (H_c) and remanent magnetization (M_r) were quantified as: $H_c = (H_{c1} - H_{c2})/2$, where H_{c1} and H_{c2} are the left and right coercive fields [11,15] and $M_r = |(M_{r1} - M_{r2})|/2$ where M_{r1} and M_{r2} are the magnetization with positive and negative points of intersection with $H = 0$, respectively [32]. Calculated values of H_c and M_r are plotted as a function of temperature in figures 4.10 (a and b) respectively $\text{Bi}_{0.9}\text{Gd}_{0.1}\text{Fe}_{1-x}\text{Ti}_x\text{O}_3$ ($x = 0.00-0.20$) samples. Both the coercive fields and remanent magnetizations are higher for sample $x = 0.10$ than those for $x = 0.00$ and $x = 0.20$. Therefore, it is clear that the substitution of 10% Ti in place of Fe in $\text{Bi}_{0.9}\text{Gd}_{0.1}\text{FeO}_3$ compound significantly increased H_c and M_r . However, a further increment of Ti to 20% in place of Fe reduced H_c and M_r although their net values are still higher than that of Ti undoped $\text{Bi}_{0.9}\text{Gd}_{0.1}\text{FeO}_3$ sample.

In a previous investigation [11], the larger values of H_c and M_r in sample $x = 0.10$ are related with the microstructure of the composition i.e. with homogeneous small grain size of the material. In the case of La and Nb co-substituted BiFeO_3 [17] and Pr and Zr co-substituted BiFeO_3 compounds [34], increase in coercive field with the substitution was also attributed to decrease in grain size. The value of H_c in these materials are much larger than that in pure BiFeO_3 [35, 11] and such a large value of coercivity in Gd and Ti co-substituted BiFeO_3 samples may be related to their magnetic anisotropy [35, 36, 37].

Notably, at RT the $M-H$ hysteresis loops of this multiferroic ceramic demonstrate the unsaturated magnetization behavior even by applying a high magnetic field of up to ± 50 kOe. The cation doped multiferroic materials which involve mixed magnetic ordering with large anisotropy do not show a saturating trend even for $H > 50$ kOe.

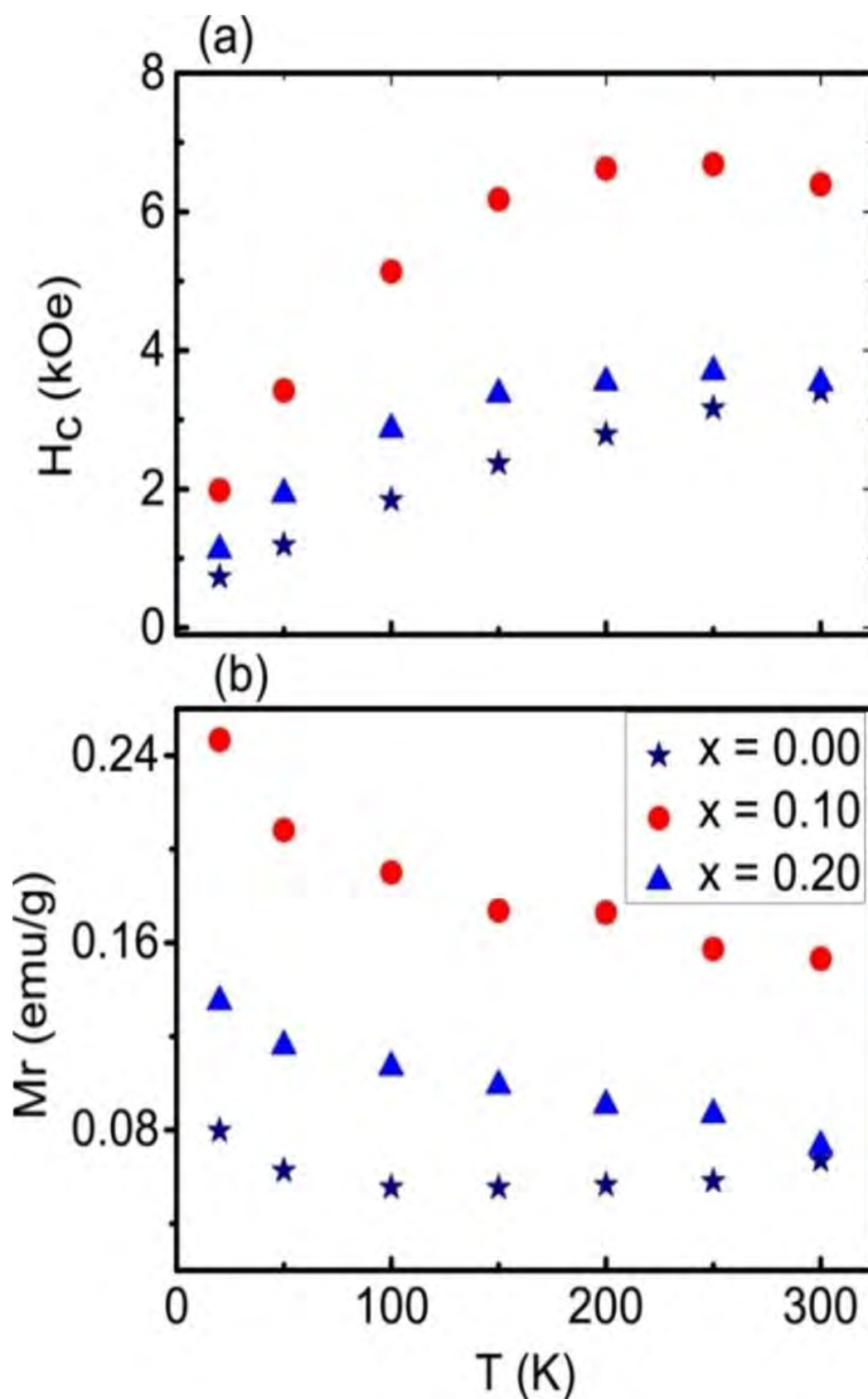


Figure 4.10: The variation of (a) coercivity (H_c) and (b) remanent magnetization (M_r) as a function of temperature in $\text{Bi}_{0.9}\text{Gd}_{0.1}\text{Fe}_{1-x}\text{Ti}_x\text{O}_3$ ($x = 0.00-0.20$) compounds. Both H_c and M_r are higher over a wide range of temperatures in sample $x = 0.10$.

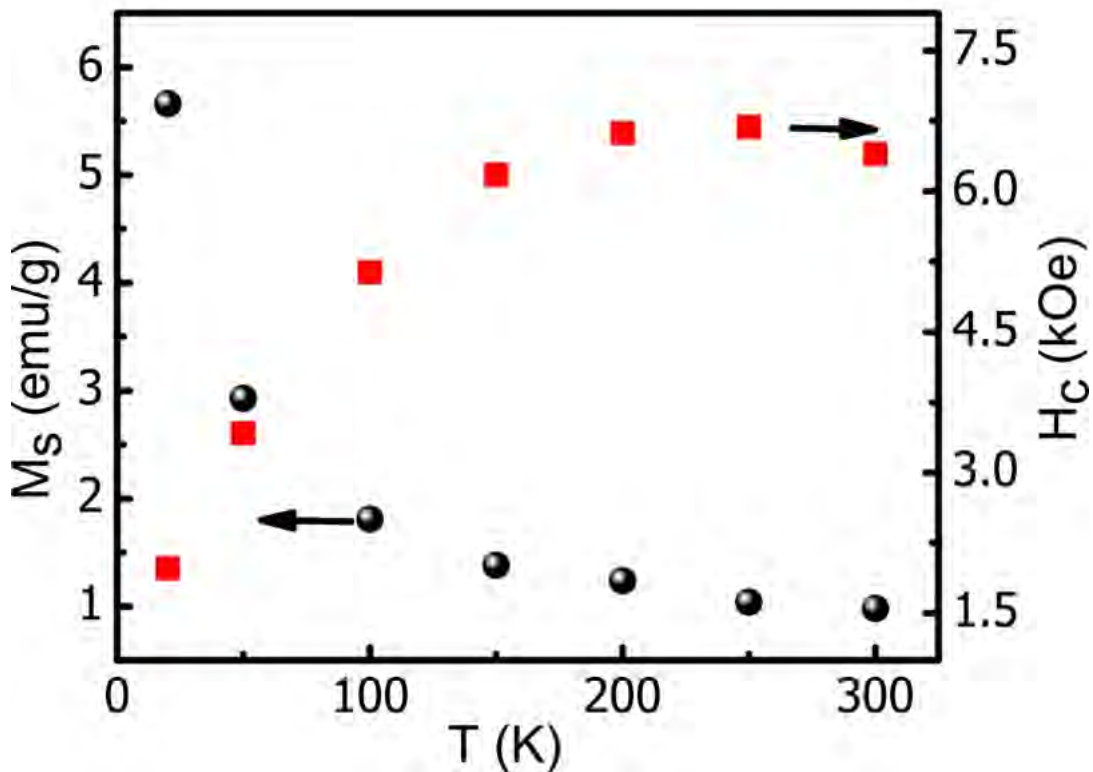


Figure 4.11: The variation of M_s (the maximum magnetization at 50 kOe) and H_c as a function of temperature in sample $x = 0.10$ ($\text{Bi}_{0.9}\text{Gd}_{0.1}\text{Fe}_{0.9}\text{Ti}_{0.1}\text{O}_3$).

The remarkable feature observed from figure 4.10 is that the coercivity of these ceramic samples increases with temperature. Figure 4.11 shows, as a typical example for $x = 0.10$ sample, that while the coercivity increases with increasing temperature, the maximum magnetization (M_s) at 50 kOe decreases with increasing temperature [38]. For all studied samples, the coercivity shows a strong temperature dependency and the H_c values are significantly higher at room temperature than that at 20 K. For example, the H_c value at room temperature for sample $x = 0.10$ is three times higher than that at 20 K.

The usual trend in a typical magnetic system is for the coercivity to increase with decreasing temperature [22,24,39] since the anisotropy decreases much more sharply than does the magnetization with increasing temperature [40]. In similar multiferroic material systems, e.g. La doped BiFeO_3 [36,37] and LuFe_2O_4 [41], the H_c values were found to increase at low temperature than that at room temperature. The unexpected decreasing trend of H_c at low temperature as compared with the room temperature

values for all the compositions may be explained by the presence of magnetoelectric coupling in these multiferroic materials [38, 40].

The presence of the magnetoelectric coupling produces additional contribution to the anisotropy that actually acts to decrease the effective magnetic anisotropy [38,40]. If K_u is the uniaxial anisotropy constant in the absence of coupling effects and K'_u is the uniaxial anisotropy constant in the presence of magnetoelectric coupling, then

$$K'_u = K_u - \chi_{\perp} (\beta P_z)^2/2$$

Here β is the homogeneous magnetoelectric co-efficient that is related to the Dzyaloshinsky Moriya magnetic field, χ_{\perp} is the magnetic susceptibility in the direction perpendicular to the antiferromagnetic vector, P_z is the spontaneous electric polarization [40, 42]. Thus the temperature variation in H_c is determined by the competition between the magnetic anisotropy and the magnetoelectric coupling [38, 40,42].

The higher values of H_c and M_r in sample $x = 0.10$ than those of $x = 0.00$ and 0.20 compositions motivated us to investigate further its magnetic and electric properties in details. Therefore, we have carried out the temperature dependence of the magnetization (M-T) of $\text{Bi}_{0.9}\text{Gd}_{0.1}\text{Fe}_{0.9}\text{Ti}_{0.1}\text{O}_3$ bulk sample.

Temperature Dependent Magnetization:

The M-T curves measured in zero fields cooled (ZFC) and field-cooled (FC) modes in the presence of 500 Oe applied magnetic field is shown in figure 4.12, figure 4.13 and figure 4.14. In the ZFC process, the sample was initially cooled from 300 to 5 K and data were collected while heating in the presence of the applied field. On the other hand, in the FC mode, data values are collected while cooling in the presence of the magnetic field which is commonly known as cooling magnetic field [33]. Here the temperature dependence magnetization measurements demonstrate clearly that both ZFC and FC curves of $\text{Bi}_{0.9}\text{Gd}_{0.1}\text{Fe}_{0.9}\text{Ti}_{0.1}\text{O}_3$ ceramic coincide with each other without showing any bifurcation which indicates the absence of any spin flipping effect [43,44]. In similar multiferroic materials both the ZFC and FC curves were also found to coincide with each other [45, 46].

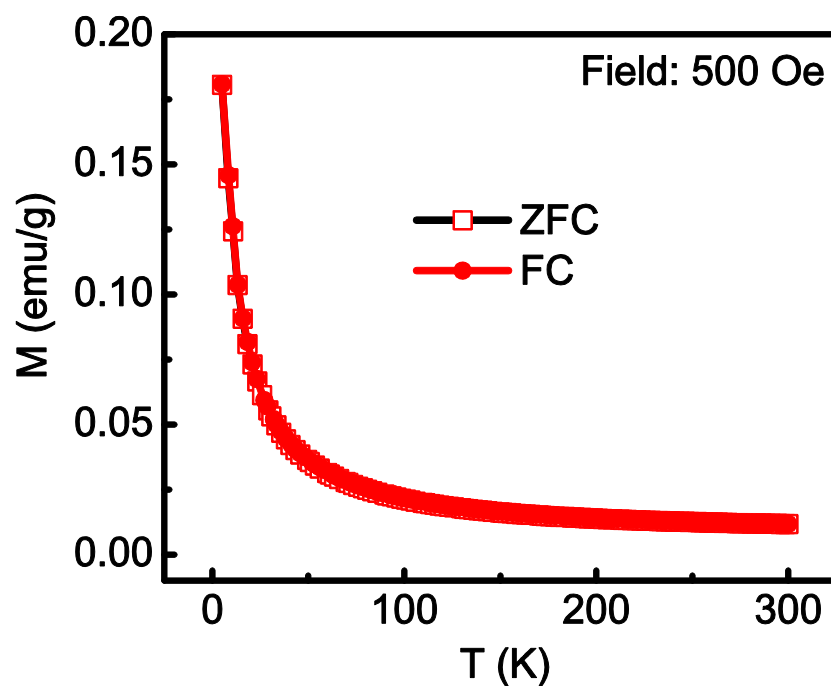


Figure 4.12: The temperature dependence of magnetization (M-T curves) of $\text{Bi}_{0.9}\text{Gd}_{0.1}\text{FeO}_3$ sample measured in ZFC and FC processes in the presence of 500 Oe applied magnetic fields. Both ZFC and FC curves coincide with each other without showing any bifurcation.

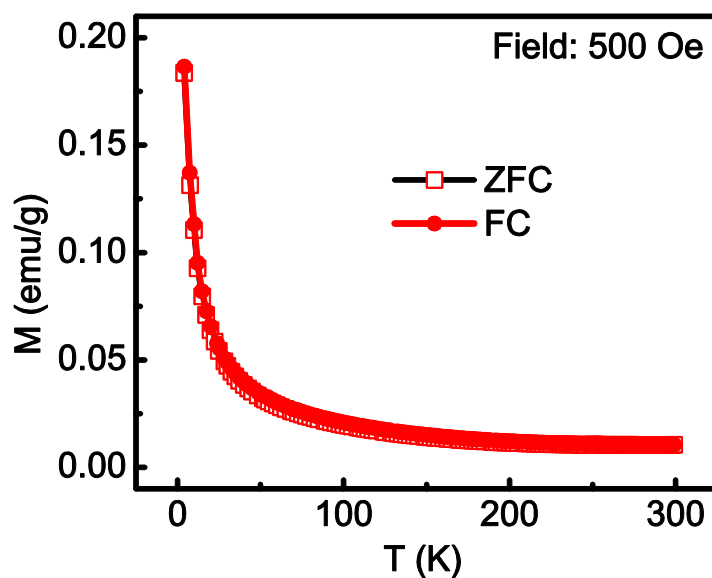


Figure 4.13: The temperature dependence of magnetization (M-T curves) of $\text{Bi}_{0.9}\text{Gd}_{0.1}\text{Fe}_{0.9}\text{Ti}_{0.1}\text{O}_3$ sample measured in ZFC and FC processes in the presence of 500 Oe applied magnetic fields. Both ZFC and FC curves coincide with each other without showing any bifurcation.

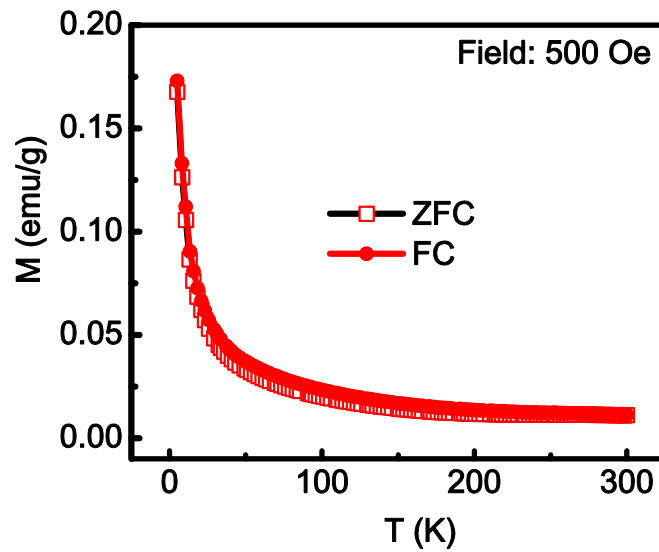


Figure 4.14: The temperature dependence of magnetization (M-T curves) of $\text{Bi}_{0.9}\text{Gd}_{0.1}\text{Fe}_{0.8}\text{Ti}_{0.2}\text{O}_3$ sample measured in ZFC and FC processes in the presence of 500 Oe applied magnetic fields. Both ZFC and FC curves coincide with each other without showing any bifurcation.

As shown in figures 4.7, figure 4.8 and figure 4.9 (a-h), the room temperature M-H hysteresis loop as well as the loops taken at other temperatures exhibit an asymmetric shift towards the magnetic field axes [52]. This is a signature of the presence of an exchange bias effect in multiferroic $\text{Bi}_{0.9}\text{Gd}_{0.1}\text{Fe}_{0.9}\text{Ti}_{0.1}\text{O}_3$ material [11, 52, 43].

In the present investigation, the hysteresis loops of Gd and Ti co-doped BiFeO_3 ceramic system is unsaturated even with an applied magnetic field of up to ± 50 kOe which confirm the basic antiferromagnetic nature of the compounds. Notably, undoped BiFeO_3 possesses a very narrow hysteresis loop with a very small but non-zero remanent magnetization (0.0009 emu/g) and a coercive field of ~ 110 Oe at room temperature [11]. Compared to pure BiFeO_3 , the center of M-H loops of $\text{Bi}_{0.9}\text{Gd}_{0.1}\text{Fe}_{1-x}\text{Ti}_x\text{O}_3$ ($x = 0.00-0.20$) compounds are wider (as shown typically in the enlarged view of sample $x = 0.10$, figures 4.8(b-h)) which suggests a weak ferromagnetic nature [21] of this co-doped ceramic system. The weak ferromagnetic nature of this material system is also revealed from temperature dependent magnetization curves [21]. In this way we anticipate the co-existence of strong-anisotropic ferri/ferromagnetic (FM) and antiferromagnetic domains in this

multiferroic material system. As a consequence of the exchange coupling between these multiple magnetic domains, it is expected that the system acts as a natural system for generating EB effect in $\text{Bi}_{0.9}\text{Gd}_{0.1}\text{Fe}_{0.9}\text{Ti}_{0.1}\text{O}_3$ multiferroics[15, 22, 23, 24]. The exchange bias field (H_{EB}) from the loop asymmetry along the field axis can be quantified as

$$H_{EB} = -(H_{c1} + H_{c2})/2$$

Where H_{c1} and H_{c2} are the left and right coercive fields, respectively [22,52]. The variation of H_{EB} as a function of temperature in $\text{Bi}_{0.9}\text{Gd}_{0.1}\text{Fe}_{0.9}\text{Ti}_{0.1}\text{O}_3$ calculated from the asymmetric shift of the M-H hysteresis loops of figures 4.8(b-h) is shown in figure 4.15. The temperature dependence of H_{EB} for two other compositions were calculated from the asymmetric shift of the M-H hysteresis loops of figures 4.7(b-h) and 4.9(b-h) and presented in the information table 4.3[11].

As was mentioned earlier, the EB effect usually occurs when the system is cooled down in an external magnetic field through the Neel temperature (T_N). It is worth mentioning that in BiFeO_3 ceramic system the exchange bias effect was observed without any magnetic field annealing process through T_N [26] which is the conventional method of inducing unidirectional anisotropy[25]. It has also been observed without using any alloy layers [48], however, then the biasing strength of BiFeO_3 is observed to be very weak with $H_{EB} = 36$ Oe [27] at room temperature. The exchange bias fields indicate the strength of the exchange coupling of an exchange bias system.

Temperature dependent exchange bias field without applying cooling magnetic field:

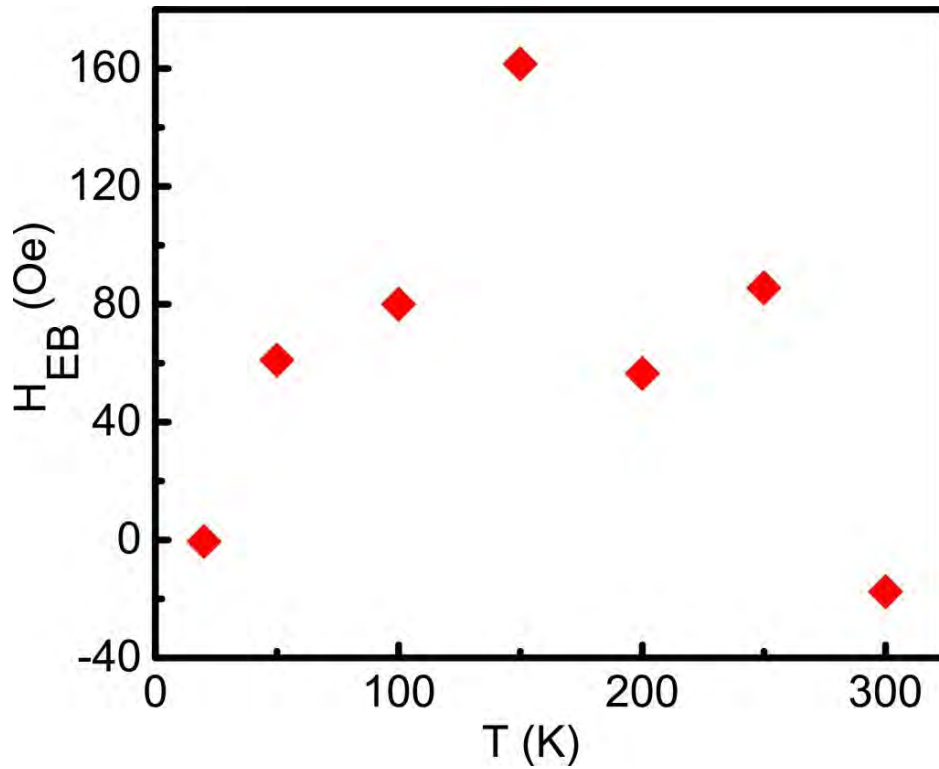


Figure 4.15: The variation of exchange bias fields (H_{EB}) as a function of temperature in $\text{Bi}_{0.9}\text{Gd}_{0.1}\text{Fe}_{0.9}\text{Ti}_{0.1}\text{O}_3$. The H_{EB} values were calculated from the asymmetric shift of the M - H hysteresis loops of figures 4.8 (b-h).

Table 4.3: The table shows the exchange bias fields of $\text{Bi}_{0.9}\text{Gd}_{0.1}\text{Fe}_{1-x}\text{Ti}_x\text{O}_3$ ($x = 0.00-0.20$) compositions at different temperatures.

x=	$H_{EB}(\text{Oe})$						
	T=20K	T=50K	T=100K	T=150K	T=200K	T=250K	T=300K
0.00	8	70	101	122	122	143	31
0.10	0	61	80	161	56	85	-17
0.20	7	64	61	80	26	64	33

As shown in figure 4.15, values of H_{EB} of $\text{Bi}_{0.9}\text{Gd}_{0.1}\text{Fe}_{0.9}\text{Ti}_{0.1}\text{O}_3$ at 150K and 250 K are much higher than that at any other temperatures. The values of H_{EB} shown in figure

4.15 are observed without applying any cooling magnetic field and therefore the biasing strength is weak and random. In the case of a FM/AFM bilayer system, it is well known that cooling magnetic field plays an important role in establishing a strong unidirectional anisotropy due to the exchange coupling [48]. Hence, in the following experiments, the magnetic hysteresis loops of $\text{Bi}_{0.9}\text{Gd}_{0.1}\text{Fe}_{0.9}\text{Ti}_{0.1}\text{O}_3$ material were carried out at temperatures 150 K and 250 K by cooling down the sample from 300 K in various cooling magnetic fields (H_{cool}) ranging from 20 kOe to 60 kOe. In each experiment related to cooling magnetic fields, the measuring magnetic fields were from -30 kOe to 30 kOe. The details of the loop asymmetry at different cooling fields and temperatures can be found in the figures 4.16 and 4.17 [11].

Temperature dependent Exchange bias field with applying cooling magnetic field :

The influence of cooling magnetic fields on exchange bias effect at temperatures 150 K and 250 K in $\text{Bi}_{0.9}\text{Gd}_{0.1}\text{Fe}_{0.9}\text{Ti}_{0.1}\text{O}_3$ multiferroic material is illustrated in figure 4.18. The H_{EB} values increased significantly upon the application of cooling magnetic fields. For example, at temperature 250 K and cooling magnetic field 60 kOe, the biasing field increased more than twelve times than that for a cooling magnetic field of 20 kOe. During the field cooling experiments, the H_{EB} values reduced with increasing temperature, figure 4.18, which is similar to results reported in previous investigations [33, 30, 49]. The H_{EB} values are higher than those in related material systems [33, 50] specifically at high temperatures.

In the present investigation, the temperature dependent ZFC and FC measurements (figure 4.13) demonstrate the absence of any bifurcation from 300 K down to 5 K and therefore, we had conducted the field cooling experiments by cooling the sample from 300 K down to 150 K and 250 K. By using the SQUID magnetometer (Quantum Design MPMS-XL7, USA), it was not possible to heat the sample above 300 K; therefore, the field cooling experiments were not possible to conduct by cooling down this sample through T_N which is around 520 ± 10 K for $\text{Bi}_{0.9}\text{Gd}_{0.1}\text{Fe}_{0.9}\text{Ti}_{0.1}\text{O}_3$ ceramic measured from temperature dependent dielectric measurements (data not shown here). As was mentioned earlier, the EB has been observed in various bulk materials, however, the effect in most cases has been limited to low temperatures [29, 30]. The

observation of EB up to room temperature is of interest from the perspective of practical applications. Therefore, in future we intend to conduct field cooling experiments at room temperature by cooling $\text{Bi}_{0.9}\text{Gd}_{0.1}\text{Fe}_{0.9}\text{Ti}_{0.1}\text{O}_3$ material through T_N which is above the room temperature.

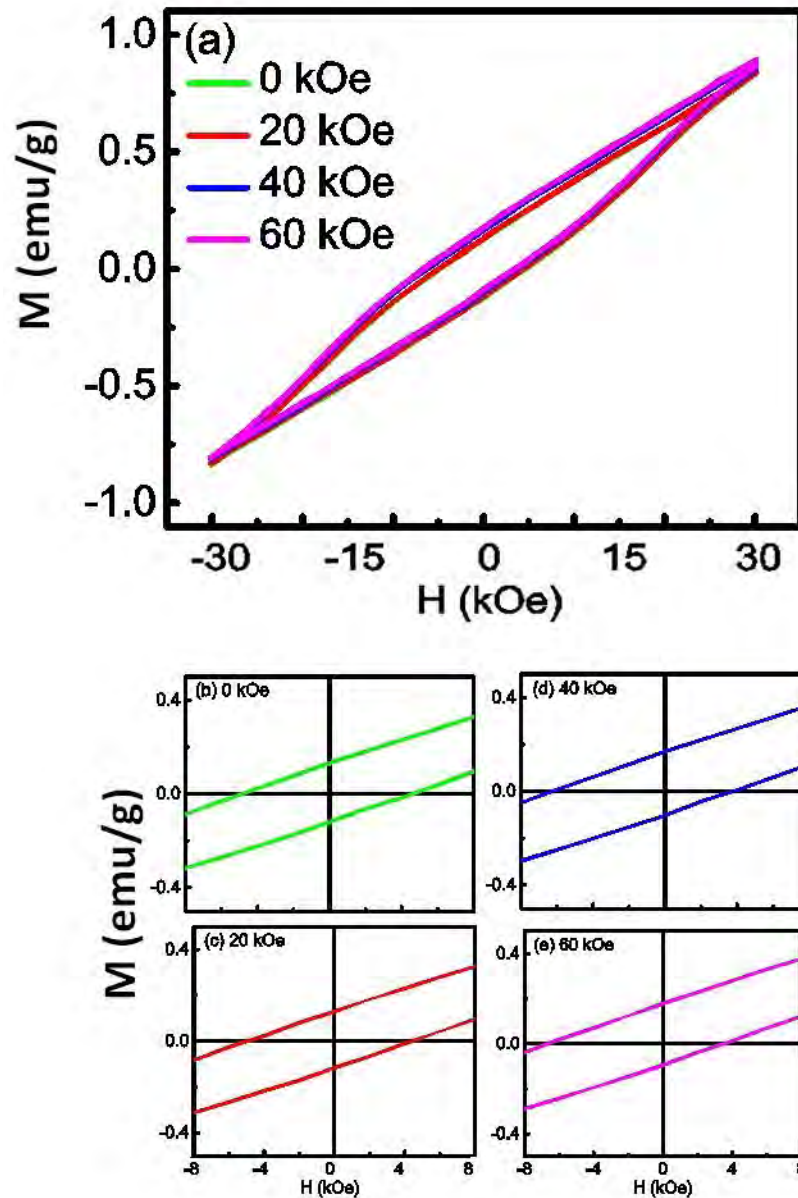


Figure 4.16: (a) The $M - H$ hysteresis loops of sample $x = 0.10$ measured at 150 K by applying cooling magnetic fields. (b-e) The enlarged views show the effect of cooling magnetic field on asymmetric shifting of the hysteresis loops.

The $M - H$ hysteresis loops of sample $x = 0.10$ measured at 150 K after being cooled from 300 K in zero field and then in separate experiments in the presence of various cooling magnetic fields are presented in figures 4.16 (a). The enlarge views, figures 4.16(b-e) demonstrate the asymmetric shifting along the field axes. Similarly,

hysteresis loops measured at 250 K after being cooled from 300K in zero field and then in the presence of various cooling magnetic fields are shown in figures 4.17(a). The enlarged views, figures 4.17(b-e) show the asymmetric shifting of the hysteresis loops along the magnetic field axes.

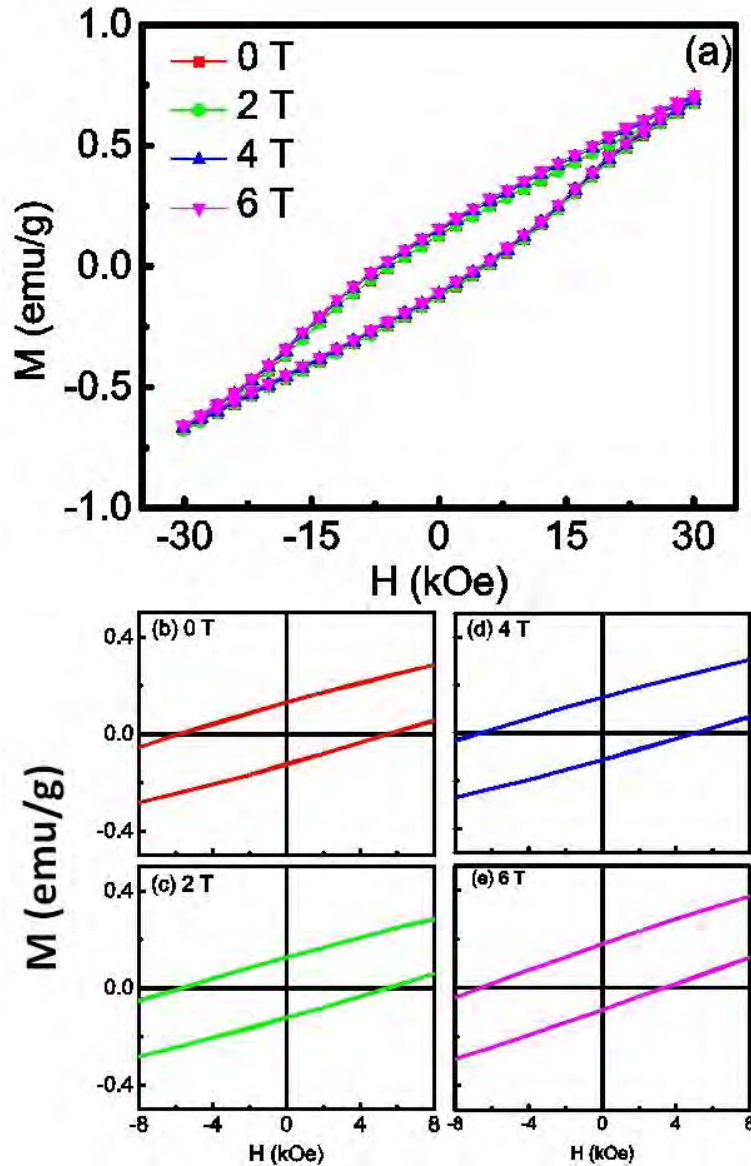


Figure 4.17: (a) The $M - H$ hysteresis loops of sample $x = 0.10$ measured at 250 K in presence of cooling magnetic fields. (b-e) The enlarged views demonstrate the effect of cooling magnetic field on asymmetric shifting of the field axes.

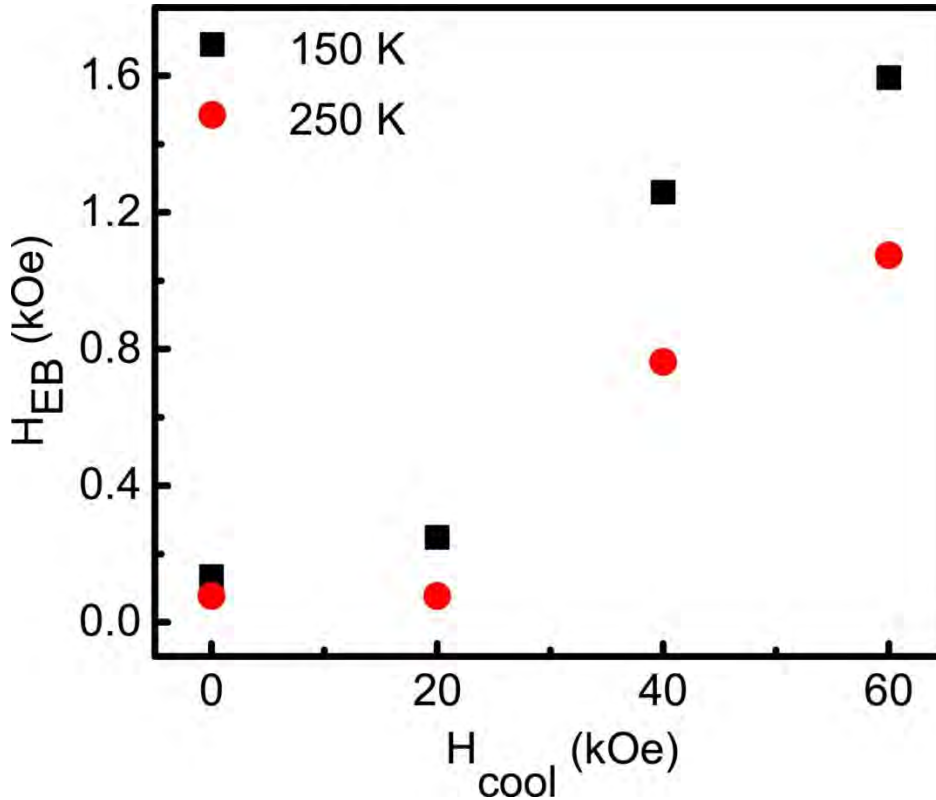


Figure 4.18: Cooling field dependence of exchange bias field (H_{EB}) at 150 K and 250 K for $\text{Bi}_{0.9}\text{Gd}_{0.1}\text{Fe}_{0.9}\text{Ti}_{0.1}\text{O}_3$ ceramic. The graph also demonstrates the dependency of H_{EB} on temperature.

Table 4.4: The table shows the effect of cooling magnetic fields on H_c of $\text{Bi}_{0.9}\text{Gd}_{0.1}\text{Fe}_{0.9}\text{Ti}_{0.1}\text{O}_3$ sample at temperatures 150 K and 250 K. Notably, the effect of temperatures on H_c of $\text{Bi}_{0.9}\text{Gd}_{0.1}\text{Fe}_{0.9}\text{Ti}_{0.1}\text{O}_3$ sample without applying cooling magnetic fields was inserted in figure 4.17.

T(k)	H_c (kOe)			
	$H_{cool}=0\text{Koe}$	$H_{cool}=20\text{Koe}$	$H_{cool}=40\text{Koe}$	$H_{cool}=60\text{Koe}$
150	4.7	4.7	5.0	5.0
250	5.6	5.6	5.8	5.8

The influence of H_{cool} on coercive field was also measured at temperatures 150 K and 250 K and the results are displayed in table 4.4. Notably, in figures 4.11, we have shown the effect of temperature on H_c without applying any cooling magnetic field. Here in table 4.4, we have inserted the effect of cooling magnetic field on H_c and the

measurements were carried out at two different temperatures close to room temperature. The exchange bias fields are strongly affected by cooling magnetic field as shown in figure 4.18, however, the H_c values (table 4.4) are influenced merely by a small extent. This is not unusual, in the case of NiFe/Co bilayers, similar effect was previously observed, i.e. the exchange bias field is strongly affected by cooling magnetic field whereas the H_c is weakly influenced [48].

In a previous investigation [25], they have synthesized nanoparticles of the same composition i.e. of $\text{Bi}_{0.9}\text{Gd}_{0.1}\text{Fe}_{0.9}\text{Ti}_{0.1}\text{O}_3$ with a mean size of 40-100 nm directly from their bulk powder by using the sonication technique described in Ref. [15]. In this specially prepared nanoparticle system, we have observed exchange bias effect and the magnitude of the exchange bias fields were also found to increase with cooling magnetic fields [52]. Obviously, the cooling field dependence of H_{EB} values of $\text{Bi}_{0.9}\text{Gd}_{0.1}\text{Fe}_{0.9}\text{Ti}_{0.1}\text{O}_3$ bulk system were weaker than those of specially prepared $\text{Bi}_{0.9}\text{Gd}_{0.1}\text{Fe}_{0.9}\text{Ti}_{0.1}\text{O}_3$ nanoparticles. For example, in both bulk and nanoparticle system the highest H_{EB} values were observed at temperature 150 K by applying 60 kOe cooling magnetic field. At this temperature and cooling magnetic field, the H_{EB} value of the bulk system is 20 % less than that of nanoparticles having sizes 40-100 nm. This is worth noting as the preparation of bulk materials is comparatively easy and straightforward considering the multistep processing for the preparation of nanoparticles.

4.4 Electric measurements

To compare the leaky behavior of undoped, Gd doped and Gd-Ti co-doped BFO ceramics, leakage current density, J versus electric field, E measurements were performed. Figure 4.19 shows that the leakage current density of 10% Gd and Ti co-doped $\text{Bi}_{0.9}\text{Gd}_{0.1}\text{Fe}_{0.9}\text{Ti}_{0.1}\text{O}_3$ bulk materials is smaller than that of other compositions. Particularly, the leakage current density of this co-doped ceramic is much small than that of undoped BFO. The high leakage current of bulk material is predominantly connected with impurity phases and oxygen vacancies[46, 47]. Therefore, it is expected that due to the substitution of Gd and Ti in BiFeO_3 the oxygen vacancies induced mainly due to the volatilization of Bi ion in the lattice was suppressed and

consequently the leakage current density was reduced. Figure 4.20 (a-d) shows the ferroelectric polarization hysteresis loops (P-E loops) of undoped, Gd doped and Gd-Ti co-doped BFO ceramic systems which were carried out by varying E-fields. The continuous increment of electric field results in the increase of remanent polarization while the driving frequency was maintained at 50 Hz. This is due to the fact that larger electric field provides higher level of driving power responsible for reversal of ferroelectric domains [48]. It is expected that in undoped BFO freely movable charges appear to contribute significantly to the electrical hysteresis loop.

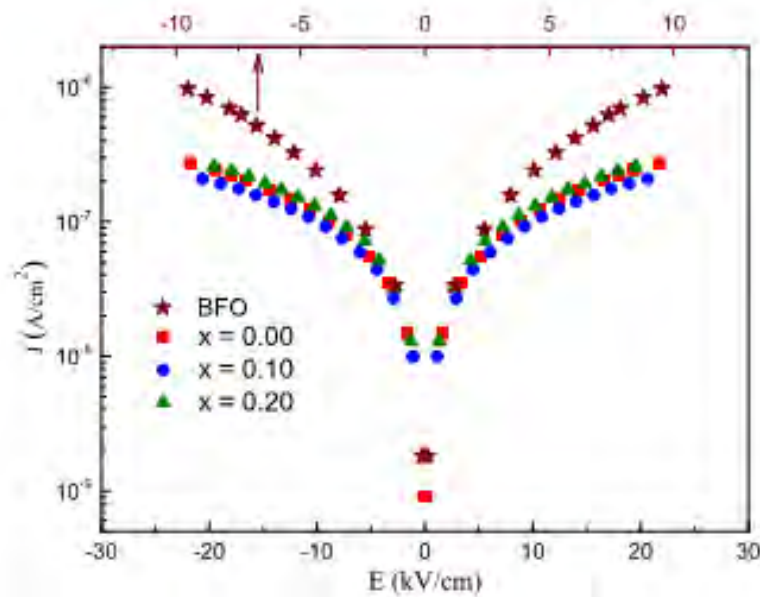


Figure 4.19: Current density of undoped, Gd doped and Gd-Ti codoped $\text{Bi}_{0.9}\text{Gd}_{0.1}\text{Fe}_{1-x}\text{Ti}_x\text{O}_3$ ($x = 0.00, 0.10$ and 0.20) materials as a function of applied electric fields. The upper x-axis is correspond to bulk BiFeO_3 .

Therefore, the undoped BFO material exhibit a round shaped P-E loop as shown in figure 4.20 (a) due to its high leakage current was evidenced in figure 4.19. The substitution of Gd in place of Bi in BiFeO_3 i.e in sample $x = 0.00$ (figure 4.20 (b)) reduces the contribution to the polarization from the freely movable charges, as evidenced by the less rounded features of the loops. The leakage current density was also found to decrease upon the substitution of Gd in place of Bi in BiFeO_3 compared to that of undoped BFO. In the case of 10%Gd and Ti co-doped $\text{Bi}_{0.9}\text{Gd}_{0.1}\text{Fe}_{0.9}\text{Ti}_{0.1}\text{O}_3$ i.e. for $x = 0.10$ composition, figure 4.20(c), the P-E loops become more and more typical which is associated with their reduced leakage current

density [49] compared to that of all other compositions. For a further increment of Ti concentration to 20% i.e. for sample $x = 0.20$, figure 4.20 (d), the shape of the loop remains elliptical, however, the remanent polarization is enhanced again probably due to the contribution of the increased freely movable charges. Hence, the electrical measurements clearly show an improved ferroelectric behavior of 10% Gd and Ti co-doped BFO material due to its reduced leakage current density.

Figures 4.20 (a-d) show the ferroelectric polarization hysteresis loops (P-E loops) of (a) undoped BiFeO_3 , (b) Gd doped $\text{Bi}_{0.9}\text{Gd}_{0.1}\text{FeO}_3$ ($x=0.00$), Gd-Ti co-doped $\text{Bi}_{0.9}\text{Gd}_{0.1}\text{Fe}_{1-x}\text{Ti}_x\text{O}_3$ with (c) $x = 0.10$ and (d) $x = 0.20$ compositions measured at selected electric fields. The P-E loops of these ceramics were carried out by varying electric fields. For a fixed driven frequency of 50 Hz, the remanent polarizations were found to increase gradually with an increase in electric field. This is due to the fact that larger electric field provides higher level of driving power responsible for reversal of ferroelectric domains [48]. It is expected that in undoped BiFeO_3 freely movable charges appear to contribute significantly to the electrical hysteresis loop.

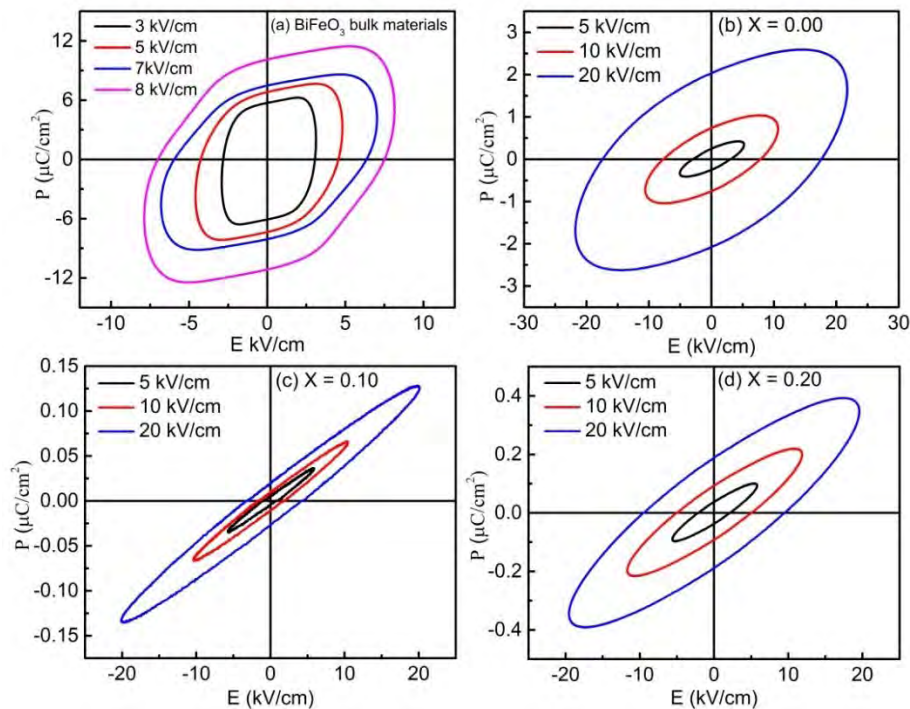


Figure 4.20: The P-E hysteresis loops of (a) undoped BFO, (b) $\text{Bi}_{0.9}\text{Gd}_{0.1}\text{FeO}_3$ ($x = 0.00$) (c) $\text{Bi}_{0.9}\text{Gd}_{0.1}\text{Fe}_{0.9}\text{Ti}_{0.1}\text{O}_3$ ($x = 0.10$) and (d) $\text{Bi}_{0.9}\text{Gd}_{0.1}\text{Fe}_{0.8}\text{Ti}_{0.2}\text{O}_3$ ($x = 0.20$) materials.

Therefore, the undoped BiFeO_3 material exhibit a round shaped P-E loop as shown in figure 4.20 (a) due to their high leakage current . Due to the substitution of Gd in

place of Bi in BiFeO_3 i.e in sample $x = 0.00$ (figure 4.20(b)), the contribution to the polarization from the freely movable charges is reduced, as evidenced by the less rounded features of the loops. The leakage current density was also found to decrease upon the substitution of Gd in place of Bi in BiFeO_3 compared to that of undoped BiFeO_3 . In the case of 10% Gd and Ti co-doped $\text{Bi}_{0.7}\text{Ba}_{0.3}\text{Fe}_{0.9}\text{Ti}_{0.1}\text{O}_3$ i.e. for $x = 0.10$ composition, figure 4.20 (c), the P-E loops become more and more typical which is associated with their reduced leakage current density [49] compared to that of all other compositions. For a further increment of Ti concentration to 20% i.e. for sample $x = 0.20$, figure 4.20(d), the shape of the loop remain elliptical, however, the remanent polarization is enhanced again probably again due to the contribution of the increased freely movable charges.

4.5 Dielectric measurements

In our previous investigation, dielectric properties of this material system were carried out as a function of frequencies [11] at RT. In this investigation, the temperature dependence of dielectric constant and dielectric loss of 10% Gd and Ti co-doped $\text{Bi}_{0.9}\text{Gd}_{0.1}\text{Fe}_{0.9}\text{Ti}_{0.1}\text{O}_3$ material was investigated at three different frequencies. Figures 4.21 (a) and (b) illustrate the variation of dielectric constant and dielectric loss as a function of temperature at frequencies 1 kHz, 10 kHz and 200 kHz. The dielectric constant as well as dielectric loss is fairly constant up to 485 ± 10 K, above this temperature both dielectric constant and loss gradually increase and a broad peak is observed around the antiferromagnetic Neel temperature, $T_N = 520 \pm 10$ K. With the increase in frequency, this peak shifts to a higher temperature and it also decreases in intensity which is a typical characteristic of relaxor ferroelectrics [57-59]. This type of dielectric anomaly around the Neel temperature may be a consequence of magnetoelectric coupling [60,61]. To confirm the dielectric anomaly, we performed the measurements at a very high frequency of 200 kHz. Interestingly, the anomaly was observed at this frequency too, as shown separately in the insets of Fig. 4.21 (a) and (b). Both the dielectric constant and dielectric loss functions exhibited the anomaly around 520 K even at 200 kHz corroborating the claim of this being a consequence of ME coupling. Here the modifications in spin structure for a typical magnetic transition are expected to be coupled with ferroelectric ordering.

These modifications ultimately cause a change in structural parameters, hence, an anomaly in dielectric behavior is likely.

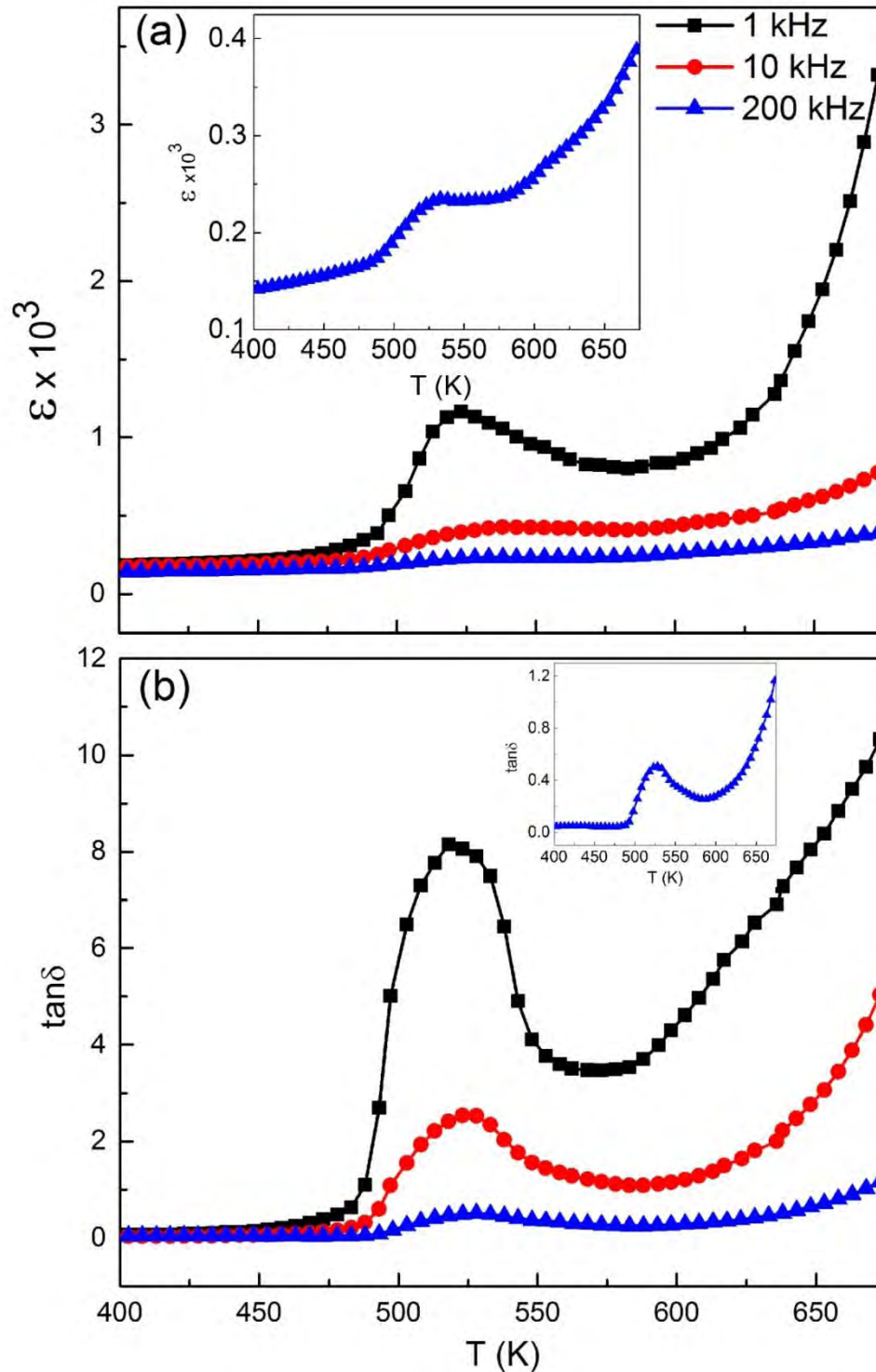


FIG. 4.21: The variation of (a) dielectric constant and (b) dielectric loss as a function of temperature in 10% Gd and Ti co-doped $\text{Bi}_{0.9}\text{Gd}_{0.1}\text{Fe}_{0.9}\text{Ti}_{0.1}\text{O}_3$ at 1 kHz, 10 kHz and 200 kHz. The dielectric anomaly is clearly visible around the antiferromagnetic Neel temperature. The insets show the zoomed in view around 520 K at 200 kHz.

References :

- [1] Makhdoom, A. R., Akhtar, M. J., Rafiq, M. A., and Hassan, M. M., “Investigation of transport behavior in Ba doped BiFeO₃”, *Ceram. Int.* 38, 3829, 2012.
- [2] Ianculescu, A., Prihor, F., Postolache, P., Mitoeriu, L., Drgan, N., and Crian, D., “Preparation, Structural and Magnetic Properties of Mn-Doped La_{0.1}Bi_{0.9}FeO₃ Ceramics”, *Ferroelectrics* 391, 67, 2009.
- [3] Kumar, M., Yadav, K.L., “Study of room temperature magnetoelectric coupling in Ti substituted bismuth ferrite system”, *J. Appl. Phys.* 100, 074111, 2006.
- [4] Brinkman, K., Iijima, T., Nishida, K., Katoda, T., and Funakubo, H., “The influence of acceptor doping on the structure and electrical properties of sol-gel derived BiFeO₃ thin films”, *Ferroelectrics* 357, 35, 2007.
- [5] Chaodan, Z., Jun, Y., Duanming, Z., Bin, Y., Yunyi, W., Longhai, W., Yunbo, W., and Wenli, Z., “Processing And Ferroelectric Properties Of Ti-Doped BiFeO₃ Ceramics”, *Integr. Ferroelectr.* 94, 31, 2007.
- [6] Bernardo, M.S., Jardiel, T., Peiteado, M.F., Mompean, J., Hernandez, G., Garcia, M. A., Villegas, M., and Caballero, A.C., “Intrinsic Compositional Inhomogeneities in Bulk Ti-doped BiFeO₃: Microstructure Development and Multiferroic Properties”, *Chem. Mater.* 25, 1533, 2013.
- [7] Fisher, J.G., Jang, S.H., Park, M. S., Sun, H., Moon, S.H., Lee, J. S., and Hussain, A., “The Effect of Niobium Doping on the Electrical Properties of 0.4(Bi_{0.5}K_{0.5})TiO₃-0.6BiFeO₃ Lead-Free Piezoelectric Ceramics”, *Mater.* 8, 8183, 2015.
- [8] Dang, N.V., Thanh, T.D., Hong, L.V., Lam, V. D., and Phan, T. L., “Structural, optical and magnetic properties of polycrystalline BaTi_{1-x}Fe_xO₃ ceramics”, *J. App. Phys.* 110, 043914, 2011.
- [9] Pradhan, S.K., and Roul, B. K., “Effect of Gd doping on structural, electrical and magnetic properties of BiFeO₃ electroceramic”, *J. of Phys. And Chemistry of Solids* 72, 1180, 2011.

- [10] Bernardo, M. S., Jardiel, T., Peiteado, M. F., Caballero A. C., and Villegas, M., “Reaction pathways in the solid state synthesis of multiferroic BiFeO₃”, J. Eur. Ceram. Soc. 31,3047, 2011.
- [11] Basith, M. A., Kurni, O., Alam, M. S., Sinha, B. L., and Ahmmad, B., “Room temperature dielectric and magnetic properties of Gd and Ti co-doped BiFeO₃ ceramics”, J. Appl. Phys. 115, 024102.
- [12] Rodriguez, J., Carvajal, “Satellite Meeting on powder diffraction of the XV” Congress of the IUCr 127, Toulouse, France 1990.
- [13] Rath, C., Mohanty, P., Pandey, A.C., and Mishra, N. C., “Oxygen vacancy induced structural phase transformation in TiO₂ nanoparticles”, J. Phys. D: Appl. Phys. 42, 205101, 2009 .
- [14] Lebeugle, D., Colson, D. , Forget, A., Viret, M., Bonville, P., Marucco, J. F., and Fusil, S., “Room-temperature coexistence of large electric polarization and magnetic order in BiFeO₃ single crystals”, Phys. Rev. B 76, 024116 2007.
- [15] Guo, Y., Shi, L., Zhou, S., Zhao, J., Wang, C., Liu, W., and Wei, S., “Tunable exchange bias effect in Sr-doped double perovskite La₂NiMnO₆”, J. Phys. D: Appl. Phys. 46, 175302, 2013.
- [16] Anjum, G., Kumar, R., Mollah, S., Shukla, D.K., Kumar, S., and Lee, C.G., J. “Structural, dielectric, and magnetic properties of La_{0.8}Bi_{0.2}Fe_{1-x}Mn_xO₃ (0.0≤x≤0.4) multiferroics”, App. Phys. 107, 103916 2010.
- [17] Zhai, L., Shi, Y.G., Tang, S.L., Lv, L. Y. and Du, Y.W., “Large magnetic coercive field in Bi_{0.9}La_{0.1}Fe_{0.98}Nb_{0.02}O₃ polycrystalline compound”, J. Phys. D: Appl. Phys. 42, 165004, 2009.
- [18] Sati, P.C., Arora, M., Chauhan, S., Chhoker, S., and Kumar, M., “Structural, magnetic, and optical properties of Pr and Zr codoped BiFeO₃ multiferroic ceramics”, J. Appl. Phys. 112, 094102, 2012.
- [19] Basith, M.A., Khan, F.A., Ahmmad, B., Kubota, S., Hirose, F., Ngo, D.-T., Tran, Q.-H., and Mølhav, K., “Tunable exchange bias effect in magnetic Bi_{0.9}Gd_{0.1}Fe_{0.9}Ti_{0.1}O₃ nanoparticles at temperatures up to 250 K”, J. Appl. Phys. 118, 023901, 2015.
- [20] Murthy, K.J., and Venimadhav, A., “Giant zero field cooled spontaneous exchange bias effect in phase separated La_{1.5}Sr_{0.5}CoMnO₆”, Appl. Phys. Lett. 103, 252410, 2013.

- [21] Ramachandran, B., Dixit, A., Naik, R., Lawes, G., and Rao, M.R, “Weak ferromagnetic ordering in Ca doped polycrystalline BiFeO₃”, *J. App. Phys.* 111, 023910, 2012.
- [22] Fertman, E., Dolya, S., Desnenko, V., Pozhar, L. A., Kajnakova, M., and Feher, A., “Exchange bias in phase-segregated Nd_{2/3}Ca_{1/3}MnO₃ as a function of temperature and cooling magnetic fields”, *J. App. Phys.* 115, 203906, 2014.
- [23] Qian, J. F., Nayak, A.K., Kreiner, G., Schnelle, W., and Felser, C., “Exchange bias up to room temperature in antiferromagnetic hexagonal Mn₃Ge”, *J. Phys. D: Appl. Phys.* 47, 305001, 2014.
- [24] Deng, D., Zheng, J., Yu, D., Wang, B., Sun, Avdeev, D.M., Feng, Z., Jing, C., Lu, B., Ren, W., Cao, S., and Zhang, “Cooling field tuned magnetic phase transition and exchange bias-like effect in Y_{0.9}Pr_{0.1}CrO₃”, *J.,App. Phys. Lett.* 107, 102404, 2015.
- [25] Borisov, P., Hochstrat, A., Chen, X., Kleemann, W., Binek, C., “Magnetolectric Switching of Exchange Bias”, *Phys. Rev. Lett.* 94,117203, 2005.
- [26] Dho, J., Qi, X., Kim, H., MacManus. J. L.-Driscoll, and Blamire, M.G., “Large Electric Polarization and Exchange Bias in Multiferroic BiFeO₃”, *Adv. Mater.* 18, 1445, 2006.
- [27] Yao, R., Cao, C., Zheng, C., and Lei, Q., “Lattice mismatch induced strained phase for magnetization, exchange bias and polarization in multiferroic BiFeO₃”, *RSC Adv.* 3, 24231,2013.
- [28] Ahmmad, B., Islam, M.Z., Billah, A., and Basith, M.A., “Anomalous coercivity enhancement with temperature and tunable exchange bias in Gd and Ti co-doped BiFeO₃ multiferroics”, *J. Phys. D: Appl. Phys.* 49, 095001, 2016.
- [29] Yu., P., et al., “Interface Ferromagnetism and Orbital Reconstruction in BiFeO₃–La_{0.7}Sr_{0.3}MnO₃ Heterostructures”, *Phys. Rev. Lett.* 105, 027201, 2010.
- [30] Ang, R., Sun, Y.P., Luo, X., Hao, C.Y., Zhu, X. B., and Song, W. H., “Interface Ferromagnetism and Orbital Reconstruction in BiFeO₃–La_{0.7}Sr_{0.3}MnO₃ Heterostructures”, *J. Appl. Phys.* 104, 023914, 2008.

- [31] Shang, C., Guo, S., Wang, R., Sun, Z., Xiao, H., Xu, L., Yang, C., and Xia, Z., Scientific Reports 6, 2016.
- [32] Anjum, G., Kumar, R., Mollah, S., Shukla, D. K., Kumar, S. S., Lee S., “Structural, dielectric, and magnetic properties of $\text{La}_{0.8}\text{Bi}_{0.2}\text{Fe}_{1-x}\text{Mn}_x\text{O}_3$ ($0.0 < x < 0.4$) multiferroics”, J. App.Phys., 107, 103916, 2010.
- [33] Tian, Z. M., Yuan, S. L., Zheng, X. F., Jia, L. C., Huo, S. X., Duan, H. N., Liu, L., “Spin-glass like behavior and exchange bias in multiferroic $\text{Bi}_{1/3}\text{Sr}_{2/3}\text{FeO}_3$ ceramics”, App. Phys. Lett., 96, 142516, 2010.
- [34] Sati, P.C., Arora, M., Chauhan, Chhoker, S., and Kumar, M., Structural, Magnetic, and Optical Properties of Pr and Zr Codoped BiFeO_3 Multiferroic Ceramics”, J. Appl. Phys. 112, 094102, 2012.
- [35] Rao, T.D., Asthana, S., “Evidence of improved ferroelectric phase stabilization in Nd and Sc co-substituted BiFeO_3 ”, J. Appl. Phys., 116, 164102, 2014.
- [36] Suresh, P., Srinath, S., “Observation of high coercivity in multiferroic lanthanum doped BiFeO_3 ”, Journal of Alloys and Compounds 554, 271276, 2013.
- [37] Das, S.R., Choudhary, R. N. P., Bhattacharya, P., and Katiyar, R.S., Dutta, P., Manivannan, A. and Seehra, M. S., “Structural and multiferroic properties of La modified BiFeO_3 ceramics”, J. App. Phys. 101, 034104, 2007.
- [38] Hussain, S., Hasanain, S. K., Jaffari, G. H., Ali, N. Z., Siddique, M. and Shah, S.I., “Correlation between structure, oxygen content and the multiferroic properties of Sr doped BiFeO_3 ”, J. Alloys and Compounds 622 8, 2015.
- [39] Huang, X. H., Ding, J. F., Zhang, G.Q., Hou, Y., Yao, Y.P. and Li, X.G., “Size- dependent exchange bias in $\text{La}_{0.25}\text{Ca}_{0.75}\text{MnO}_3$ nanoparticles”, Phys. Rev. B, 78, 224408 2008.
- [40] Park, T.J., Papaefthymiou, G.C., Viescas, A.J., Lee, Y., Zhou, H. and Wong, S.S., “Composition dependent magnetic properties of BiFeO_3 - BaTiO_3 solid solution nanostructures”, Phys. Rev. B, 82, 024431, 2010.
- [41] Patankar, S., Pandey(a), S.K., Reddy, V.R., Gupta, A., Banerjee, A. and Chaddah, P., “Tuning the magnetic properties of the multiferroic LuFe_2O_4 by moderate thermal treatment”, EPL, 90, 57007, 2010.

- [42] Ruetter, B., Zvyagin, S., Pyatakov, A. P., Bush, A., Li, J.-F., Belotelov, V.I., Zvezdin, A. K. and Viehland, D., “Magnetic-field-induced phase transition in BiFeO₃ observed by high-field electron spin resonance: Cycloidal to homogeneous spin order”, *Phys. Rev. B* 69 064114, 2004.
- [43] Fang, L., Liu, J., Ju, S., Zheng, F., Dong, W. and Shen, M., “Experimental and theoretical evidence of enhanced ferromagnetism in sonochemical synthesized BiFeO₃ nanoparticles”, *Appl. Phys. Lett.* 97, 242501, 2010.
- [44] Rana, D.S., Kuberkar, D.G. and Malik, S. K., “Field-induced abrupt change in magnetization of the manganite compounds (LaR)_{0.45}(CaSr)_{0.55}MnO₃ (R=Eu and Tb)”, *Phys. Rev. B*, 73, 064407, 2006.
- [45] Lu, J., Günther, A., Schrettle, F., Mayr, F., Krohns, S., Lunkenheimer, P., Pimenov, A., Travkin, V.D., Mukhin, A.A., and Eur, L., “On the room temperature multiferroic BiFeO₃: magnetic, dielectric and thermal properties”, *Phys. J. B* 75, 451-460, 2010.
- [46] Lazenka, V. V., Zhang, G., Vanacken, J., Makoed, I., Ravinski, A. F. and Moshchalkov, V. V., “Structural transformation and magnetoelectric behaviour in Bi_{1-x}Gd_xFeO₃ multiferroics”, *J. Phys. D: Appl. Phys.* 45, 125002, 2012.
- [47] Murthy J. K. and Venimadhav, X., “Giant zero field cooled spontaneous exchange bias effect in phase separated La_{1.5}Sr_{0.5}CoMnO₆”, *Appl. Phys. Lett.* 103, 252410, 2013.
- [48] Ambrosea, T., and Chien, C. L., “Dependence of exchange field and coercivity on cooling field in NiFe/CoO bilayers”, *J. App. Phys.* 83, 7222, 1998.
- [49] Huang, S., Shi, L. R., H. G. Sun, C. M. Zhu, Z. M. Tian and S. L. Yuan, “Exchange bias effect in Bi₂Fe₃AlO₉ ceramics” *Appl. Phys. Lett.* 105, 192904, 2014.
- [50] Karmakar, S., Taran, S., Bose, E., Chaudhuri, B.K., Sun, C.P. Huang, C. L., and Yang, H.D., “Evidence of intrinsic exchange bias and its origin in spin glass like disordered L_{0.5}Sr_{0.5}MnO₃ manganites (L=Y, Y_{0.5}Sm_{0.5}, and Y_{0.5}La_{0.5})” *Phys. Rev. B* 77, 144409, 2008.

- [52] Basith, M. A., Khan, F. A., Ahammad, B., Kubota, S., Hirose, F., Ngo, D. T., Tran, Q.H., Mølhave, K., “Tunable exchange bias effect in magnetic $\text{Bi}_{0.9}\text{Gd}_{0.1}\text{Fe}_{0.9}\text{Ti}_{0.1}\text{O}_3$ nanoparticles at temperatures up to 250 K”, *J. App. Phys.*, 118, 023901, 2015.
- [53] Makhdoom, A.R., Akhtar, M.J., Rafiq, M.A., and Hassan, M.M., “Investigation of transport behavior in Ba doped BiFeO_3 ”, *Ceramics International* 38, 3829, 2012.
- [54] Cheng, Z., Wang, X., Dou, S., Kimura, H., and zawa, K., “Improved ferroelectric properties in multiferroic BiFeO_3 thin films through La and Nb co-doping”, *Phys. Rev. B* 77, 092101, 2008.
- [55] Wu, M. S., Huang, Z. B., Han, C.X., Yuan, S.L., Lu, C.L., and Xia, S. C., “Enhanced multiferroic properties of BiFeO_3 ceramics by Ba and high-valence Nb co-doping”, *Solid State Com.* 152, 2142, 2012.
- [56] Haojiang, D., Ming, Z. H., Zhu, X. Qunfeng, Z. Qi, Jizhou, W., and Hui, Y., “Enhanced dielectric and ferroelectric properties of Ba and Ti co-doped BiFeO_3 multiferroic ceramics”, *J. of Alloys and Com.* 582, 273, 2014.
- [57] Singh, A., Panday, V., Kotnala, A., and Panday, D., “Direct Evidence for Multiferroic Magnetoelectric Coupling in $0.9\text{BiFeO}_3-0.1\text{BaTiO}_3$ ”, *Phys. Rev. Lett.* 101, 247602, 2008.
- [58] Bhattacharjee, S., Panday, V., Kotnala, R.K., Panday, D., “Unambiguous evidence for magnetoelectric coupling of multiferroic origin in $0.73\text{BiFeO}_3-0.27\text{PbTiO}_3$ ”, *Appl. Phys. Lett.* 94, 012906, 2009.
- [59] Ray, Sinha, N., and Kumar ,B., “Environment friendly novel piezoelectric $0.94[\text{Na}_{0.8}\text{K}_{0.2}\text{NbO}_3]-0.06\text{LiNbO}_3$ ternary ceramic for high temperature dielectric and ferroelectric applications”, *Mater. Chem. Phys.* 142, 619, 2013.
- [60] Chauhana, S., Kumara, M., Chhokera, S., K. H., Singh, S. C., Jewariya, M., and Yadav, K. L., “Multiferroic, magnetoelectric and optical properties of Mn doped BiFeO_3 nanoparticles”, *Solid State Commun.* 152, 525, 2012.
- [61] Eerenstein, W., Mathur, N. D., Scott, J. F., “Multiferroic and magnetoelectric materials”, *Nature* 442, 759-765, 2006.

Chapter 5

Summary and Conclusions

5.1 Summary

The Gd and Ti co-doped multiferroic bulk polycrystalline materials were prepared by conventional solid state reaction technique and characterized by using a number of techniques. The outcomes of this investigation are summarized as,

- The FESEM images demonstrated that the grain size was reduced with simultaneous substitution of Gd and Ti in Bi and Fe sites of BiFeO₃ respectively.
- The major phase rhombohedral R3c is 97.16 % in 10% Gd and Ti co-doped Bi_{0.9}Gd_{0.1}Fe_{0.9}Ti_{0.1}O₃.
- Both H_c and M_r are higher over a wide range of temperatures in 10% Gd and Ti co-doped BFO material.
- The coercive fields of this multiferroic system were enhanced anomalously with increasing temperature. The anomalous enhancement of the coercivity with increasing temperature and particularly the observation of the high values of H_c near/at room temperature may be of future use in potential applications where a coercivity stability at high temperature is crucially effective.
- ZFC and FC curves coincide with each other without showing any bifurcation.
- The presence of exchange bias effect due to the interface exchange coupling between FM and AFM domains of Gd and Ti co-doped BiFeO₃ material system was observed. The magnitude of the exchange bias fields in bulk Bi_{0.9}Gd_{0.1}Fe_{0.9}Ti_{0.1}O₃ were also found to increase with cooling magnetic field.

- The electrical measurements clearly show an improved ferroelectric behavior of 10% Gd and Ti co-doped BiFeO₃ material due to its reduced leakage current density.
- The broad peak of dielectric constant near T_N is frequency dependent and shifts to a higher temperature and decreases in intensity with an increase in frequency.

5.2 Conclusions

The compendium of these investigations is that the nominal composition of 10% Gd and Ti co-doped BiFeO₃ with significantly improved phase purity exhibited enhanced multiferroic properties. We anticipate that the presence of both exchange and magnetoelectric coupling in Bi_{0.9}Gd_{0.1}Fe_{0.9}Ti_{0.1}O₃ multiferroic material might be worthwhile for potential applications in novel multifunctional devices. We may further conclude that an appropriate choice of co-doping elements and fine composition adjustment are keys to optimize the multiferroic properties of BiFeO₃ ceramics.

5.3 Future work

In a previous investigation simultaneous substitution of Gd and Ti in place of Bi and Fe, respectively in BiFeO₃ multiferroics improved their morphological, dielectric and magnetic properties at room temperature [1]. Therefore, in this investigation, we were interested to conduct experiments on temperature dependence of magnetic properties of Gd and Ti co-doped Bi_{0.9}Gd_{0.1}Fe_{1-x}Ti_xO₃ (x = 0.00 - 0.20) multiferroic materials. Later on, the optical properties and photocatalytic activity of 10% Gd and Ti co-doped BiFeO₃ multiferroic materials will be carried out in the Nanotechnology Research Laboratory, Department of Physics, BUET..

It might be interesting and equally important to prepare 10% Gd and Ti co-doped BiFeO₃ nanoparticles [2] by using wet-chemical technique like sol-gel.

References:

- [1] Basith, M. A., Kurni, O., Alam, M. S., Sinha, B. L., Ahammad, B., “Room temperature dielectric and magnetic properties of Gd and Ti co-doped BiFeO₃ ceramics”, J. Appl. Phys., 115, 024102, 2014.
- [2] Basith, M. A., Ngo, D. T., Quader, A., Rahman, M. A., Sinha, B. L., Bashir Ahmad, Fumihiko Hirose and Mølhave, K., “Simple top-down preparation of magnetic Bi_{0.9}Gd_{0.1}Fe_{1-x}Ti_xO₃ nanoparticles by ultrasonication of multiferroic bulk material”, Nanoscale, 6, 14336, 2014.